Recovery of the Reflection Response for Marine Walkaway VSP

Mark Higgins

BSc (Hons) Astrophysics,
University of Edinburgh 1994

Thesis submitted for the degree of
Doctor of Philosophy
University of Edinburgh – 1998

ABSTRACT

The aim of walkaway VSP experiment is to image the region beneath the receiver. The information in the data is obscured by propagation effects in the region above the receiver such as free surface multiples, internal reflections and mode conversions. This thesis presents a method of extracting the reflectivity response of the region beneath the receiver from walkaway VSP data , assuming the earth to be horizontally stratified.

For marine experiments the source is an acoustic source in the water. Measurements of source signatures clearly show shot–to–shot variations. VSP processing, such as the separation of upgoing and downgoing waves, is based on the assumption of shot–to–shot repeatability. However, shot–to-shot variations are usually ignored during processing. I present a straightforward method for correcting for these variations. The source signature must be measured and the geometry of the measurement must be known. The recorded source wavelets are all shaped to a standard wavelet using filters in the frequency domain. The same filters are applied to the geophone data, thus removing the effect of the source variations. The method is demonstrated on real data.

As a plane horizontally–layered earth is laterally invariant, a walkaway VSP can be viewed as an experiment with a single source and a horizontal array of geophones at depth. The data are processed in the horizontal wavenumber–frequency domain, in which plane wave components are separated. I present a method for recovering the reflectivity of the region beneath the receiver in this domain. The full wavefield at the receiver level can be computed for a plane–horizontally layered earth as a superposition of plane wave responses. Given the compressional and shear velocities at the receivers, compressional and shear components are computed from the separated upgoing and downgoing wavefields. This yields four wavefields: upgoing and downgoing S-wavefields and upgoing and downgoing P-wavefields. The upgoing P–wavefield is related to the downgoing P- and S–wavefields by two reflectivities, R_{PP} and R_{PS}, respectively, and the upgoing S–wavefield is related to the downgoing P- and S–wavefields by R_{SP} and R_{SS}, respectively. Thus there are two equations relating four unknowns. Using a second source, which must change the partition of energy between the P– and S–wavefields, yields a second set of equations containing different wavefields but the same four reflectivities. These four equations are then combined to solve for the four reflectivities and image the region beneath the receiver. The method is demonstrated on synthetic data. The best results are obtained using a vertical–force/horizontal–force sea–bed source combination. Reasonable results can be obtained using an acoustic–source/horizontal–force combination. Such sea–bed sources are currently being tested for commercial use. No dual–source real data are yet available.

This thesis has been composed by myself and is original work unless explicitly stated in the text. This work has not been submitted for any other degree.

Mark Higgins, Edinburgh 1998

ACKNOWLEDGEMENTS

This project was funded by Elf UK (Geoscience Research Centre). The data were provided by Elf Norge and partners. I thank Elf for funding this project and granting permission to show the data. I am very grateful to Peter Rowbotham of Elf GRC for his interest in this work and encouragement and Jean–Luc Boelle of the Elf data centre in Pau for stimulating discussions each time we met in London.

I would like to thank: my supervisors, Anton Ziolkowski and Colin MacBeth, particularly for their patience with me as a student; Margaret Penman, secretary to the Centre for Reservoir Geoscience Research; David Taylor for assisting me with the synthetic seismogram modelling and Rodney Johnston, who provided some of the subroutines used for the source wavelet shaping.

Friends and colleagues in the Grant Institute and Murchison House, have shared their knowledge and experience freely. I am particularly grateful to: Richard Holme knowing much mathemagics and being patient with it; Shane and Chis for knowing lots about computers; and Fox E. Fox and the other Anton for stress relief.

During the last 8 years I have met many good friends in Edinburgh. I thank them for their friendship and support and hope they've enjoyed the more exotic culinary creations that have been placed before them, including coronation fish–finger. I am indebted to my flat mates of the final two years of this work. Helen, for many fine cakes that "didn't turn out quite right", her encouragement to keep the flat in a live-able state and being generally a wise person, and Martin who introduced me to the guitar and effective monosyllabic communication. I am indebted to Pete and Jane for their constant friendship and hospitality.

To my folks;

who have waited 21 years for their son to leave full time education.

CONTENTS

Notations, definitions and conventions ix

1 Introduction 1

1.1 Motivation for research . . . 1

1.2 Philosophy – multiple suppression or recovering reflectivity? . . . 2

1.3 Summary of the problem and solution . . . 2

1.4 Thesis organisation . . . 2

2 Theory of wave propagation 5

2.1 Introduction . . . 5

2.2 Elements of continuum mechanics and elasticity . . . 5

2.2.1 The stress tensor . . . 5

2.2.2 The strain tensor . . . 7

2.2.3 Hooke's law . . . 7

2.2.4 Newton's second law . . . 7

2.2.5 The elastodynamic system of differential equations . . . 8

2.2.6 The wave equation . . . 10

2.2.7 Wave equation – conclusion . . . 11

2.3 Decomposition of spherical waves to plane waves . . . 11

2.4 Conclusions 15

3 Multicomponent marine borehole seismology **17**

3.1 Introduction 17

3.2 A brief history of vertical seismic profiling 17

3.3 Standard VSP processing techniques: a short review 18

3.3.1 Wavelet shaping 19

3.3.2 VSP wavefield separation and deconvolution 20

3.3.3 Other considerations in VSP processing 22

3.4 Examples of multicomponent experiments 22

3.5 Walkaway VSP geometry and data 24

3.6 The Elf dataset 25

3.7 Initial processing of the data 28

3.8 Real data section 32

3.9 Conclusions 32

4 The Marine Seismic Source: theory **35**

4.1 Introduction 35

4.1.1 The physics of an expanding and contracting bubble 35

4.2 The wavefield of a single bubble: Lamb's wave equation 38

4.3 Linearisation and approximate solution of Lamb's equation 40

4.4 Solving for pressure and particle velocity in the water 41

4.5 Conclusions 43

5 Source signal measurement and deconvolution **45**

5.1 Introduction 45

5.2 Source Measurements 45
5.3 Source measurement deghosting 48
5.4 Sensitivity analysis 50
5.5 Theory and application of measured wavelet shaping 50

6 Recovering the reflectivity: theory 57

6.1 Introduction 57
6.2 The wavefield at the receiver 57
6.3 The transfer matrices, $m_{U|D}$ 60
6.4 Recovery of the reflectivity 64
6.5 Wavefield division 66
6.6 The second source 69
6.7 Reflectivity display 69
6.8 Processing summary 71
6.9 Discussion and conclusions 71

7 The (x, y, t) to (k_x, k_y, ω) transform 73

7.1 Introduction 73
7.2 Aliasing 73
7.3 Transforming from time-space to frequency–space 74
7.4 The space to wavenumber transform 77
7.5 The (ω, k_x, k_y) domain 79
7.6 The inverse transform 80
7.7 Transform summary 80
7.8 Conclusions 81

8 Recovering the reflectivity: application to synthetics **83**

8.1 Introduction 83

8.2 The (synthetic) data 83

8.3 P and S separation 88

8.4 Recovering the reflectivity 91

8.5 Upgoing wavefield reconstruction 95

8.6 Discussion and initial conclusions 96

8.7 Complex (synthetic) data example 98

8.8 Conclusions 103

9 Conclusions **105**

9.1 Conclusions 105

9.2 Suggestions for further work and speculation 106

A Sensitivity of source measurement deghosting **115**

LIST OF FIGURES

2.1 Surface Σ though a body in equilibrium 6

2.2 Spherical wave from a source at the origin 12

2.3 Definitions for spherical wave decomposition in angular coordinates 15

3.1 Reginald Fessenden's 1917 patent application, from Hardage (1983) 18

3.2 Single line walk–away VSP geometry 23

3.3 Outline of data recording scheme 25

3.4 Schematic diagram of walkaway VSP geometry 26

3.5 Radial and Vertical common receiver gathers, respectively 27

3.6 Definition of axes and angles of propagation 29

3.7 Horizontal plane rotation angles 29

3.8 Predicted horizontal plane rotation angles 30

3.9 Difference in horizontal plane rotation angles 31

3.10 Annotated walkaway VSP section (radial component) 32

4.1 Comparison of adiabatic and more realistic bubble expansion models 37

4.2 Definition of the equivalent bubble and external region. 38

4.3 Sketch of bubble at some instantaneous time, t. After Ziolkowski (1998). . . 39

5.1 Timing Line; after Dillon and Collyer (1985) 45

5.2 Geometry of source measurement. 46

5.3 Measured Source Signatures 47

5.4 Measured source signatures with trace average subtracted 47

5.5 Source signatures A) before and B) after wavelet shaping 52

5.6 A) Time domain wavelet shaping filter and B) desired wavelet 52

5.7 Vertical geophone data before wavelet shaping 53

5.8 Vertical geophone data after wavelet shaping 54

6.1 Terms in equation (6.2) 59

6.2 P-wave decomposition to dynamic frame 61

6.3 SV-wave decomposition to dynamic frame 62

6.4 Flowchart for the P-S separation and division 65

6.5 Absolute magnitude of $P(x)$ 67

6.6 Absolute magnitude of $Q(x)$ 67

6.7 Absolute magnitude of $R(x)$, as computed by division 68

6.8 Absolute magnitude of $Q(x)R(x) - P(x)$ 68

6.9 Geometry for computing wavefields from the recovered reflectivities 70

7.1 A) Original trace 1 B) Band–pass filtered trace 1 74

7.2 Cartoon showing a)A real time trace b)The real part of the DFT of a) after (Bracewell, 1986),p363 76

7.3 A) Amplitude trace 1 B) Phase trace 1 (spectra are wrapped about twice the Nyquist frequency) 76

7.4 A) Amplitude spectra in (x, y)-plane B) Phase spectra in (x, y)-plane, for a fixed frequency 78

7.5 A) Amplitude spectra in (k_x, k_y)-plane B) Phase spectra in (k_x, k_y)-plane, for a fixed frequency 79

7.6 A) Upgoing $P-$ amplitude spectra in (k_x, k_y)-plane, B) Upgoing $S-$ amplitude spectra in (k_x, k_y)-plane 80

8.1 Simple earth model 84

8.2 Acoustic source data, vertical and radial components 85

8.3 Vertical force source data,vertical and radial components 86

8.4 Horizontal force source data,vertical and radial components 87

8.5 Acoustic source data, $P-$ and $S-$ components 88

8.6 Vertical force source data, $P-$ and $S-$ components 89

8.7 Horizontal force source data, $P-$ and $S-$ components 90

8.8 Reflectivity wavefields, explosion and vertical–force dual source 91

8.9 Reflectivity wavefields, explosion and horizontal–force dual source 92

8.10 Reflectivity wavefields, vertical–force and horizontal–force dual source . . . 93

8.11 Acoustic source data reconstruction and difference 95

8.12 Vertical force source data, reconstruction and difference 96

8.13 Horizontal force source data, reconstruction and difference 97

8.14 Complex earth model 98

8.15 Vertical force source data. Complex model 99

8.16 Horizontal force source data, Complex model 100

8.17 Vertical force source, mode separated data. Complex model 101

8.18 Horizontal force source, mode separated data, Complex model 102

8.19 Recovered reflectivity. Complex model 103

Notations, Definitions and Conventions

All the terms used in this thesis are given here. For complete definitions one should refer to the main text. SI units are used throughout. Commonly used abbreviations are also given here.

Scalar and vector quantities

Vector quantities are written in bold type face, $\boldsymbol{F}$, and scalar quantities in normal type, F. All vectors are three-vectors, unless otherwise stated in the text.

Space and Time

A right–handed Cartesian reference frame with z increasing with depth is the main frame of reference in this work. For diagrams the x axis is in the plane of the paper and the y axis is perpendicular to the page. If y increases out of the page then x increases to the right and if y increases into the page x increases to the left. Let

$$\boldsymbol{x} = (x, y, z)$$

in the Cartesian frame. In general let $\boldsymbol{x} = (x_1, x_2, x_3)$ represent the position three-vector in $\mathbb{R}^3$ and $\boldsymbol{n}_i$ the ith orthonormal basis vector such that

$$\boldsymbol{x} = \sum_{i=1}^{3} x_i \boldsymbol{n}_i.$$

Let t denote time. Frames which are a pure rotation from the Cartesian frame are commonly used. The cylindrical system (r, θ, z) is defined by

$$\left(x^2 + y^2\right)^{\frac{1}{2}} = r \quad \tan^{-1}\frac{y}{x} = \theta \quad \text{and} \quad z \to z.$$

The summation convention is used for repeated subscripts, e.g.

$$a_i b_i = a_1 b_1 + a_2 b_2 + a_3 b_3.$$

Spatial differentiation with respect to x_i is represented by

$$\partial_i v_j = \frac{\partial v_j}{\partial x_i}.$$

Temporal differentiation is represented by ∂_t or an overdot $\dot{u}_i$ All tensors are Cartesian, covariant a^i and contravariant a_i forms are identical.

Special functions

$\delta(x)$	$\int_{-\infty}^{\infty} \delta(x-\eta) f(x)\ \mathrm{d}x = f(\eta)$	the Dirac delta function
$\delta(\boldsymbol{x})$	$\delta(x_1)\delta(x_2)\delta(x_3)$	the three dimensional delta function
δ_{ij}	$\delta_{ij} a_j = a_i$	the Kronecker delta function
$\mathcal{J}_0(x)$	$\sum_{s=0}^{\infty} \frac{(-1)^2}{(s!)^2} \left(\frac{x}{2}\right)^{2s}$	the zeroth order Bessel function

Integral transforms

It is assumed that all integral transforms used converge for the all cases presented in this thesis. There are known cases when they do not converge, but none of these cases apply here. A complete discussion of these transforms is found in Bracewell (1986).

The Fourier transform with respect to t and transform parameter ω is

$$\boldsymbol{F}(\boldsymbol{x}, \omega) = \int_{-\infty}^{\infty} \boldsymbol{f}(\boldsymbol{x}, t) \exp\{i\omega t\}\ \mathrm{d}t.$$

The inverse transform is

$$\boldsymbol{f}(\boldsymbol{x}, t) = \frac{1}{2\pi} \int_{-\infty}^{\infty} \boldsymbol{F}(\boldsymbol{x}, \omega) \exp\{-i\omega t\}\ \mathrm{d}t.$$

The change from small to capital letter denotes the change of domain.

The Fourier transform with respect to space x and its transform parameter k_x is

$$\tilde{\boldsymbol{F}}(k_x,\omega) = \int_{-\infty}^{\infty} \boldsymbol{F}(\boldsymbol{x},\omega) \exp\{-ik_x x\} \, \mathrm{d}x$$

and its inverse

$$\boldsymbol{F}(x,\omega) = \frac{1}{2\pi} \int_{-\infty}^{\infty} \tilde{\boldsymbol{F}}(k_x,\omega) \exp\{ik_x x\} \, \mathrm{d}k_x.$$

The $\tilde{}$ denotes the change of domain.

The three dimensional space-time to horizontal–wavenumber-angular frequency transform is

$$\hat{\boldsymbol{F}}(k_x,k_y,\omega) = \iiint_{-\infty}^{\infty} \boldsymbol{f}(x,y,t) \exp i(wt - k_x x - k_y y) \, \mathrm{d}x \, \mathrm{d}y \, \mathrm{d}t$$

and has inverse:

$$\boldsymbol{f}(x,y,t) = \frac{1}{8\pi^3} \iiint_{-\infty}^{\infty} \hat{\boldsymbol{F}}(k_x,k_y,\omega) \exp i(k_x x + k_y y - wt) \, \mathrm{d}k_x \, \mathrm{d}k_y \, \mathrm{d}\omega.$$

The Fourier transform of the nth derivative of a function, $\boldsymbol{F}_n(\omega)$ is related to the transform of the function $\boldsymbol{F}(\omega)$ by:

$$\boldsymbol{F}_n(\omega) = (-i\omega)^n \boldsymbol{F}(\omega).$$

A function in time $f(t)$ can be retarded $f(t) \to f(t-\tau)$ using the convolutional relationship:

$$f(t-\tau) = f(t) * \delta(t-\tau),$$

where $*$ represents convolution.

The zeroth Hankel transform is defined in terms of the two dimensional Fourier transform by

$$\iint_{-\infty}^{\infty} f(x,y) \exp\{-i2\pi(k_x x + k_y y)\} \, \mathrm{d}x \, \mathrm{d}y = 2\pi \int_0^{\infty} f'(r) J_0(2\pi k_r r) r \, \mathrm{d}r,$$

where $f'(r) = f\left((x^2+y^2)^{\frac{1}{2}}\right)$ and k_r is the radial wavenumber.

SI base units

Quantity	Unit	
	Name	Symbol
length	metre	m
mass	kilogramme	kg
time	second	s
thermodynamic temperature	Kelvin	K

SI derived units

Quantity	Unit		
	Name	Symbol	Equivalent
frequency	Hertz	Hz	s^{-1}
force	Newton	N	kg ms^{-2}
pressure	Pascal	Pa	Nm^{-2}
energy	Joule	J	kg m^2s^{-2}
power	Watt	W	Js^{-1}
electric potential	volt	V	W A^{-1}

Symbols

Symbol	Description	Units
A^*	complex conjugate of A	same as A
b_{ij}	initial stress tensor	Pa
c_{ijkl}	stiffness tensor	Pa
c	acoustic velocity of water	m s^{-1}
C	Hydrophone calibration constant	V Pa^{-1}
$\boldsymbol{D}$	Matrix of downgoing wavefields	m s^{-1}
e_{ij}	strain tensor	%
$\boldsymbol{f}$	source force	Nm^{-3}
$G_{x,y,z}$	geophone gains for x, y, z component	
h_{ij}	volume source density of strain rate tensor	%/s
h	enthalpy	J kg^{-1}
$\boldsymbol{I}$	3x3 identity matrix	
$\Im$	the imaginary axis	–
k	wavenumber magnitude	m^{-1}
$\boldsymbol{k}$	wavenumber vector	m^{-1}

Symbol	Description	Units
k_r	radial wavenumber	m^{-1}
$k_{x,y,z}$	horizontal wavenumber in the x, y or z directions	m^{-1}
m	mass	kg
$m^R_{U,D}$	transfer matrix	
$m(t)$	source measurement	Pa
$m_{real}(t)$	recorded source measurement	V
$\boldsymbol{n}_{x,y,z}$	Cartesian frame basis vectors	
$\boldsymbol{n}_{R,T,V}$	dynamic frame basis vectors	
$\boldsymbol{n}_{S1,S2,P}$	eigenvector frame basis vectors	
p	horizontal slowness	$s\ m^{-1}$
p	pressure	Pa
P_H	instantaneous seismic power in the horizontal plane	W
$P_{U\|D}$	complex amplitude of upgoing or downgoing P–wave	m/s
q_α	isotropic P-wave vertical slowness	$s\ m^{-1}$
q_β	isotropic S-wave vertical slowness	$s\ m^{-1}$
r	distance from the hydrophone to the source	m
r	distance from origin in $\mathbb{R}^2$	m
R_c	free–surface reflection coefficient	
R	distance from the hydrophone to the virtual image of a source	m
R	distance from origin in $\mathbb{R}^3$	m
$\boldsymbol{R}$	3x3 reflection matrix	
R_{PP}	P to P reflectivity	
R_{PS}	S to P reflectivity	
R_{SP}	P to S reflectivity	
R_{SS}	S to S reflectivity	
$\boldsymbol{R}$	bubble wall displacement	m
$\dot{\boldsymbol{R}}$	bubble wall velocity	$m\ s^{-1}$
$\Re$	the real axis	–
$s(t)$	source time function	Pa m
$S_{U\|D}$	complex amplitude of upgoing or downgoing S–wave	
$S(\omega)$	Transformed $s(t)$	Pa
$\boldsymbol{T}$	3x3 transmission matrix	
T	$s(t)$ to $m(t)$ transfer function in frequency domain	
$\boldsymbol{U}$	Matrix of upgoing wavefields	$m\ s^{-1}$
$\boldsymbol{u}(\boldsymbol{x})$	a particle displacement field	m

Symbol	Description	Units
$\boldsymbol{v}(\boldsymbol{x})$	a particle velocity field	m s^{-1}
V	volume	m^3
V_B	bubble volume	m^3
V_p	isotropic P-wave velocity	m s^{-1}
V_s	isotropic S-wave velocity	m s^{-1}
$\boldsymbol{x}_r$	receiver position	m
$\boldsymbol{x}_s$	source position	m
α	complex frequency shift	s^{-1}
α	isotropic P-wave velocity	m s^{-1}
β	isotropic S-wave velocity	m s^{-1}
ε	small constant for deconvolution stabilisation	varies
θ	horizontal angle of wave–normal to the x axis	radians
ϑ	measured angle of P–wave to the horizontal	radians
ϑ_p	predicted angle of P–wave to the horizontal	radians
λ	wavelength	m
λ	Lamé parameter	Pa
μ	Lamé parameter	Pa
$\boldsymbol{\Lambda}$	rotation matrix, $x, y, z \rightarrow R, T, V$	
ρ	density	kg m^{-3}
$\boldsymbol{\Sigma}$	source vector	m s^{-1}
τ_{ij}	stress tensor	Pa
ϕ	vertical angle of a wave normal to the x axis	radians
$\phi(x,t)$	particle velocity potential	m^2/s
$\psi(\boldsymbol{x})$	acoustic potential	m^2 s^{-1}
ω	angular frequency	s^{-1}
$\aleph_0$	a contour of integration in the complex plane	
$\beth$	source and near surface wavefield	m s^{-1}

A blank in the units column denote the quantity is dimensionless, a dash that the object has no units. Any conflicts are made clear in the text. The full wavefield notation is detailed in Chapter 6

Notations and abbreviations

V	the vertical component of a three–component geophone
H1	horizontal geophone component orthogonal to H2
H2	horizontal geophone component orthogonal to H1
R	horizontal geophone aligned in the radial direction
T	horizontal geophone aligned in the transverse direction
P	a compressional wave
SV	a vertically–polarised shear wave
SH	a horizontally–polarised shear wave
qP	a quasi–compressional wave
$qS1$	the fast quasi–shear wave
$qS2$	the slow quasi–shear wave
TIV	transverse isotropy with a vertical axis of symmetry
TIH	transverse isotropy with a horizontal axis of symmetry
DFT	the discrete Fourier transform
FFT	the fast Fourier transform

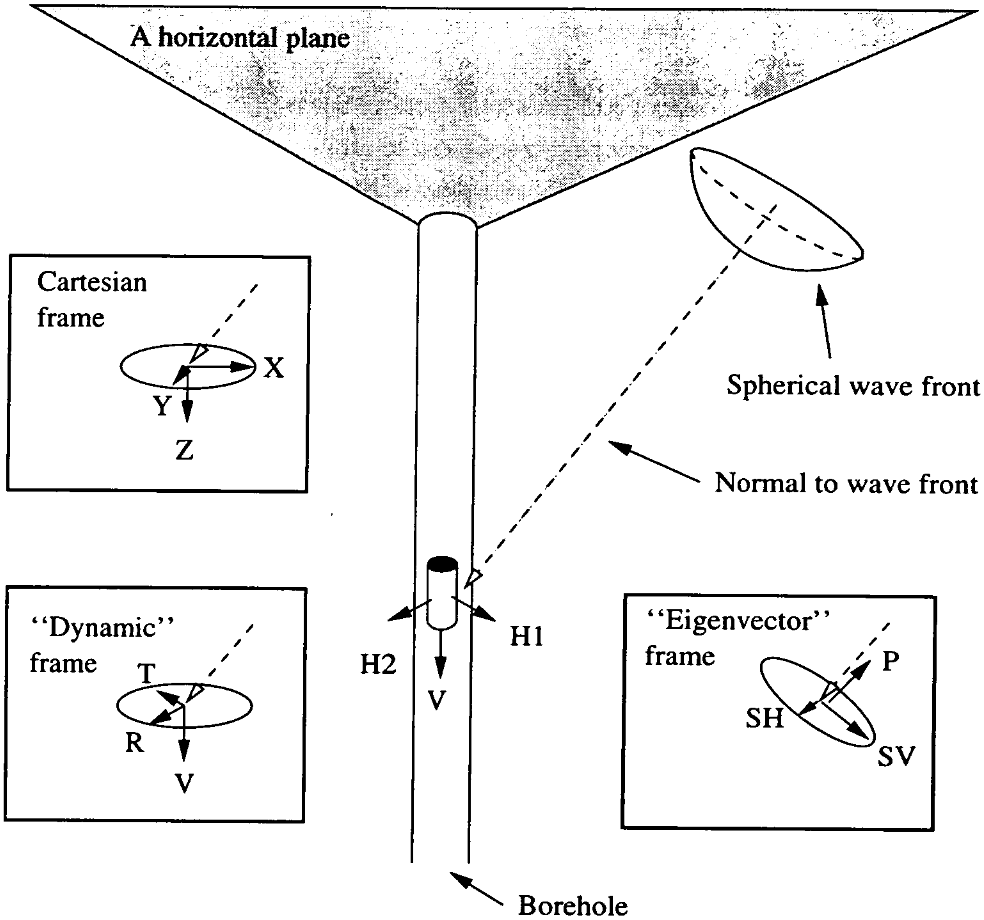

Definition of axes and reference frames

The figure shows the definition of the Cartesian axis. The directions H1,H2 and V for a geophone and R,T and P,SV and SH for a down going wave are also shown. The radial direction is defined as the direction perpendicular to the z-axis in the vertical source receiver plane. The transverse direction is orthogonal to the radial direction. These directions define the dynamic frame. The eigenvector frame the frame in which the basis vectors are aligned with the eigenvectors of the solution to the elastic wave equation. The eigenvectors are wavenumber dependent. The definition of the eigenvector frame is different for waves in non-azimuthally isotropic material where the phase and group velocities of a wave are not parallel.

INTRODUCTION

Chapter 1

1.1 Motivation for research

Borehole seismology has come a long way from check shot surveying (Dix, 1936), where the main aim of the experiment was to provide calibrated time–to–depth curves for surface seismic data or to calibrate sonic logs. This ignores all the data but first break times. Today the compressional wavefield is recorded almost in full and it is becoming common to record more of the shear wavefield. With this increase in the quantity and quality of borehole data there has come a demand for new processing techniques to obtain more from the data.

Multiples are often the most serious problems in seismic reflection surveying (Wiggins, 1988). As with marine surface seismic data, free–surface multiples are a problem for marine walkaway vertical seismic profiles (VSPs) (MacBeth and Liu, 1994b). This project began as an attempt to develop a wave–equation based free–surface multiple suppression scheme for marine walkaway VSP. The aim of suppressing the multiples is to allow better imaging of the experiment target.

MacBeth and Liu (1994b) consider the problem of free–surface multiples when looking at the direct (non–reflected) wavefield in VSPs, particularly when considering the converted wavefield or the relative amplitude of the $P-$ and $S-$ arrivals. The reflected part of the VSP wavefield has similar problems, the multiples make computation of relative amplitude of the $P-$ and $S-$ arrivals difficult. Amplitude versus offset methods have become popular recently, and ideally should be applied to multiple–free data. For the VSP case there is also the problem of effects due to the region above the receiver, called the near–surface. For a walkaway VSP with the receiver at 3km depth there is much scope for near–surface effects to cause severe problems when trying to image the target.

Some authors refer to the multiples associated with the water column as free–surface multiples, highlighting the fact that without the free–surface these multiples could not exist and that it is the magnitude of the free–surface reflection coefficient that causes the problem to be so serious. Other authors refer to them as water bottom multiples as the sea–bed is the first reflection in the multiple.

There are many surface–seismic multiple–suppression schemes in the literature. Wiggins (1988) presents a wave–equation–based prediction and subtraction scheme which requires a model of the sea–bed reflectivity to begin with. Vershuur *et al.* (1992) present an adaptive wave–equation based scheme in which the wavefield is extrapolated one round–trip through the water, each event then becomes a multiple of one higher order. The predicted multiples are then subtracted from the original data. Kennett (1979) presents a method of approximately inverting for the P–P reflectivity of the earth beneath the water layer. It is this scheme to which the work here is most closely related.

1.2 Philosophy – multiple suppression or recovering reflectivity?

This thesis does not solve a multiple attenuation or suppression problem. Rather the aim becomes to recover information about a specific region of the earth, where that information is not contaminated by information about any other region in the earth. In this case the region of interest is the region beneath the receiver. The effects of the near–surface and the free–surface are eliminated from the data by recovering the reflectivity of the earth for the region beneath the receiver.

1.3 Summary of the problem and solution

The equations for seismic wave propagation in stratified media are well know both for the isotropic (Kennett, 1981, 1983) and the anisotropic (Fryer and Frazer, 1984) case. These equations are used to compute the full wavefield at the receiver level. I then manipulate this wavefield so that the reflectivity of the region beneath the receiver can be computed as a combination of upgoing and downgoing wavefields for two different sources.

The scheme presented is dependent on the separation of upgoing and downgoing wavefields as well as transforming the data to the frequency–(horizontal)-wavenumber domain. Both of these processing steps require that the source does not vary shot–to–shot. The marine seismic source does vary shot–to–shot so I present a method of processing the data to remove the effect of such source variations. VSP wavefield separation schemes are discussed in Chapter 3.

1.4 Thesis organisation

- **1 Introduction.** This chapter. All the terms used in this thesis as well as definitions of some of the important expressions are given before this chapter.

- **2 Elastic wave theory.** The basic elements of wave propagation are revised and two key results are highlighted: the solutions of the wave equation using potentials and the decomposition of spherical waves into plane wave components.

- **3 Multicomponent seismology.** Here the data are introduced and the basic initial processing is discussed. The initial rotation of the multicomponent data and separation of upgoing and downgoing wavefields is given particular attention.

- **4 Acoustic source measurement: theory.** Shot–to–shot variations must be removed from the data to prevent the introduction of errors into the data. This chapter deals with source signal deghosting, deconvolution and wavelet shaping.

- **5 Acoustic source measurement: application.** Here the problem of shot–to–shot variations for a 'marine VSP is discussed and the techniques presented in chapter 4 are applied to a real data set.

- **6 Reflectivity recovery: theory.** From the equation that describes the full wavefield at the receiver for a plane–layered earth the equations of reflectivity recovery are developed, which includes P-S separation. These equations show that a wave–equation based walkaway VSP demultiple scheme requires the full reflection response of the earth and that two sources are required to recover the reflectivity of the region beneath the receiver.

- **7 Wavenumber–frequency transform.** The separation equations are formulated and the data are processed in the wavenumber–frequency domain. This chapter deals with the transform including preconditioning of the data and symmetries that are observed in the transform domain.

- **8 Reflectivity recovery: application.** Using the transform developed in chapter 7 the scheme of chapter 6 is applied to simple and more complex synthetic data examples.

- **9 Discussions and conclusions.** The synthetic examples show that the reflectivity of the region beneath the receiver is best recovered using horizontal–force/vertical–force dual-source data. Discussion on using this scheme on data from a three–dimensional earth and including anisotropy is presented.

Chapter 2

2.1 Introduction

This chapter reviews the basic elements of the theory of wave propagation and wavefield representation that are required in this thesis. The fundamental results required are the spherical wave solutions to the wave equation and the representation of a spherical wave by a set of plane waves. The physics of the source are dealt with in the following chapter.

2.2 Elements of continuum mechanics and elasticity

Starting from the definition of stress, Newton's second law of motion, and Hooke's law, the linear elastic wave equation is derived. This wave equation is solved with suitable boundary conditions for the problems met in this thesis.

The description of an elastic solid is best described using Cartesian tensors. This means that the equations developed are invariant under frame rotation. The wave equation is the same in the dynamic frame and the eigenvector frame for example (These frames are defined in notations section of Chapter 1). The different solutions to the wave equation are more easily expressed in some frames than in others.

2.2.1 The stress tensor

Consider a homogeneous perfectly elastic body. Figure (2.1) shows such a body undergoing deformation, with surface Σ and its normal vector $\boldsymbol{n}$. The traction at a point fully describes the net force acting on that point. The body is deformed by applying external forces but is in dynamic equilibrium. The internal forces in the body act to resist deformation. The internal forces in the body are analysed by looking at a surface Σ, which is a cross section though the body and contains the point O. The surface is described by a unit vector $\boldsymbol{n}$, which is normal to the surface and originates at O. The traction $\boldsymbol{t}$ is the force per unit area across Σ. Physically, the traction is the contact force, between particles on either side of the surface, per unit area. There is an infinite number of planes and thus an infinite number of tractions containing O

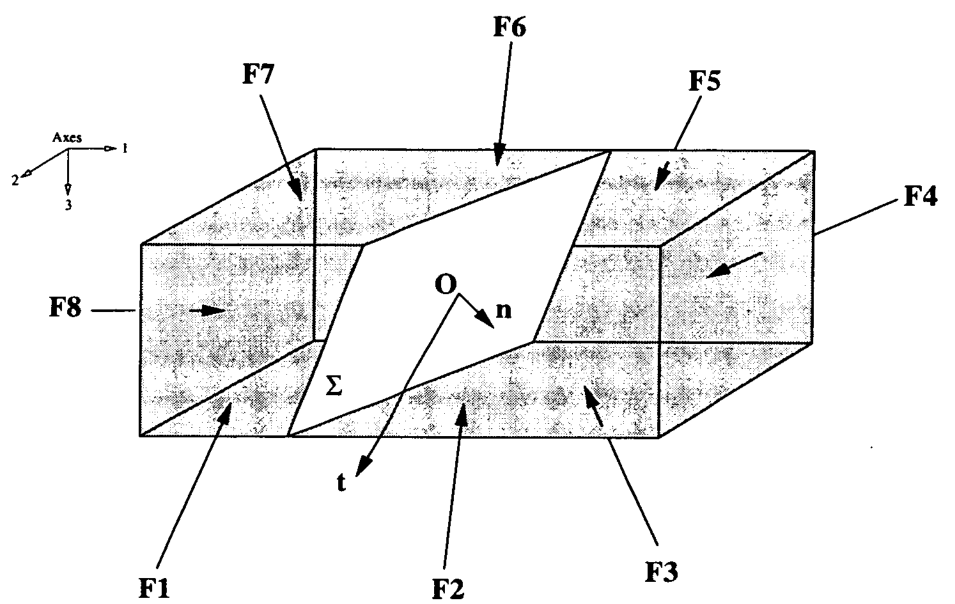

Figure 2.1: Surface Σ though a body in equilibrium

all defined by different unit normal vectors. The stress at O is the sum of all the possible tractions acting though O.

A normal vector decomposed into orthonormal components is

$$n = (n_1, n_2, n_3). \tag{2.1}$$

The component of the traction vector in the 1–direction is

$$t_1 = \tau_{11}n_1 + \tau_{12}n_2 + \tau_{13}n_3, \tag{2.2}$$

$\tau_{11}n_1$ is the component of t_1 acting in the same direction as n_1. The units of $\tau_{11}n_1$ are force per unit area. Generalising to the three orthogonal tractions yields

$$t_i = \tau_{ij}n_j. \tag{2.3}$$

This is Cauchy's stress formula. Physically τ_{ij} is the i–th component of traction acting across a plane normal to the j–axis. The 3x3 stress–tensor τ_{ij} is required to define the tractions, its familiar form is

$$\tau_{ij} = \begin{bmatrix} \tau_{11} & \tau_{12} & \tau_{13} \\ \tau_{21} & \tau_{22} & \tau_{23} \\ \tau_{31} & \tau_{32} & \tau_{33} \end{bmatrix}. \tag{2.4}$$

The diagonal terms are the normal components of stress and the off–diagonal terms are the shearing components of stress.

2.2.2 The strain tensor

The infinitesimal strain tensor e is defined as (Aki and Richards, 1980, page 13)

$$\frac{1}{2}(\partial_j u_i + \partial_i u_j) = e_{ij}. \tag{2.5}$$

This definition is valid for small (normally less than one percent) strains. The strains associated with seismic body wave propagation are smaller than this. Assuming properties of the stiffness tensor such that $\partial_j u_i = \partial_i u_j$, the strain tensor can be defined as

$$e_{ij} = \partial_j u_i. \tag{2.6}$$

2.2.3 Hooke's law

The generalised form of Hooke's Law is

$$\tau_{ij} = c_{ijkl} e_{kl} + b_{ij}, \tag{2.7}$$

where c_{ijkl} is the stiffness tensor. The quantity b_{ij} is the initial stress tensor. Under consideration here are elastodynamic problems where the initial strain rate corresponds to an initially stress–free state. Thus body forces such as gravity or tectonic stresses can be neglected for these problems. This is a linear elastic relationship. Time dependent and nonlinear regimes are not considered here.

2.2.4 Newton's second law

Newton's second law can be stated thus

$$\boldsymbol{f}_N = \frac{\mathrm{d}(m\boldsymbol{v})}{\mathrm{d}t}, \tag{2.8}$$

where $\boldsymbol{f}_N$ is the force, m the (constant) mass and $\boldsymbol{v}$ the particle velocity. That is, the force acting on a particle is equal to the change in the linear momentum of that particle. For a continuum of particles the total force acting on a material volume is equal to rate of change of the total linear momentum of the material within the volume. For a volume V bounded by a closed surface Σ this is

$$\frac{\mathrm{d}}{dt}\int_V \rho \boldsymbol{v}\,\mathrm{d}V = \int_\Sigma \boldsymbol{t}\,\mathrm{d}\Sigma + \int_V \boldsymbol{f}\,\mathrm{d}V. \tag{2.9}$$

The second term on the right–hand side is the total (body) force exerted on the volume. Here the elastodynamic wavefield is being calculated, and volume sources such as gravitational and magnetic forces are negligible, $\boldsymbol{f}$ is volume source density of force.

2.2.5 The elastodynamic system of differential equations

Expressing the first term on the right hand side in indicial notation and applying the Cauchy stress relation, (2.9) is written

$$\frac{\mathrm{d}}{\mathrm{d}t}\int_V \rho \boldsymbol{v}\,\mathrm{d}V = \int_\Sigma n_m \tau_{mk}\,\mathrm{d}\Sigma + \int_V \boldsymbol{f}\,\mathrm{d}V. \tag{2.10}$$

Assuming conservation of mass and therefore total particle number, the left hand side can be expressed as

$$\int_V \rho \frac{\mathrm{d}\boldsymbol{v}}{\mathrm{d}t}\,\mathrm{d}V = \int_\Sigma n_m \tau_{mk}\,\mathrm{d}\Sigma + \int_V \boldsymbol{f}\,\mathrm{d}V. \tag{2.11}$$

Consider an infinitesimal change in velocity $\boldsymbol{v}$, thus:

$$\Delta \boldsymbol{v} = \frac{\partial \boldsymbol{v}}{\partial x}\cdot \Delta x + \frac{\partial \boldsymbol{v}}{\partial y}\cdot \Delta y + \frac{\partial \boldsymbol{v}}{\partial z}\cdot \Delta z + \frac{\partial \boldsymbol{v}}{\partial t}\cdot \Delta t, \tag{2.12}$$

where $\boldsymbol{u}$ is the particle displacement.

The total derivative of this is

$$\frac{D\boldsymbol{v}}{Dt} = \lim_{\Delta t\to 0} \frac{\frac{\partial \boldsymbol{v}}{\partial x}\cdot \Delta x + \frac{\partial \boldsymbol{v}}{\partial y}\cdot \Delta y + \frac{\partial \boldsymbol{v}}{\partial z}\cdot \Delta z + \frac{\partial \boldsymbol{v}}{\partial t}\cdot \Delta t}{\Delta t} = \frac{\partial \boldsymbol{v}}{\partial t} + \nabla \boldsymbol{v}\cdot \dot{\boldsymbol{u}}, \tag{2.13}$$

where $\dot{\boldsymbol{u}} = \frac{\partial \boldsymbol{u}}{\partial t}$ The second term is called the convective derivative. This term, $\nabla \boldsymbol{v}\cdot \dot{\boldsymbol{u}}$, is zero if the motion is considered in the frame of a particular particle. This is known as the Lagrangian frame, the Eulerian frame is the frame fixed in space. This distinction is used later in this thesis.

The familiar form of Gauss's theorem is

$$\int_s \boldsymbol{V}\cdot \mathrm{d}s = \int_V \nabla\cdot \boldsymbol{V}\,\mathrm{d}V. \tag{2.14}$$

That is, the surface integral of a vector over a closed surface equals the volume integral of the divergence of that vector over the volume enclosed by the surface, assuming the vector is continuously differentiable within the volume. Therefore the surface integral in (2.11) is written

$$\int_V \rho \frac{\mathrm{d}\boldsymbol{v}}{\mathrm{d}t}\,\mathrm{d}V = \int_V \nabla_m \tau_{mk}\,\mathrm{d}V + \int_V \boldsymbol{f}\,\mathrm{d}V, \tag{2.15}$$

or

$$\int_V \rho \frac{\mathrm{d}\boldsymbol{v}}{\mathrm{d}t}\,\mathrm{d}V = \int_V \partial_m \tau_{mk}\,\mathrm{d}V + \int_V \boldsymbol{f}\,\mathrm{d}V. \tag{2.16}$$

by equation (2.14)[1] this can be expressed as

$$\int_V \left(\rho \frac{\mathrm{d}\boldsymbol{v}}{\mathrm{d}t} - \partial_m \tau_{mk} - \boldsymbol{f}\right)\,\mathrm{d}V = 0. \tag{2.18}$$

If the entire integrand is zero this is

$$\rho \frac{\mathrm{d}\boldsymbol{v}}{\mathrm{d}t} - \partial_m \tau_{mk} - \boldsymbol{f} = 0, \tag{2.19}$$

which is known as the local form of the stress equation of motion.

Stress and displacement are related by

$$\tau_{ij} = c_{ijkl}\partial_l u_k + q_{ij}, \tag{2.20}$$

where q_{ij} is the volume source density of strain. Taking the time derivative the uniform strain rate is,

$$\partial_t \tau_{ij} = c_{ijkl}\left[\partial_l v_k - h_{ij}\right]. \tag{2.21}$$

The *volume source density of strain rate* is denoted h_{ij}, which is the time derivative of q_{ij}.

This equation is the linearised equation of deformation rate.

[1]Here the general tensor rather than vector field version (equation 2.14) of Gauss's theorem is used. Schutz (1980) shows that

$$\int_s \xi_i n_i\,\mathrm{d}s = \int_V \partial_i \xi_i\,\mathrm{d}V \tag{2.17}$$

for an i-dimensional tensor field ξ_i in a Cartesian space and the surface s and volume V have dimensionalities related to ξ.

2.2.6 The wave equation

Spatial differentiation of the deformation rate equation (2.21) yields

$$\partial_i \partial_t \tau_{ij} = c_{ijkl} \partial_i \left[\partial_l v_k - h_{ij} \right]. \tag{2.22}$$

Temporal differentiation of the stress equation of motion 2.19 yields

$$\partial_t \left(\rho \frac{\mathrm{d}\boldsymbol{v}}{\mathrm{d}t} \right) - \partial_t \partial_m \tau_{mk} - \partial_t \boldsymbol{f} = 0. \tag{2.23}$$

Combining these two equations (2.22,2.23) and eliminating stress yields

$$\partial_t \left(\rho \frac{\mathrm{d}\boldsymbol{v}}{\mathrm{d}t} \right) + c_{ijkl} \partial_i \left[\partial_l v_k - h_{ij} \right] - \partial_t \boldsymbol{f} = 0, \tag{2.24}$$

which is the elastic wave equation. For marine acoustic sources $\boldsymbol{f}$ is zero (no shear force), thus

$$\partial_t \left(\rho \frac{\mathrm{d}\boldsymbol{v}}{\mathrm{d}t} \right) + c_{ijkl} \partial_i \left[\partial_l v_k - h_{ij} \right] = 0. \tag{2.25}$$

The acoustic source is h_{ij}. The physics of sea-bed sources is not discussed in this thesis.

For isotropic material the elastic constants tensor can be represented in terms of the Lamé parameters λ and μ by (Menke and Abbott, 1990, p248)

$$c_{ijkl} = \lambda \delta_{ij} \delta_{kl} + \mu (\delta_{ik} \delta_{jl} + \delta_{il} \delta_{jk}). \tag{2.26}$$

Helmholtz's theorem states that a vector field which vanishes at infinity can be represented by a rotational field and a solenoidal field. Thus the particle velocity can be represented by (Aki and Richards, 1980, p69)

$$\boldsymbol{v} = \nabla \psi + \nabla \times \boldsymbol{\phi}, \tag{2.27}$$

where $\boldsymbol{\phi}$ and ψ are vector and scalar particle displacement potentials, respectively. In this case the (source free) wave equation can be separated into two parts

$$\nabla^2 \psi = \frac{1}{\alpha^2} \frac{\partial^2 \psi}{\partial t^2}, \tag{2.28a}$$

and

$$\nabla^2 \boldsymbol{\phi} = \frac{1}{\beta^2} \frac{\partial^2 \boldsymbol{\phi}}{\partial t^2}, \tag{2.28b}$$

where

$$\alpha = \sqrt{\frac{\lambda + 2\mu}{\rho}}, \tag{2.29a}$$

and

$$\beta = \sqrt{\frac{\mu}{\rho}}. \tag{2.29b}$$

2.2.7 Wave equation – conclusion

The full wave equation has been derived and solved in terms of Helmholtz potentials for isotropic media. The wave equation can be solved for arbitrary anisotropic media, in which case the Helmholtz potentials cannot be constructed. The solution has eigenmodes corresponding to the P–like and two S–like modes for both upgoing and downgoing waves. The compressional and shear wave fields are not decoupled for many anisotropic media, however the eigenmodes are orthogonal. As each mode in the upgoing or downgoing wavefield is orthogonal to all other modes it is possible to separate wave types based on particle motion. For the isotropic case the scalar wave (the P wave) propagates in the source–receiver direction, the waves corresponding to the vector potential propagate orthogonal to this and correspond to SV and SH modes.

2.3 Decomposition of spherical waves to plane waves

The physics of plane wave propagation is well understood and relatively simple. A full understanding of the propagation of spherical waves has only been possible since the early twentieth century. Spherical waves can be decomposed into cylindrical waves, via the Sommerfeld integral (Sommerfeld, 1909), and into plane waves via the Weyl integral (Weyl, 1919). This derivation follows Brekhovskikh (1960), chapter 4. The derivation of Båth (1968), chapter 7, is similar but he uses the opposite sign convention for propagating waves; he also calls the Weyl integral the Sommerfeld integral. [2]

Consider a sinusoidal source of spherical waves represented by the scalar potential $\psi(R)$. The acoustic potential at some far-field distance $R = (x^2 + y^2 + z^2)^{\frac{1}{2}}$ from the source is

[2] Derivations are also given in: Aki and Richards (1980), chapter 6, Ewing *et al.* (1957), chapter 1 and Menke and Abbott (1990), chapter 8.

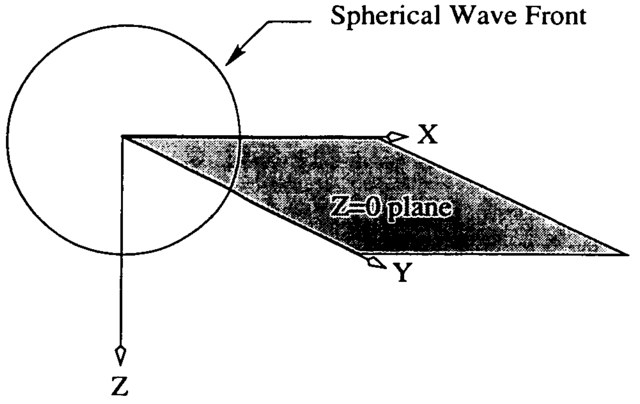

Figure 2.2: Spherical wave from a source at the origin

(Brekhovskikh, 1960, p237)

$$\psi_s = \frac{V_0}{4\pi}\frac{e^{i(kR-\omega t)}}{R}, \tag{2.30}$$

where $V_0/4\pi$ is a measure of the source strength and k is a spatial analogue to ω. Such a source could be a bubble oscillating sinusoidally where the bubble radius is small compared to the wavelength of the emitted acoustic waves. Figure 2.2 shows a spherical wave front from such a source positioned at the origin. Ignoring any terms in time t, which are constant under spatial integration, the source is represented by:

$$\psi_s = \frac{e^{ikR}}{R}. \tag{2.31}$$

In the plane $z = 0$ the horizontal distance is $r = (x^2 + y^2)^{\frac{1}{2}}$. The acoustic potential is now,

$$\psi_s' = \frac{e^{ikr}}{r}. \tag{2.32}$$

Expressing this wavefield in terms of the inverse two dimensional Fourier transform in space yields

$$\frac{e^{ikr}}{r} = \iint_{-\infty}^{\infty} A(k_x, k_y)\exp[i(k_x x + k_y y)]\,\mathrm{d}k_x\,\mathrm{d}k_y. \tag{2.33}$$

in which $A(k_x, k_y)$ is given by

$$(4\pi^2)A(k_x, k_y) = \iint_{-\infty}^{\infty} \frac{e^{ikr}}{r}\exp[-i(k_x x + k_y y)]\,\mathrm{d}x\,\mathrm{d}y. \tag{2.34}$$

Which is the forward two-dimensional transform.

Transforming from Cartesian to polar coordinates by

$$\begin{aligned} k_x &= k_r \cos\psi, & k_y &= k_r \sin\psi, & k_r &= (k_x^2 + k_y^2)^{1/2}, \\ x &= r\cos\theta, & y &= r\sin\theta, & \mathrm{d}x\,\mathrm{d}y &= r\,\mathrm{d}r\,\mathrm{d}\theta, \end{aligned} \tag{2.35}$$

yields

$$(4\pi)^2 A(k_x, k_y) = \int_0^{2\pi} \mathrm{d}\theta \int_0^{\infty} \exp\{ir[k - \cos(\psi)\cdot k_r\cos(\theta) - \sin(\psi)\cdot k_r \sin(\theta)]\}\,\mathrm{d}r, \tag{2.36}$$

which is

$$(4\pi)^2 A(k_x, k_y) = \int_0^{2\pi} \mathrm{d}\theta \int_0^{\infty} \exp\{ir[k - k_r\cos(\psi - \theta)]\}\,\mathrm{d}r. \tag{2.37}$$

If the medium of propagation is attenuating (even if only very slightly) k has a positive imaginary component and the integral over r then is elementary. The upper limit in the evaluation of the integration then vanishes[3]. That is:

$$\int_0^{\infty} \exp\{irB\}\,\mathrm{d}r = \left.\frac{\exp\{irB\}}{iB}\right|_{r=0}^{\infty} = 0 - \frac{1}{iB} = \frac{i}{B}, \tag{2.38}$$

where $B = [k - k_r\cos(\psi - \theta)]$. Thus (2.37) is

$$(4\pi)^2 A(k_x, k_y) = i\int_0^{2\pi} \frac{\mathrm{d}\theta}{k - k_r\cos(\psi - \theta)}. \tag{2.39}$$

Making the substitution $\delta = \theta - \psi$ so $\mathrm{d}\delta = \mathrm{d}\theta$, recognising the 2π periodicity of the kernal, yields

$$(4\pi)^2 A(k_x, k_y) = i\int_0^{2\pi} \frac{\mathrm{d}\delta}{k - k_r\cos(\delta)} = \frac{i}{k}\int_0^{2\pi} \frac{\mathrm{d}\delta}{1 - (k_r/k)\cos(\delta)}. \tag{2.40}$$

The integral identity for integrals of this form is (Båth, 1968, p189)

$$\int_0^{2\pi} \frac{dx}{1 + a\cos(x)} = \frac{2\pi}{\sqrt{1 - a^2}}, \tag{2.41}$$

[3]The upper limit vanishes as $e^{i(i\infty)} = e^{-\infty} = 0$.

for $a^2 < 1$. Applying (2.41) to (2.40) yields

$$(4\pi^2)A(k_x, k_y) = \frac{i}{k}\frac{2\pi}{\sqrt{1-(-\frac{k_r}{k})^2}}. \tag{2.42}$$

Which, when simplified, is,

$$A(k_x, k_y) = \frac{i}{2\pi\sqrt{k^2-k_r^2}} = \frac{i}{2\pi\sqrt{k^2-k_x^2-k_y^2}}. \tag{2.43}$$

Substituting (2.43) into (2.33) yields

$$\frac{e^{ikr}}{r} = \frac{i}{2\pi}\iint_{-\infty}^{\infty} \frac{\exp[i(k_x x + k_y y)]\,\mathrm{d}k_x\,\mathrm{d}k_y}{\sqrt{k^2-k_x^2-k_y^2}}. \tag{2.44}$$

This is the decomposition into plane waves in the horizontal plane. The vertical wavenumber k_z is defined as

$$k_z = \sqrt{k^2-k_x^2-k_y^2}. \tag{2.45}$$

Adding the term $\pm ik_z z$ to the exponent in the integral extends equation (2.44) to waves propagating down from and up out of the (x, y)–plane respectively. Thus the full spherical wave to plane wave decomposition is

$$\frac{\mathrm{e}^{ikR}}{R} = \frac{i}{2\pi}\iint_{-\infty}^{\infty} \exp[i(k_x x + k_y y + k_z z)]\frac{\mathrm{d}k_x\,\mathrm{d}k_y}{k_z}, \qquad z \geqslant 0, \tag{2.46a}$$

and

$$\frac{\mathrm{e}^{ikR}}{R} = \frac{i}{2\pi}\iint_{-\infty}^{\infty} \exp[i(k_x x + k_y y - k_z z)]\frac{\mathrm{d}k_x\,\mathrm{d}k_y}{k_z}, \qquad z \leqslant 0. \tag{2.46b}$$

The right–hand sides of these expressions, (2.46), satisfy the wave equation and give the correct result at the origin so the extension out of the (x, y)–plane is valid. Equations (2.46) are the Weyl integral.

These expressions represent the decomposition of spherical waves into plane waves in terms of the orthogonal wavenumbers k_x, k_y and k_z in the Cartesian frame. They can be re-expressed in spherical coordinates, looking at the direction of propagation of the plane wave component in terms of the angles ϕ and θ.

The transform from Cartesian to spherical coordinates is

$$k_x = k \sin\phi \cos\theta, \qquad k_y = k \sin\theta \sin\phi, \qquad k_z = k \cos\phi. \tag{2.47}$$

The definitions of these angles is shown in figure 2.3. The third of these transforms has consequences on the limits of integration in ϕ. If the horizontal wavenumbers are zero then k is equal k_z and the ϕ will be zero, that is, the wave is propagating vertically. As the magnitude of the horizontal wavenumbers becomes large the vertical wavenumber becomes imaginary, a consequence of (2.45). If k_z is complex then ϕ must also become complex. Therefore, limits of integration are $\phi = 0 \ldots \pi/2 - i\infty$ in the vertical plane and $\theta = 0 \ldots 2\pi$ in the horizontal plane. Figure 2.3 shows the path of integration $\aleph_0$ about ϕ in the complex plane.

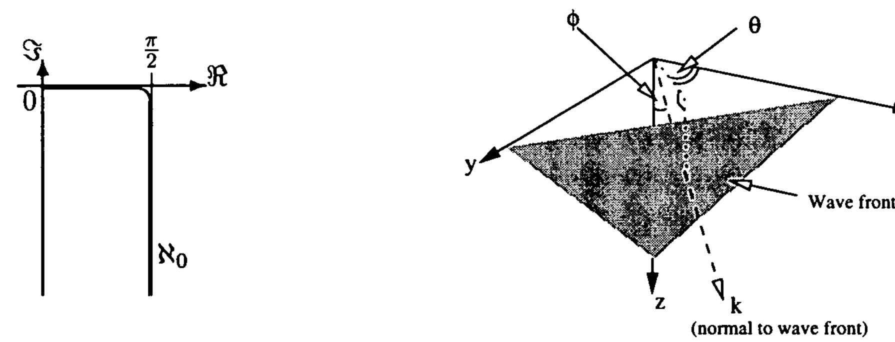

Contour of integration in the complex plane

Angle definitions for a single plane wave component

Figure 2.3: Definitions for spherical wave decomposition in angular coordinates

From (2.47) it can be shown that (Båth, 1968, p190),(Brekhovskikh, 1960, p190).

$$\frac{\mathrm{d}k_x \,\mathrm{d}k_y}{k_z} = k \sin\phi \cdot \mathrm{d}\phi \,\mathrm{d}\theta, \tag{2.48}$$

Thus the decomposition equation (2.46) is now written as:

$$\frac{\mathrm{e}^{ikR}}{R} = \frac{ik}{2\pi} \int_0^{\frac{\pi}{2}-i\infty} \int_0^{2\pi} \exp[i(k_x x + k_y y - k_z z)] \sin\phi \cdot \mathrm{d}\theta \,\mathrm{d}\phi, \qquad z \geqslant 0, \tag{2.49a}$$

and

$$\frac{\mathrm{e}^{ikR}}{R} = \frac{ik}{2\pi} \int_0^{\frac{\pi}{2}-i\infty} \int_0^{2\pi} \exp[i(k_x x + k_y y + k_z z)] \sin\phi \cdot \mathrm{d}\theta \,\mathrm{d}\phi, \qquad z \leqslant 0, \tag{2.49b}$$

noting that k_x, k_y and k_z are functions of θ and ϕ. Transforming the Weyl integral to polar coordinates yields the Sommerfeld integral for decomposition of spherical waves to cylindrical waves.

2.4 Conclusions

In this chapter the basic theory that is needed in the rest of this thesis has been presented. The key results are the decomposition of a spherical wave into plane wave components and the solution of the wave equation using such spherical waves. The wavefields presented in this thesis are processed in the horizontal-wavenumber–frequency domain, in which plane wave are separated. In this domain it is possible to separate compressional and shear modes if the local compressional and shear velocities are known.

MULTICOMPONENT MARINE BOREHOLE SEISMOLOGY

Chapter 3

3.1 Introduction

The aim of this chapter is to introduce the type of data considered in the thesis and the standard processing techniques usually applied. A short history of VSP experiment and processing is presented to provide a context for current developments in the field. A review of the relevant standard processing techniques and some examples of multicomponent VSP experiments follow. The chapter finishes with a description of walkaway VSP geometry and initial processing and a data example of the initial processing is presented.

3.2 A brief history of vertical seismic profiling

The first documented application of borehole seismology appears in a 1917 patent application (Fessenden, 1917). Figure 3.1 is diagram 2 from the patent application. Item 49 is the acoustic source and items 18 (left borehole) and 15 (right borehole) are acoustic receivers. Fessenden[1] states, "The vertical angle of reflection may be determined by hauling the transmitter or receivers up or down the drill holes.". These source and receiver geometries are similar to the crosshole and uniwell type experiments being developed today.

The development of borehole seismic technology outside the USSR was almost non-existent until the mid–1970s. Inside the Soviet Union, however, VSP research was significant from the early 1960's. The standard Russian text on VSP (Gal'perin, 1974) cites the start of serious interest at 1959; the original Russian book is Галвперин (1971). In 1980 there were about twenty times as many Soviet publications as Western VSP publications (Hardage, 1983).

The growth in VSP interest in the west turned in the 1980's with the beginning of academic

[1]Canadian Reginald A. Fessenden (1838–1932) was the first person to show that radio could be used to transmit anything other than Morse code signals. In 1901 he took part in the first transatlantic broadcast when he and Marconi, in Newfoundland, received the Morse letter S (· · ·) from Fleming in Cornwall. On Christmas Eve 1906 he successfully broadcast his voice and music and in November 1907 he achieved the first transatlantic voice communication between Brant Rock, Massachusetts, and Machrahanish, Scotland.

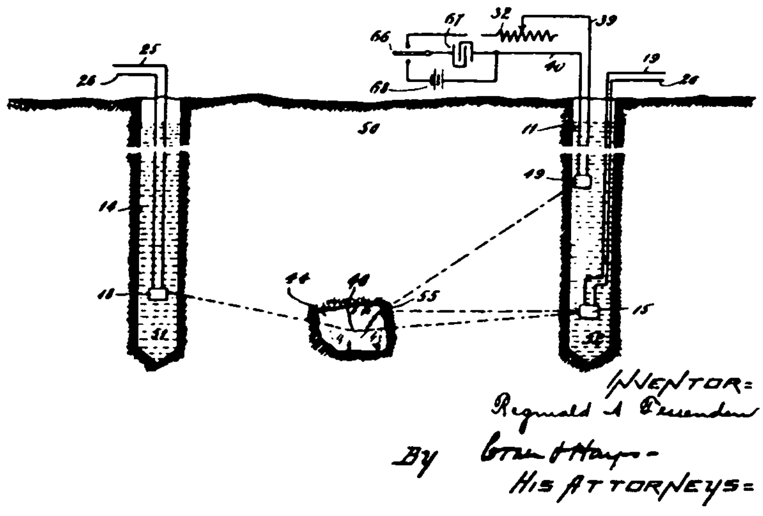

Figure 3.1: Reginald Fessenden's 1917 patent application, from Hardage (1983)

ties between the West and the USSR. In 1980 the (American) Southeastern Geophysical Society held a one–day workshop to increase awareness of this 'new technology' at which Gal'perin was a keynote speaker. In 1981 a workshop was held at the Massachusetts Institute of Technology which focused mainly on three-component technology, looking at seismic attenuation, the shear wave trains and fracture detection using seismic waves, subjects very much still current today. Since then VSP experiment design and processing has had a significant amount of attention. There has always been a close link between the anisotropy and VSP research communities. Three–component data have been routinely recorded for some time and three–component sources have sometimes been used allowing nine–component datasets to be collected. Such multicomponent datasets appeal to the anisotropy community as they better reflect the tensor nature of the seismic response of the earth.

3.3 Standard VSP processing techniques: a short review

In the mid 1980's VSP processing was based on modified surface seismic techniques. Lee (1984) describes a standard VSP processing flow, which is for a set of vertical measurements and a single source point. The development to a walkaway will come later. This VSP processing flow has the form:

1. wavelet shaping,
2. velocity filtering or wavefield separation,
3. downgoing wave deconvolution.

These are each considered briefly here.

3.3.1 Wavelet shaping

There are no papers available specifically on source signature–based initial VSP data processing. Many of the original VSP case studies mention some source monitor measurement–based processing but do not go into detail or discussions about the limitations of using such measurements. Kennet *et al.* (1980), of the Seismograph Services Limited (SSL) VSP group, use only vertical sensor data and assume only P-wave propagation. They present a VSP processing scheme with data examples. In these examples the first motions appear non-continuous suggesting that source variation problems exist but have not been addressed. This paper has no references to other work. A few years later Lee (1984) states in a VSP processing review paper that:

> [VSP] processing and interpretation is based on the assumption that the source wavelet is identical for all recordings at all depth levels. This is rarely the case. In fact, the source waveform is almost always different for every recording episode.

The problem of shot–to–shot repeatability and the problems shot variation introduces into VSP data were known in 1984 (Lee, 1984). In this paper the use of a source monitor is suggested and one of the waveforms recorded at this sensor is picked as the 'standard' waveform. Time domain filters are constructed to shape all other recorded source waveforms to this standard waveform and these same filters are then applied to the data traces. The paper presents a land VSP data example which has been wavelet–shaped to remove source variability. Such a scheme leaves the true source waveforms unknown. There is no discussion on how effective such a scheme is and the effect the source ghost has on the information recorded at the monitor. This ghost may mask some of the shot variation as recorded at the sensor. The monitor must also be a suitable distance from the source, outside any non-linear zone and free of ground roll (in the land case), of which no mention is made in the paper. Hardage (1983) p149 comments on stacking the data for Gaussian ($\sqrt{N}$) noise reduction with variable sources. This may be reasonable for marine sources as they are reasonably stable and so variations may be random, but for land sources this stability assumption is not good.

Tariel and Michon (1984), of the Compangnie Général de Géophysique (CGG) VSP group, also present a VSP processing paper in which they present the idea of deconvolving the upgoing wavefield using the downgoing wavefield. In this paper the source monitor data is used only to correct the first break times; no wavelet shaping is performed. The book by Hardage (1983) describes two approaches to source signature variation elimination. Wave shaping to a standard wavelet (Hardage, 1983, p202) of the measured signatures is qualitatively described but no examples are shown and no references are made to published work on wavelet shaping. A wavelet shaping scheme that does not rely on a measured source signature is also described in the book (Hardage, 1983, p32). The first breaks in the geophone data are aligned and an average wavelet computed by stacking all the recorded wavelets. A convolutional filter is constructed to make this average wavelet compact. This filter is then applied to the whole dataset. Dillon and Collyer (1985) consider first break picking in VSP data and mention a shaping scheme very similar to Higgins *et al.* (1997) but do not discuss its validity or make reference to other papers..

In the data presented in this thesis there is a source variation problem. This problem was not dealt with by the contractors. I cannot find any decisive work in the literature which discuses this problem in VSP processing. Higgins *et al.* (1997) presents a scheme for wavelet shaping using the source monitor data. This scheme is fully detailed in chapter 5 of this thesis. This may be a reinvention of a much earlier work by Zeitvogel[2] in which the problem of source variations causing apparent discontinuities in the measured wavefield is address by using measured source signature data.

3.3.2 VSP wavefield separation and deconvolution

In the borehole both upgoing and downgoing waves are recorded. Processing using a velocity filter scheme to separate these different wavefields then allows specific reflectors to be identified more clearly. Wavefield separation and filtering has formed a major part of VSP processing research because of its fundamental role in using VSP data to image the subsurface. Kommedal and Tjøstheim (1989) present a tutorial on different methods of VSP wavefield separation. They compare delay and sum methods with Fourier based frequency–wavenumber schemes and nonlinear median filtering. Some of the more common schemes are outlined briefly here.

An estimate of the downgoing wavefield $d(t)$ by *delay and sum*, given the ith trace $v_i(t)$ and the ith trace initial wave onset time t_i is

$$d(t) = \frac{1}{N}\sum_{i=1}^{N} v_i(t + t_i), \tag{3.1}$$

for N traces. Subtracting this estimate from the recorded wavefield yields an estimate of the upgoing wavefield $u(t)$. Effectively the first breaks are aligned in time and all traces then

[2]There are references to a Zeitvogel (1982) in Toksöz and Stewart (1984) but the full citation is missing from the book. The article is not in the journals Geophysics, Geophysical Prospecting or Geophysical Journal of the Royal Astronomical Society and a search for Zeitvogel on the SEG, Geobase, or GeoRef databases yields no articles other than Spencer *et al.* (1984), which is an abstract from the 1983 SEG conference. Seismology Abstracts for 1982 also has nothing for Zeitvogel.

summed to yield the downgoing wavefield estimate. Seeman and Horowicz (1983) pose this problem as a least–squares optimisation in the frequency domain, minimising the quantity $J(\omega)$

$$J(\omega) = \sum_{i=1}^{N} |V_i(\omega) - e^{i\omega t_i}U(\omega) - e^{-i\omega t_i}D(\omega)|^2, \tag{3.2}$$

where $U(\omega)$ and $D(\omega)$ are estimates of the upgoing and downgoing wavefields and $V_i(\omega)$ is the ith data trace. This scheme assumes a single downgoing and a single upgoing wave. The chief advantage of these type of schemes is that they do not require regular spatial sampling and the upgoing and downgoing waves do not have opposite moveout. Equation (3.2) show the downgoing and upgoing waves as having opposite moveout, as in the original paper. This is not a necessary condition; the filter can be parameterised for two wavefields with arbitrary moveouts. Moreover, the parameterisation can be expanded to deal with any number of wavefields.

For median filters instead of averaging, as in the delay and sum techniques, the statistical median of a number of traces in depth is computed after aligning traces by their first breaks. The median filter must have an odd number of points otherwise discontinuities are not preserved. The action of the filter severely attenuates upgoing waves and amplifies and smoothes the aligned downgoing waves. The number of points in the filter is dependent on how continuous the downgoing wavefield is. A detailed description with data examples is shown in Hardage (1983) pages 182–194. Median filters are nonlinear.

If the upgoing and downgoing waves have different moveout then they will be distinct in the (ω,k_z) domain. If the moveouts are opposite, applying a Gaussian pass filter in the frequency–wavenumber domain for either the positive or negative wavenumbers yields either the upgoing or downgoing waves. If the moveouts are not opposite it is still possible to filter VSP data in this domain to attenuate specific modes or velocity (or slowness) ranges using Gaussian fan filters (Hardage, 1983, pp 174–179). Filter design in this domain is dependent on the velocity of the desired wavefield.

The VSP convolution assumption is that, for zero offset convolution of the downgoing wavefield at a specific level with the reflectivity series below yields the upgoing wavefield at that level. If this is true then a deconvolution operator can be constructed from the downgoing wavefield to recover the reflectivity series from the upgoing wavefield on a trace–by–trace basis (Smidt, 1989; Kennet *et al.*, 1980). Such a scheme assumes single mode propagation, with no conversions and a one dimensional earth, thus only vertical component data is usually used. For zero–offset experiments it is reasonable to assume that there is no mode conversions, but this breaks down rapidly in the presence of steep cross–dip or in the presence of non azimuthally–symmetric anisotropy (Higgins and MacBeth, 1995). The work presented in this thesis is an extension of this idea to walkaway geometries allowing for mode conversions and using multicomponent data.

The processing scheme for offset VSP, where the source is at a fixed shot point some lateral distance from the receiver, is only slightly different. Converted waves are recorded on the horizontal and vertical components of the geophones. To utilise these data properly, correction must be made for tool rotation between deployment positions. One must now also correct for the source offset to get an equivalent zero–offset section; this is very similar to normal move-out correction in surface seismic data. The data can now be transformed to the common reflection point domain to image features away from the well. These processing steps require a velocity model of the earth and accurately–picked first–break times. Such experiments are discussed in Lee (1984). Lee (1984) suppresses the converted (S-)modes as an initial step.

A comprehensive discussion of VSP processing is in the book Hardage (1983) and multi-component advances of that time are discussed in the companion volume Toksöz and Stewart (1984), both part of the "Handbook of Geophysical Exploration" series.

3.3.3 Other considerations in VSP processing

Tube waves (DiSiena *et al.*, 1984a; Cheng and Toksöz, 1984) , often dominated by high frequencies, are a common feature in borehole data sections. They are identified by their distinctive moveout (apparent velocities in the range 1500m/s to 1600m/s). These waves correspond to (pseudo–Stoneley) interface–waves set up at the borehole–fluid-rock interface and are affected by changes in the borehole casing and surrounding rock structure. The suppression of these modes is often difficult. Geophone noise (Beydoun, 1984), clamping and cable noise have in the past been significant noise sources in VSP data (Hardage, 1983, p62). Today a full range of tests is carried out to make sure that the tools are well clamped and there is minimal cable and geophone noise. Sneddon (1998) has recently developed a velocity filtering technique for the suppression of tube–waves in uniwell data. The wave mode separation scheme presented in Chapter 6 is based on a velocity filtering approach to wavefield separation.

3.4 Examples of multicomponent experiments

Many examples of processing multicomponent VSP have been documented, most looking at the converted waves. Converted wave processing is considered in MacBeth *et al.* (1998) and the case of converted waves at near normal-incidence in MacBeth and Liu (1994a). Examples of the use of converted wave data are: rock property estimation, considered in Ahmed (1989), reservoir characterisation in MacBeth (1995) and shear wave splitting in the North

Sea, (Schruth *et al.*, 1992). The processing of vector wavefield data is reviewed in Wild *et al.* (1993). In 1989 the Society of Exploration Geophysicists (SEG, 1989) devoted an entire workshop to vector wavefield data, in which most of the case studies were VSP data examples.

The comparatively small scale but high cost of VSP experiments means they are designed with specific objectives in mind. The experiment geometry is dependent on the borehole for the positions of the sensors. This leads to many interestingly–designed experiments. A non-standard geometry is detailed in Dougherty *et al.* (1995) where they describe what they call an "Oblique seismic experiment". Unfortunately most of the useful data is in the direct P-wave coda. This experiment was one of the first 3D VSPs with the source boat moving in concentric circles. One of the first walkaway experiments is described in Ahmed *et al.* (1986).

3.5 Walkaway VSP geometry and data

Figure 3.2 shows a diagram of a single line walk away VSP experiment. The source and hydrophone are towed behind the boat. The ship track passes a safe distance from the rig, thus there is only a zero–offset shot point if the well is deviated. For a single line experiment the track is chosen to be perpendicular to the strike of the subsurface features, i.e cross-dip. A zero offset shot is desirable as the reflection sequence at vertical incidence is the most simple.

The geophones are in an equi-spaced array, commonly five or twelve receivers spaced at 15m intervals. The array may be pulled up the well and the line re-shot with the receivers in this new position; thus a larger array can be simulated. For a fixed (single) shot point VSP there is usually just a single geophone, pulled up the hole between shots. The receivers are free to rotate in the horizontal plane as they are pulled up–hole. They are gimbled so the vertical component remains vertical. The geophone packages are clamped to the borehole lining during shooting and it is assumed that the coupling is constant for all geophone positions.

There are two sets of data recorded: the receiver geophone and source measurements are recorded using different sensors and electronic filters. An outline of the recording scheme is shown in figure 3.3. In the diagram a triangle represents a filter (with an associated gain), while ADC represents analogue to digital conversion. TX and RX represent the radio transmitter and radio receiver for the source data. The source data are transmitted by radio from the boat to the rig where they are then recorded onto the same tape as the geophone data. The two sets of data are multiplexed.

The exact positions of the source and hydrophone are not recorded. A source position is stated in the data headers but this is a source suspension point relative to the mast of the source boat. The mast position is known using GPS. The direction the boat is travelling in and the distance

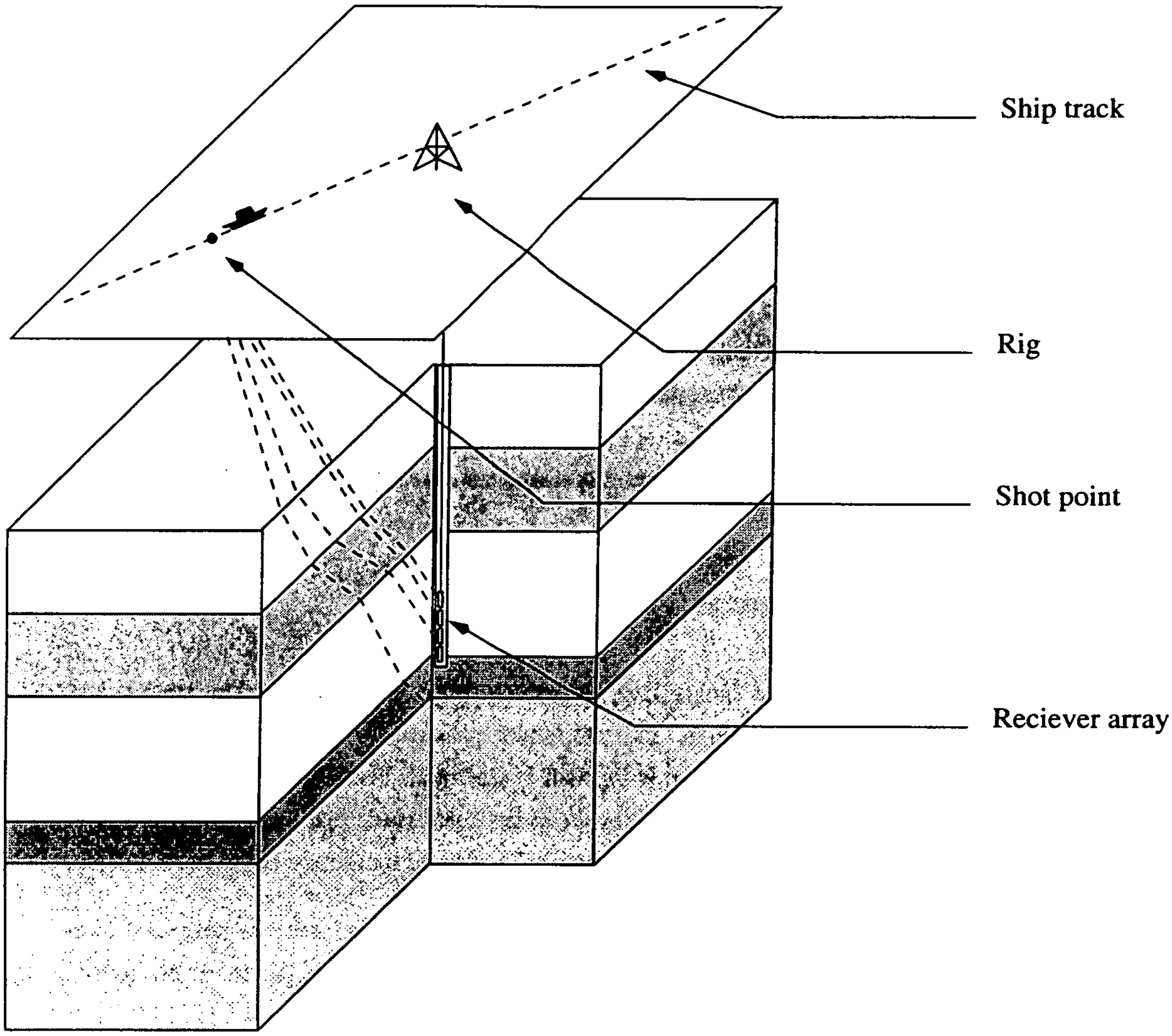

Figure 3.2: Single line walk–away VSP geometry

from the mast to the source suspension point (assumed to be constant) are used to calculate the recorded source position. The boat is steaming continuously during the experiment. The recorded source depth is normally the length of chain from the suspension buoys to the source rig, in this case 4m.

The geophone positions are given as depths in the well below the kelly bushing on the rig. These are converted to true depths using well deviation measurements. Measurement of the rotation of the horizontal sensors is possible using a gyroscope but such measurements are currently rare.

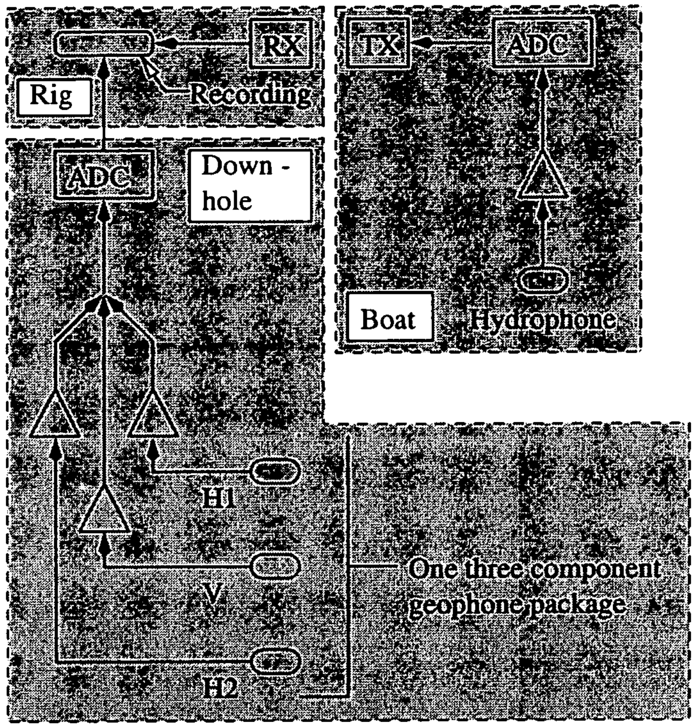

Figure 3.3: Outline of data recording scheme

3.6 The Elf dataset

The data presented in this thesis are from an experiment in the Norwegian sector of the North Sea. At the time this was part of one of the largest borehole seismic experiments undertaken. The geophone tool has five levels, shot in two positions. Only the upper position data are presented.

Table 3.1 and Figure 3.4 show the geometry from the data examples shown in this thesis. The geophones were deployed in a string of five three-component geophones. This string was deployed in two different positions (A and B in table 3.1) during the experiment. The source depth was measured relative to the sea surface and the geophone depths relative to the kelly bushing on the rig, which was 26m above the sea surface. Figure 3.5 shows common receiver gathers for the radial and vertical geophones. All traces are plotted at the same scale. The first arrival on the radial section is the projection of the P-wave. The initial processing that has been applied to these data is detailed in the following sections of this chapter.

Source depth (msl)	4m
Water depth	90m
Geophone depths (kb) A	3045 – 3105m
Geophone depths (kb) B	3120 – 3180m
Geophone interval	15m
Source offsets	-1680m – 3240m
Shot point interval	30m

Table 3.1: Walkaway VSP experimental parameters.

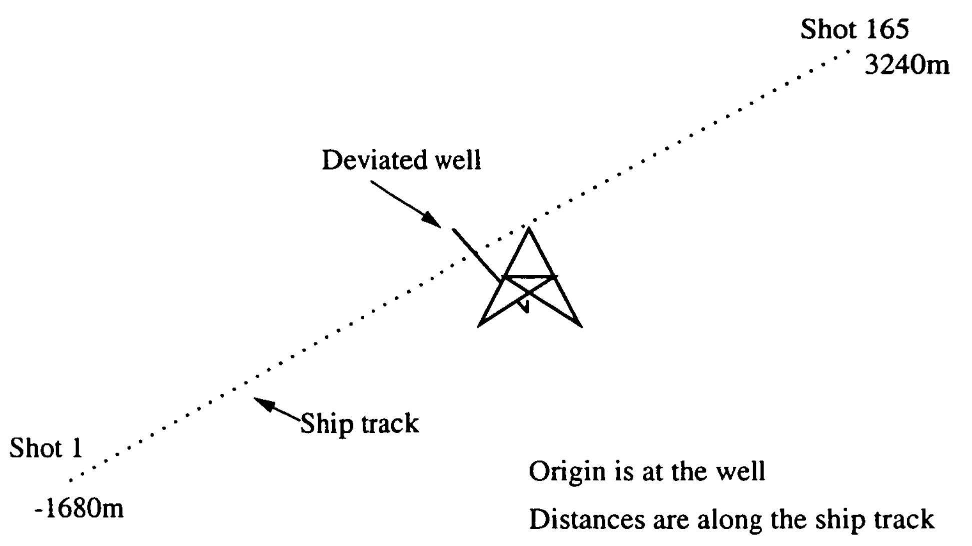

Figure 3.4: Schematic diagram of walkaway VSP geometry

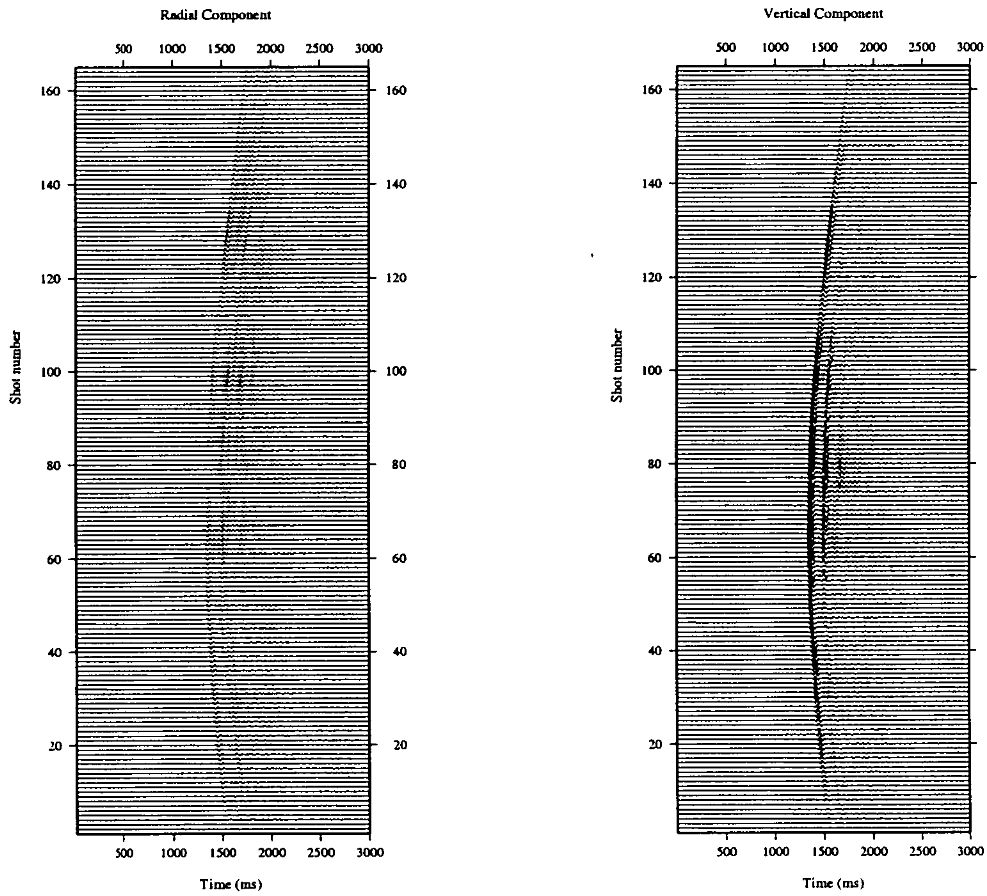

Figure 3.5: Radial and Vertical common receiver gathers, respectively

3.7 Initial processing of the data

There was some initial data manipulation processing carried out by the contractors. Precise details are not available, but they have demultiplexed the data, and applied a static correction to make sure all geophone traces have the same zero time relative to the first break on the source measurement. The down–hole recording devices are accelerometers. These data have been converted to particle velocity with the application of a phase shift of $\pi/2$, but no amplitude correction has been applied[3].

The data were recorded using three orthogonal sensors. The orientation of the sensors was fixed at each tool level. The particle velocity field at a (perfectly coupled) receiver is

$$\boldsymbol{v}(t) = v_x(t)\boldsymbol{n}_x \cdot G_x + v_y(t)\boldsymbol{n}_y \cdot G_y + v_z(t)\boldsymbol{n}_z \cdot G_z, \tag{3.3}$$

where $\boldsymbol{n}_{x,y,z}$ are the Cartesian basis vectors $v_{x,y,z}$ are orthogonal particle velocities and G_x,G_y and G_z are geophone gains. Ideally the gains are identical. For the data shown in this thesis it is assumed that this is the case as none of the geophone test data have been provided. This assumption is likely to be valid for the horizontal components G_x and G_y, as the same vertical force due to gravity acts on both of them. The vertical component is a different instrument as it is designed to detect motion in the same direction in which the gravitational force is acting. The result, is that the apparent horizontal or vertical velocities may be exaggerated in the receiver medium, thus affecting any velocity model. No problems of this kind are reported in the contractor's report so it is assumed either this has not been a problem or has been corrected in some (unknown) way[4]. This error is constant shot-to-shot.

The geophones may be oriented in any direction in the horizontal plane. This orientation is constant shot–to–shot as the geophones do not move. The orientation varies along the geophone string as the cable between tool housings twists during tool deployment. The vertical component is always vertical. The horizontal components are denoted $H1$ and $H2$, and there is a fixed angle which rotates $H1$ and $H2$ to be inline with the survey axes x and y.

The geophone data are rotated shot–by–shot to the dynamic coordinate system (Esmersoy, 1984, 1990). The radial direction is the direction that is horizontal and lies within the vertical source–receiver plane. The receiver is a positive distance from the source along the radial axis. The vertical direction is unchanged and the transverse direction is orthogonal to both the radial and vertical. These three directions form a right–handed coordinate system which is a pure rotation from the Cartesian system. The axes are denoted R, T, and V. Figure 3.6 shows the definition of this coordinate system. Note that the eigenvector axes point *towards* the source, which is at the origin of the wave–normal. The equation of rotation is (DiSiena

[3]This correction was applied by the contractors.

[4]correction for misalignment of the vertical geophone is difficult there is no linear rotation to correct the data.

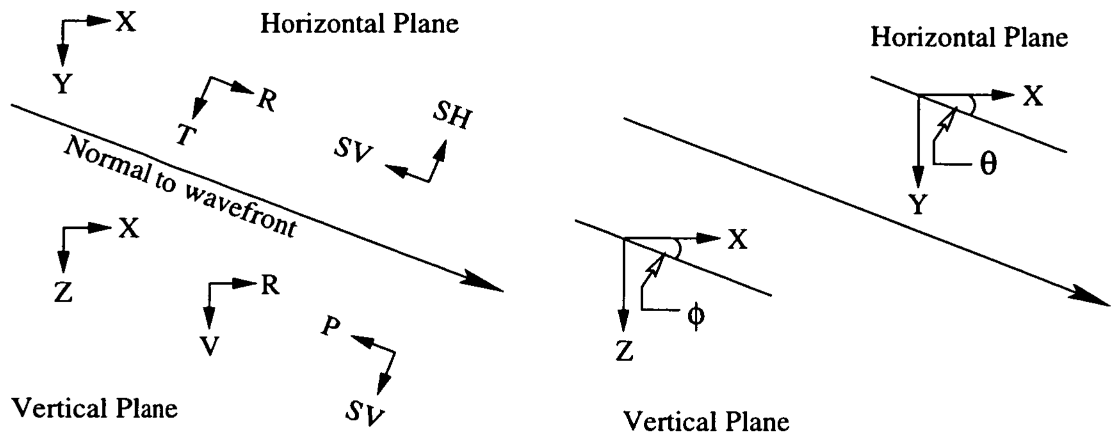

Figure 3.6: Definition of axes and angles of propagation

et al., 1984b)

$$\begin{bmatrix} u_R \\ u_T \\ u_V \end{bmatrix} = \begin{bmatrix} \cos\theta & \sin\theta & 0 \\ -\sin\theta & \cos\theta & 0 \\ 0 & 0 & 1 \end{bmatrix} \begin{bmatrix} u_x \\ u_y \\ u_z \end{bmatrix}, \tag{3.4}$$

where θ is the angle of rotation for a shot position. Figure 3.7 shows the horizontal rotation angles, in degrees, to rotate the geophone data from $H1$ and $H2$ to R and T for each shot point in the single line walkaway VSP. This definition of the radial direction assumes no

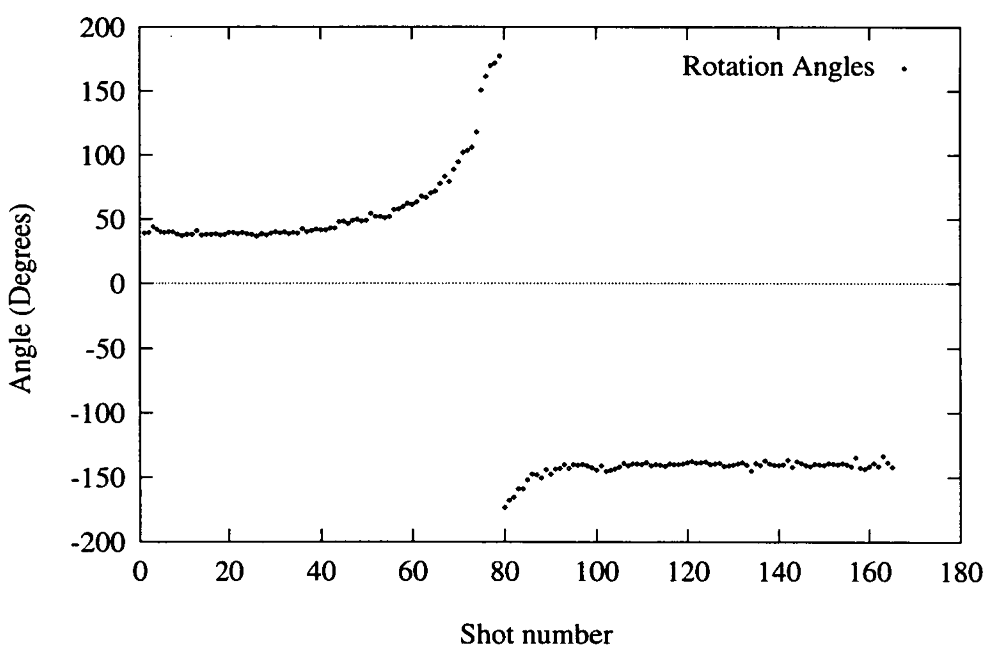

Figure 3.7: Horizontal plane rotation angles

cross-dip. The radial direction is the projected direction of the first P–wave motion in the horizontal plane. A time window about the P–wave first arrival is picked and the instantaneous component of the seismic power P_H in the horizontal plane is calculated thus:

$$P_{H,i}(\theta) \propto \left(H1_i^2 + H2_i^2\right), \tag{3.5}$$

where i is the sample number in the time window. The instantaneous angle ϑ is

$$\vartheta_i = \tan^{-1}\frac{H2_i}{H1_i}. \tag{3.6}$$

The instantaneous power has a maximum $P_{H,max}$ at some angle ϑ_{max} and this angle is the angle of $H1$ from R (Ahmed *et al.*, 1986). This assumes that the P–wave motion is linear. Figure 3.7 shows the rotation angles computed in this manner for the Elf dataset. For the near offset data there is little energy on the horizontal components, thus the peak power angle is less easy to pick. If there is cross–dip or non azimuthally symmetric–anisotropy then the radial direction computed from the initial P–wave motion is not contained within the source receiver plane.

The horizontal rotation angles can be predicted from the experimental geometry given the assumption of a plane–layered, azimuthally–isotropic earth (figure 3.8). The predicated angle

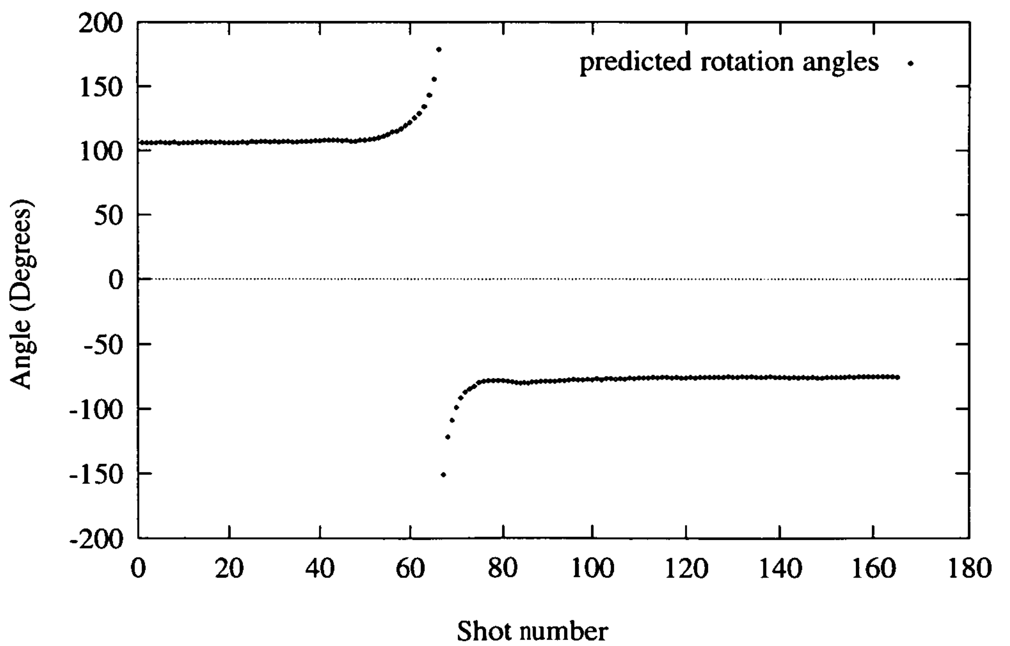

Figure 3.8: Predicted horizontal plane rotation angles

ϑ_p is given by

$$\vartheta_p = \tan^{-1}\frac{y_s - y_r}{x_s - x_r}, \tag{3.7}$$

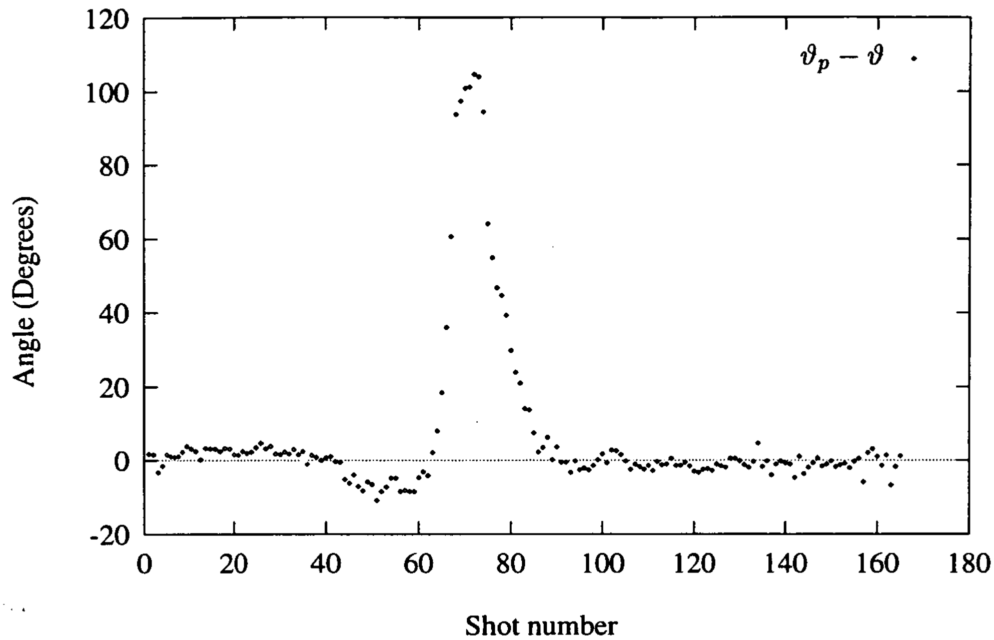

Figure 3.9: Difference in horizontal plane rotation angles

where the horizontal receiver position is (x_r, y_r). The average difference in the angle between the computed and measured rotation angles is $65^o(\pm 2.2^o)$. This average angle is computed using the offset shot–points, where the rotation angles are linear, Figure 3.7. This average angle is the angle of the receiver coordinates $(H1, H2)$ from the geometry coordinate system (x, y), a constant for each receiver throughout the experiment. Figure 3.9 shows the difference between theoretical and computed rotation angles for the Elf data with this constant removed. The peak in the plot occurs at near–offset; that is where there is very little energy on the horizontal components and so the signal–to–noise ratio is much higher than for far offsets. This makes the computation of angle unstable. One would expect the near–offset to be incoherent. The peak is due to a small error in the position of the receiver relative to the ship track. This error is constant shot–to–shot. If there is no error in the receiver position then there will be no coherent peak in the difference plot.

There is one other reference frame used in this thesis, the eigenvector frame. There are normally six solutions to the wave equation for a single wavenumber, corresponding to three up–going and three downgoing waves. For isotropy this is one compressional and two shear waves for each direction, where the compressional wave is coupled to a shear wave and the other shear wave is fully decoupled. It is possible to rotate the data to this eigenvector frame from the dynamic frame for a single plane wave thus:

$$\begin{bmatrix} u_{SV} \\ u_{SH} \\ u_P \end{bmatrix} = \begin{bmatrix} \cos\phi & 0 & -\sin\phi \\ 0 & 1 & 0 \\ \sin\phi & 0 & \cos\phi \end{bmatrix} \begin{bmatrix} u_R \\ u_T \\ u_V \end{bmatrix}, \tag{3.8}$$

where ϕ is the angle of the wave from the vertical. The rotation in the horizontal plane is accounted for during the rotation to the dynamic frame. Rotation to and from this frame forms the basis for P-wave and S-wave separation in the ω-k_r domain. Such a rotation cannot be carried out in the t-x domain as the rotation angle ϕ is slowness–dependent.

3.8 Real data section

Figure 3.10 shows the radial component for a walkaway VSP in the common–receiver domain. The data have been rotated to the dynamic frame but no other processing has been applied. The multiples can be clearly identified: the two–way time for vertically travelling waves in the water, depth 90m, is 120ms.

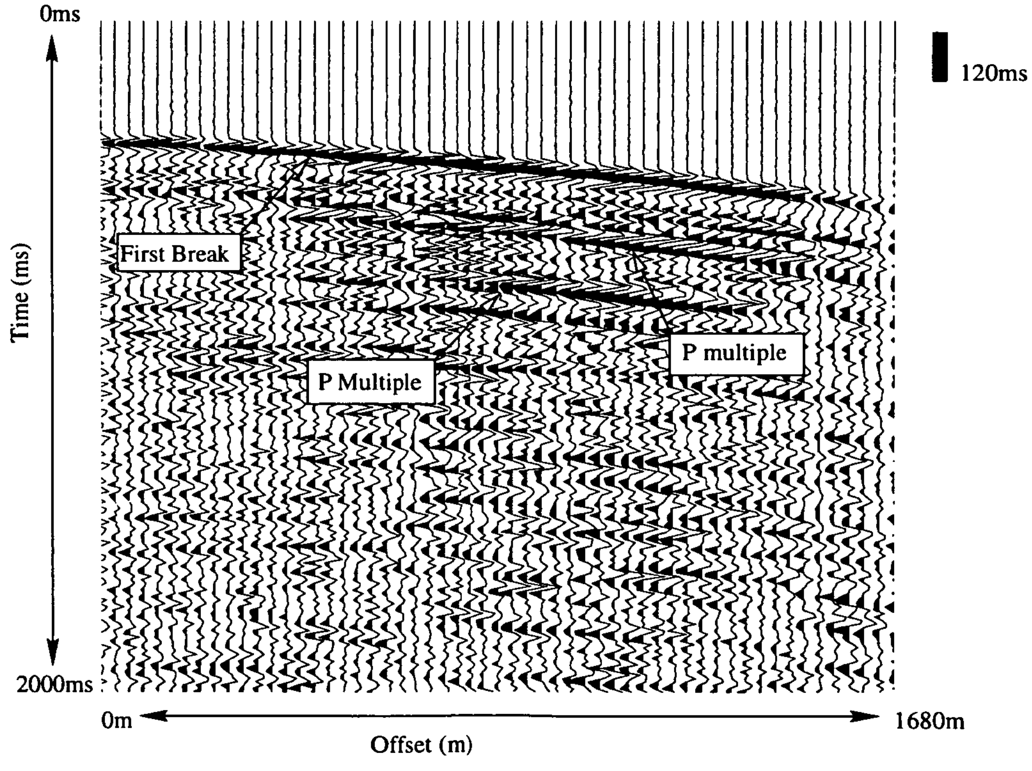

Figure 3.10: Annotated walkaway VSP section (radial component)

3.9 Conclusions

In this chapter a brief discussion of the most commonly used VSP processing techniques has been presented. Using the standard technique of rotation in the horizontal plane, using computed rotation angles, the data are rotated from the geophone coordinate system (H1, H2, V) to the dynamic coordinate system (R, T, V). The multiples can be clearly identified in the rotated data.

THE MARINE SEISMIC SOURCE: THEORY

Chapter 4

4.1 Introduction

For marine walkaway VSP seismic experiments the source is commonly a cluster of three 145 cubic inch airguns, fired at approximately 2000psi ($\approx$ 135atm). A measurement of this source is made using a single hydrophone usually between one and twenty metres from the source.

The aim of this chapter is to relate the marine source, its near field (pressure) measurement and the far field (particle velocity) wavefield recorded at the geophone. Source signature deconvolution is based on a convolutional model of wave propagation. Wave propagation near the source does not obey a linear wave equation. Parkes and Hatton (1986) develop the linear wave equation as an approximation to the full wave equation, but do not fully consider the effect of the approximations. Here the full non-linear acoustic wave equation is stated. The linearisation of this wave equation is discussed. Relationships between pressure measurements and the bubble radius and volume are also derived and discussed.

The physics of airgun bubble oscillation is not fully known; problems with simple models and solutions are qualitatively discussed. These problems do not affect the derivation of the wave equation or its solution for the case presented here of wave propagation at seismic frequencies.

The work in this chapter draws on Ziolkowski (1982) for the bubble physics, on Ziolkowski *et al.* (1982) for deconvolution relationships, on Lamb (1923) for the derivation of the full non–linear wave equation and the non-linear analysis and on Ziolkowski (1998) and Lamb (1923) for the linear and non-linear approximations to Lamb's wave equation.

4.1.1 The physics of an expanding and contracting bubble

Here the physics of an oscillating bubble is described and discussed. Knowledge of this physics allows better design and use of marine seismic sources.

The airgun acts as a source of gas. A spherical bubble of gas can be thought of as being an instantaneous initial volume V_i at initial pressure p_i and initial temperature T_i. The initial values for pressure and temperature are typically 135atm and 280K respectively. This pressure is far greater than hydrostatic pressure in the water, of order 1.5atm, and so there is a net outward force on the bubble wall causing it to expand. This expansion continues until the pressure inside the bubble is the same as the pressure outside the bubble, when there is no net force acting on the bubble wall. For shallow sources the hydrostatic pressure p is typically 1.5atm. As the bubble wall has momentum the bubble overshoots the equilibrium pressure radius, the pressure difference exerting a force radially inwards, thus slowing the bubble expansion and leading to compression. This oscillation continues until the bubble reaches thermodynamic equilibrium with the water. This model assumes a net stationary bubble. In reality the airgun has a horizontal velocity relative to the water and the bubble rises during oscillation due to the buoyancy of the bubble. Radiation from the bubble is Doppler–shifted in the frame of the water due to the horizontal motion.

Assuming that the gas in the bubble acts as an ideal gas of constant mass, the equation of state for adiabatic changes is of the form

$$pV^{\gamma} = \text{constant}, \tag{4.1}$$

where γ is the ratio of isobaric to isochoric[1] specific heat capacities. For a fixed mass of ideal gas the equation of state is

$$\frac{pV}{T} = \text{constant}, \tag{4.2}$$

where the constant in this relation and in (4.1) are not the same. Thus, using the subscript i to denote initial values,

$$\frac{p_i V_i}{T_i} = \frac{pV}{T} \qquad \text{and} \qquad p_i V i^{\gamma} = pV^{\gamma}. \tag{4.3}$$

Eliminating $\frac{V}{V_i}$ from these expressions yields:

$$T = \left(\frac{p_i}{p}\right)^{\frac{1-\gamma}{\gamma}} T_i, \qquad \text{which is} \qquad T = \left(\frac{150\text{atm}}{1.5\text{atm}}\right)^{\frac{1-1.4}{1.4}} 288\text{K} \approx 80\text{K} \tag{4.4}$$

for this example, assuming $\gamma = 1.4$ for adiabatic expansion of a diatomic gas. This final temperature of the bubble is extremely low, colder than the liquification temperature at this pressure of both molecular oxygen and molecular nitrogen. This is clearly not what happens inside real bubbles from airgun sources. Measurement (Ziolkowski, 1970) of airgun bubble oscillation periods suggests an empirical value of γ of 1.13, which gives $T \approx 170$K. Ziolkowski (1982) suggests a heat transfer mechanism that allows the mass of gas to change. In this paper it is also noted that modelled bubble oscillations tend to decay far more slowly than the acoustic radiation of measured bubbles. There is a damping mechanism which is

[1]constant volume

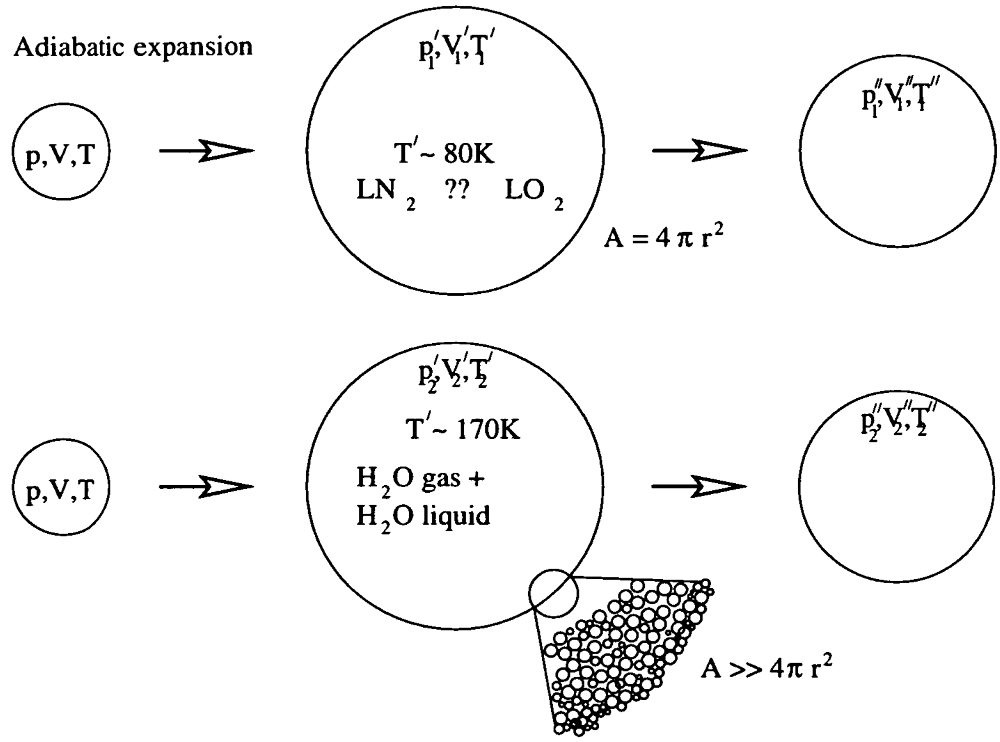

Figure 4.1: Comparison of adiabatic and more realistic bubble expansion models

not accounted for by such simple oscillating bubble models, suggesting there must be significant heat transfer across the bubble wall, in accordance with the first law of thermodynamics. Additional work must be done by the bubble wall to dampen the oscillation.

Figure 4.1 shows the mechanism proposed by Ziolkowski (1982). The bubble is not a volume of gas bounded by a smooth surface but made up of many small bubbles, dramatically increasing the surface area of the bubble, and thus the area available for heat transfer. In fact the bubble may not even be spherical (figure 4.2). The bubble expands, cooling the gas inside. Water vapour in the gas condenses, heating the gas as the latent heat of condensation is given up. The vapour pressure is very low so water vapour evaporates from the internal surfaces of the bubble wall, this vapour also condenses, heating the gas in the bubble. This damps the heating of the bubble. On compression, the gas temperature increases, water droplets evaporate, thus cooling the gas as they take up their latent heat. When the bubble temperature exceeds the surrounding water temperature the vapour inside the bubble condenses onto the bubble wall, thus heating the bubble wall and the surrounding water. This process damps the bubble oscillation, increasing the bubble period as is observed in real bubble oscillations. The net result is heat and mass transfer to the bubble from the surrounding water. This heat transfer and the emission of acoustic radiation is paid for by the initial potential energy imparted by the gun.

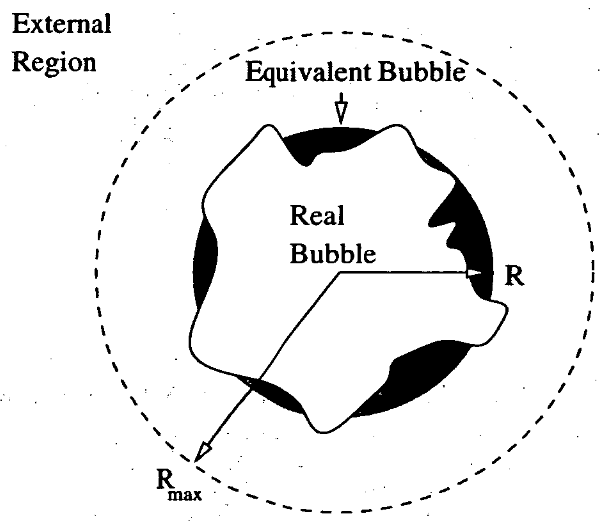

Figure 4.2: Definition of the equivalent bubble and external region.

This leads to the concept of an equivalent bubble. The equivalent bubble is the bubble which has exactly the same acoustic properties as the real bubble except that it is perfectly spherical. It is this equivalent bubble that we compute the seismic wavefield for. Figure 4.2 shows this concept. R is the radius of the equivalent bubble and R_{max} the maximum radius of the equivalent bubble. R_{max} may be of order 0.8m for a typical airgun[2]. The region outside the moving boundary R is where the following derivation of the wave equation is valid. This region is called the external region. There is heat transfer across the boundary of the equivalent bubble, but if the equivalent bubble boundary is increased by a small (few molecules) amount so that there is now a very thin layer of water inside the bubble then there is no longer be heat transfer across the new equivalent–bubble boundary. R now includes this thin layer. As the wavelength of the emitted acoustic radiation is much larger than the bubble size, this representation is valid.

4.2 The wavefield of a single bubble: Lamb's wave equation

Lamb's equation (Lamb, 1923) is the wave equation for a single oscillating bubble. It is not dependent on the internal physics of the bubble.

Consider an (equivalent) oscillating bubble. At the *origin* of the bubble the particle displacement is a meaningless quantity for a spherically symmetric bubble. The equivalent bubble is bounded by the bubble–wall which separates the gas from the surrounding liquid. The

[2]Say a 145 cubic inch airgun fired at 2000 psi, typical for marine VSP work. The bubble radius goes as the cube root of the gun volume and so is not too sensitive to changes in gun size.

displacement of the bubble *wall* is meaningful and it is this quantity that is calculated. The pressure *inside* the bubble $P(t)$ is assumed to be uniform. Pressure is continuous over the bubble wall; its (spatial) derivative, however, is not. The bubble radius is $R(t)$. The pressure is non–uniform *outside* the bubble wall. The bubble is assumed to be spherical and not interacting with the free–surface, that is, it is assumed that the bubble is in an infinite liquid and there is no gravitational field acting on the system. Figure 4.3 shows a diagram of the pressure

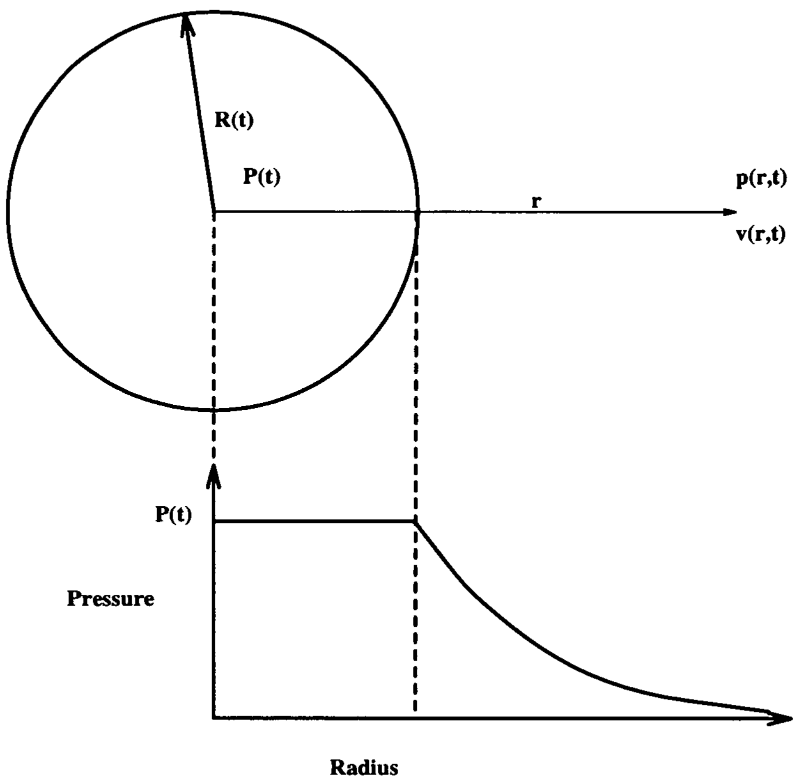

Figure 4.3: Sketch of bubble at some instantaneous time, t. After Ziolkowski (1998).

profile inside the bubble and the water.

The flow in the water is irrotational so the particle velocity $\boldsymbol{v}$ is just the gradient of the particle velocity potential ϕ, and the sign denotes positive work done to increase the particle velocity. That is:

$$\boldsymbol{v} = -\nabla\phi. \tag{4.5}$$

Lamb's equation is, (Lamb, 1923):

$$\frac{\partial^2\phi}{\partial r^2}\left(1-\frac{v^2}{c^2}\right)+\frac{2}{r}\frac{\partial^2\phi}{\partial r^2}\left(1+\frac{r}{c^2}\frac{\partial^2\phi}{\partial t\partial r}\right)-\frac{1}{c^2}\frac{\partial^2\phi}{\partial t^2}=0, \tag{4.6}$$

assuming spherical symmetry. This equation has no (known) analytical solution and so if this equation cannot be linearised then it cannot be solved without recourse to numerical techniques.

4.3 Linearisation and approximate solution of Lamb's equation

For all the experiments carried out in reflection and down–hole marine seismic experiments the fluid is water and the source of the pressure field is an air–gun. The approximations presented in Ziolkowski (1998) are designed for this case.

The linear acoustic approximation

At sufficiently large distance from the source one may assume that there is no difference in material and spatial description of the motion of the fluid; that is, the flow is the same in both the Lagrangian and Eulerian frames. This is the linear acoustic approximation. The linear wave equation is:

$$\frac{\partial^2\phi(r,t)}{\partial r^2}+\frac{2}{r}\frac{\partial\phi(r,t)}{\partial r}-\frac{1}{c^2}\frac{\partial^2\phi(r,t)}{\partial t^2}=0. \tag{4.7}$$

The wave equation has the well–known solution

$$\phi(r,t)=\frac{1}{r}f\left(t-\frac{r}{c}\right), \tag{4.8}$$

where $f(t)$ is the wavefunction. The wavefunction is related to the bubble volume V_B by (Ziolkowski, 1998):

$$f(t)=\frac{1}{4\pi}\frac{\mathrm{d}V_B(t)}{\mathrm{d}t}. \tag{4.9}$$

The incompressible flow approximation

The particle velocity is highest close to the bubble wall, therefore this is where the non-linear terms are most important. Assuming the the fluid is incompressible and the density is constant throughout the liquid, Bernoulli's equation for incompressible flow is (Lamb, 1923, equation 27):

$$h=\frac{\partial\phi}{\partial t}-\frac{v^2}{2}. \tag{4.10}$$

where h is the enthalpy[3]. The particle velocity potential and its derivative must be zero at infinite distance from the bubble wall and v is the magnitude of $\boldsymbol{v}$. Rayleigh (1917) deals with the collapse of a spherical bubble under the assumption of incompressible flow. Lamb (1923) showed that the nonlinear terms are negligible outside of the bubble for small underwater explosions.

4.4 Solving for pressure and particle velocity in the water

From the linear wave equation solution (4.8) and the velocity potential definition (4.5) the particle velocity in the water is (Lamb, 1923, equation 33):

$$v = -\frac{\partial \phi}{\partial r} = \frac{1}{r^2} f\left(t - \frac{r}{c}\right) + \frac{1}{rc} f'\left(t - \frac{r}{c}\right), \tag{4.11}$$

where f' is the spatial derivative of f. Following the appendix of Ziolkowski *et al.* (1982), consider the Fourier transform of $f(t)$:

$$F(\omega) = \int_{-\infty}^{\infty} f(t) \exp\{i\omega t\}\, \mathrm{d}t. \tag{4.12}$$

Adding a retarding phase factor[4] $\exp\{i\omega r/c\}$ yields:

$$F(\omega) \exp\{i\omega \frac{r}{c}\} = \int_{-\infty}^{\infty} f\left(t - \frac{r}{c}\right) \exp\{i\omega t\}\, \mathrm{d}t. \tag{4.13}$$

Noting that in the Fourier domain $\frac{\partial}{\partial t} \to -i\omega$ the transformed velocity $V(\omega)$ is, from equation (4.11):

$$V(\omega) = \frac{F}{r^2} \exp\{i\omega \frac{r}{c}\} - \frac{i\omega}{rc} F \exp\{i\omega \frac{r}{c}\}. \tag{4.14}$$

This can be written:

$$V(\omega) = \frac{F(\omega)}{r} \exp\{i\omega \frac{r}{c}\} \left[\frac{1}{r} - \frac{i\omega}{c}\right]. \tag{4.15}$$

Now $\omega = 2\pi f$ and $c = \lambda f$ so the above expression is

$$V(\omega) = \frac{F(\omega)}{r} \exp\{i\omega \frac{r}{c}\} \left[\frac{1}{r} - \frac{i2\pi}{\lambda}\right]. \tag{4.16}$$

The two terms in the square brackets are 90^o out of phase. Only the first term is distance dependent. In the near field $r \ll \frac{\lambda}{2\pi}$, thus the second term is negligible. So the particle

[3]energy per unit mass
[4]that is $f(t) \to f(t - r/c)$.

velocity in the near field is

$$v \approx \frac{1}{r^2} f\left(t - \frac{r}{c}\right). \tag{4.17}$$

By contrast in the far field $r \gg \lambda$ so the second term in (4.16) dominates, thus:

$$v \approx \frac{1}{rc} f'\left(t - \frac{r}{c}\right). \tag{4.18}$$

These are the expressions which relate the solution to the wave equation and the particle velocity in the near and far fields.

Considering the enthalpy the expression for the pressure in the near field is derived. From (4.8) and Bernoulli's equation (4.10) the enthalpy is:

$$.h = \frac{1}{r} f'\left(t - \frac{r}{c}\right) - \frac{v^2}{2} \tag{4.19}$$

The enthalpy can be expressed as (Ziolkowski, 1998, section 11):

$$h = \frac{p - p_\infty}{\rho_\infty}. \tag{4.20}$$

Thus (4.19) is

$$\frac{p - p_\infty}{\rho_\infty} = \frac{1}{r} f'\left(t - \frac{r}{c}\right) - \frac{v^2}{2}. \tag{4.21}$$

By (4.17), the near field velocity approximation, the v^2 term in (4.20) is

$$\frac{v^2}{2} = \frac{1}{r^4} f^2(t - \frac{r}{c}). \tag{4.22}$$

Ziolkowski and Johnston (1997) shows that, for distances greater than 1m the $v^2/2$ is negligible, and so the v^2 term can be then ignored. Thus, (4.19) is,

$$\frac{p - p_\infty}{\rho_\infty} = \frac{1}{r} f'\left(t - \frac{r}{c}\right). \tag{4.23}$$

This expression relates the pressure in the near–field (but further than 1m from the source) to the derivative of the wavefunction. It has the same shape as the particle velocity in the far field (equation (4.18)).

The hydrophone actually measures $p - p_\infty$ which is

$$p - p_\infty = \frac{\rho_\infty}{r} f'(t - \frac{r}{c}). \tag{4.24}$$

So the particle velocity observed in the far field has the same shape wavelet as the pressure in the water measured at 1m. Source signature deconvolution of far field particle velocity data using a near field pressure measurement is valid. If the hydrophone is calibrated then f' can be completely recovered. Ziolkowski (1998) presents a scheme to determine the pressure and volume of the equivalent bubble from a pressure measurement made in the water.

4.5 Conclusions

The full non-linear acoustic wave equation can be solved using approximations. These approximations are valid for the seismic case, as shown in Ziolkowski (1998). The linear near field pressure measurement has the same wavelet as the far field particle velocity, thus source signature deconvolution of down hole particle velocity data using such a measurement is a valid procedure.

SOURCE SIGNAL MEASUREMENT AND DECONVOLUTION

Chapter 5

5.1 Introduction

This chapter presents data which clearly show source signature variations. A method of deghosting these data is shown and the sensitivity of the deghosting scheme to variations in source depth is calculated. A method to remove the effect of the variations is presented and demonstrated on real data.

There is no work in the standard literature devoted to source signature deconvolution using measured source signatures for VSP data. The literature acknowledges that source variations do affect data processing and interpretation as discussed in Chapter 2. Specifically, for the work presented in this thesis, variations in source amplitude as a function of time introduce errors in the complex amplitudes in the wavenumber–frequency domain, thus introducing errors in the final result. Here a method of removing such variation using a deconvolution procedure is developed and discussed. The validity of the convolutional model has been established in the previous chapter.

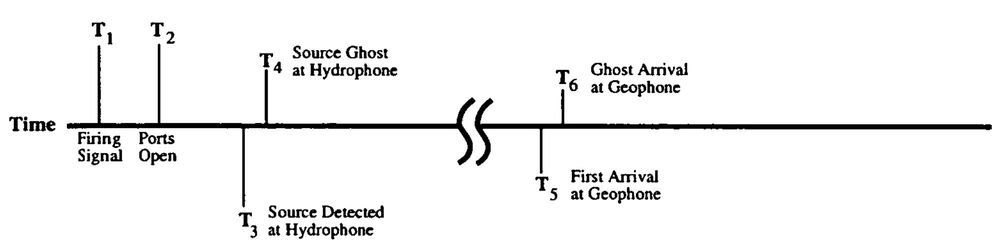

Figure 5.1: Timing Line; after Dillon and Collyer (1985)

5.2 Source Measurements

Figure 5.1 shows the relative timing for a VSP experiment. Interval arrival time estimation, from the geophone data, depends on the relative gun firing time being identical for each shot.

The gun firing time is the time at which the gun ports open T_2. The data are timed so that the gun electronic firing signal T_1 is the origin of the trace for each shot. The firing time is also known as the time break. The timing dependancies are shown in Figure 5.1.

	T1	T2	T3	T4	T5	T6
offset	✗	✗	✗	✗	✔	✔
source depth	✗	✗	✔	✔	✔	✔
geophone depth	✗	✗	✗	✗	✔	✔

Table 5.1: Timing dependencies

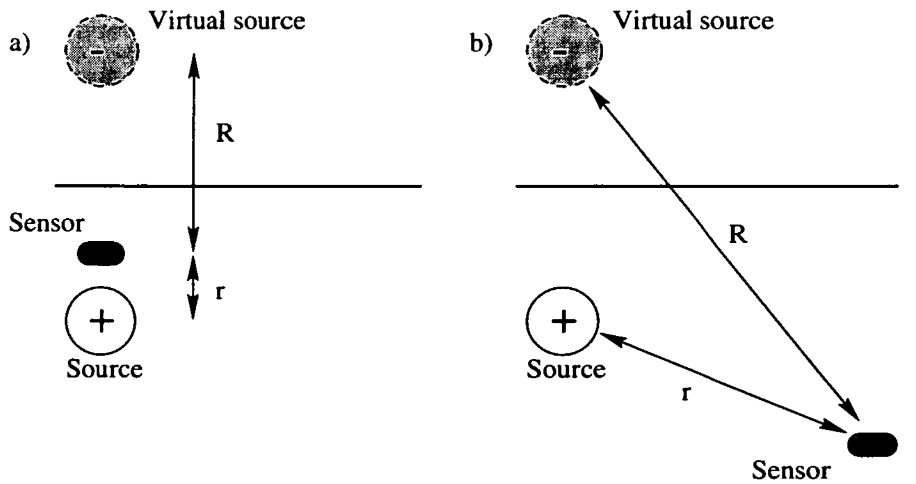

Figure 5.2: Geometry of source measurement.

Almost all VSP processing is based on the assumption of perfect shot–to-shot repeatability. Dillon and Collyer (1985) present a scheme for improving first break picking by wavelet shaping for such experiments. However they do not discuss the problem of source signature variation. Source estimation from geophone data is discussed in Hokstad *et al.* (1996) to get an effective source for reverse time migration; however, no mention is made of source signature variation and its effect on VSP migration. For processing in the wavenumber–frequency domain the problem is not one of relative timing but of how much a shot contributes to each plane wave component in this domain. For a monopole source in an infinite medium each frequency of the source contributes to all wave numbers with the same amplitude. The plane wave decomposition of the monopole source wavefield for each frequency (Båth, 1968) can be made. The decomposition is calculated using the horizontal array of sources. Each source must contribute equally to any wavenumber. If the source amplitude, for a fixed wavenumber, varies with each shot then the decomposition is erroneous. Figure 5.2 shows the common geometries for source signature measurement. The source–hydrophone distance is r and the ghost–hydrophone distance is R. Figure 5.3 shows measurements $m(t, x_s)$ of the source sig-

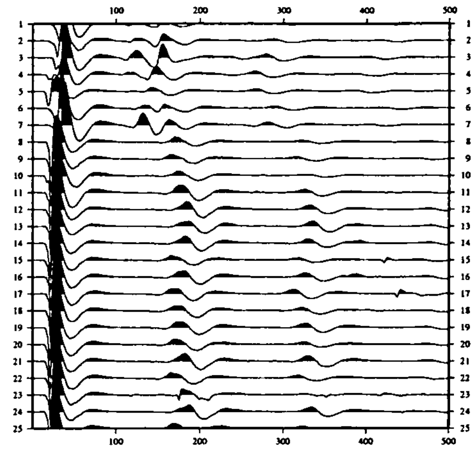

Figure 5.3: Measured Source Signatures

nature for twenty–five successive shots from a walkaway VSP experiment. The shot–to–shot source signature variation is obvious. Not only is there variation in the initial pulse but also in the bubble oscillation period, of the order of 20%. (Such a variation would be intolerable in seismic reflection data.) Figure 5.4 shows the same twenty–five traces as figure 5.3 but the

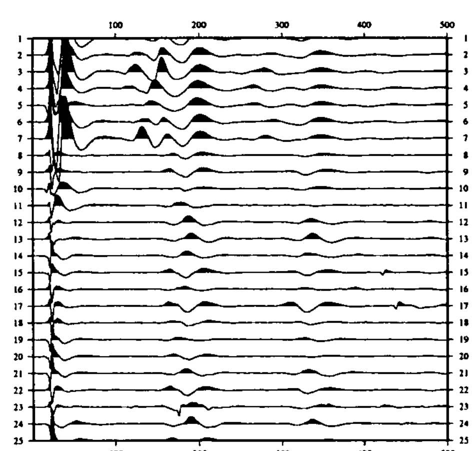

Figure 5.4: Measured source signatures with trace average subtracted

global trace average has been subtracted from each trace. Figures 5.3 and 5.4 are plotted on the same scale.

The assumption of perfect shot–to–shot repeatability is always invalid. In land VSP experiments the source signature changes shot–by–shot as the source interacts with its environment. In marine VSP the source is never in a fixed position relative to the sea–surface; any change in depth changes the bubble oscillation period (Parkes and Hatton, 1986). These changes in the source environment will always occur even if the mechanics of the source, on land or at sea, are identical shot–to–shot.

Using the scheme shown in this chapter this source of error can easily be removed from marine VSP data by wavelet shaping, provided the signature is properly measured. The quantity $m(t)$ is called the source signature measurement. The real source measurement is $m_{real}(t) = m(t) \cdot C$ where C is some calibration constant to convert from pressure to recorded voltage. For VSP this constant is commonly not known.

5.3 Source measurement deghosting

The ghost is the virtual image of the source in the sea surface. The ghost and source do not make up a dipole source, as the distance between the two poles (the source and its ghost) is not always small compared with the wavelength of the emitted radiation. The relative phase of the source and ghost are dependent on measurement position. Here it is assumed that the reflection from the sea bed is negligible in the source monitor data. For a 75m deep water column the sea bed is 100ms two–way time from the free surface. This is within the recording time of the source signature, typically 500ms. The amplitude of these arrivals is far below the noise in the recording as spherical divergence reduces these signals. This analysis assumes that the bubble is not moving relative to the hydrophone.

The (pressure) reflection coefficient of the sea surface is

$$R_c = \frac{\rho_a c_a - \rho_w c_w}{\rho_a c_a + \rho_w c_w} \tag{5.1}$$

where ρ_a and ρ_w are the densities of air and water respectively and c_a and c_w the acoustic velocities of air and water. At standard temperature and pressure this is

$$R_c = \frac{1.2 \cdot 330 - 1000 \cdot 1500}{1.2 \cdot 330 + 1000 \cdot 1500} = -0.9995, \tag{5.2}$$

Thus the reflection coefficient of the sea surface is -1 to within 1 part in one thousand. The sea surface therefore acts as a pressure–free surface, hence the description free surface.

The measurement $m(t)$ consists of arrivals direct from the source $s(t)$ and from the delayed reflection of the source $-s(t+\delta t)$. That is (Ziolkowski, 1991),

$$m(t) = \frac{1}{r}s\left(t-\frac{r}{c}\right) - \frac{1}{R}s\left(t-\frac{R}{c}\right). \tag{5.3}$$

This can be represented by a convolution in the time domain thus:

$$m(t) = s(t) \star \left[\frac{1}{r}\delta(t-\frac{r}{c}) - \frac{1}{R}\delta(t-\frac{R}{c})\right]. \tag{5.4}$$

The function $s(t)$ is the unretarded source time function. Transforming to the frequency domain and solving for the source function $S(\omega)$ yields

$$S(\omega) = \left[\frac{M(\omega)}{\frac{1}{r}\exp[\imath\omega\frac{r}{c}] - \frac{1}{R}\exp[\imath\omega\frac{R}{c}]}\right]. \tag{5.5}$$

It is possible to construct a deghosting scheme in the time domain. This may be done as bubble rise time can be easily built into the method by allowing r and R to be a function of time.

Before the ghost arrives the measurement consists only of direct arrivals.

$$m(t) = \frac{1}{r}s\left(t-\frac{r}{c}\right) \qquad t < \delta t, \tag{5.6}$$

where δt is the difference in direct and ghost arrival times. After the initial ghost arrival both direct and ghost arrivals are recorded at the sensor:

$$m(t) = \frac{1}{r}s\left(t-\frac{r}{c}\right) - \frac{1}{R}s\left(t-\frac{R}{C}\right) \qquad t \geqslant \delta t. \tag{5.7}$$

From this the source time function can be recovered. Before the ghost arrival $s(t)$ is simply

$$s(t) = m\left(t+\frac{r}{c}\right)\cdot r \qquad t < \delta t, \tag{5.8}$$

after the ghost arrival $s(t)$ is

$$s(t) = m\left(t+\frac{r}{c}\right)\cdot r - m\left(t+\frac{r}{c}-\delta t\right)\cdot R \qquad t < \delta t, \tag{5.9}$$

where

$$\delta t = \frac{R-r}{c}. \tag{5.10}$$

The data need to be resampled in order to make sure δt is, or is *close* to, being an integer multiple of the sample interval. This can be done by adding a zero pad at the Nyquist frequency in the frequency domain. The time domain data will be unaffected by this, apart from the increase in sampling frequency. (This assumes the data are not aliased)

Deghosting in the frequency domain is preferred to the time domain method as it is exact and the accuracy does not depend on the sample rate of the data, unlike the time domain method.

5.4 Sensitivity analysis

The deghosting is dependent on knowing c, r and R. The acoustic velocity is assumed to be 1500m/s. The acoustic velocity varies as a function of salinity and temperature. For shallow sea water the expected range is about 1460–1500m/s (Parkes and Hatton, 1986, p7). Over a distance of 10m this range causes a range of arrival times spread over 0.18ms, over 20m an arrival time range of 0.37ms. So, for source recording geometries that have a shallow source and hydrophone close to the source this is a negligible source of error.

The appendix shows the effect of considering first order variations in r and R. The error in r is zero as the hydrophone is fixed relative to the source. R will varies as a function of wave–height. Equation (5.5) is written :

$$\frac{M(\omega)}{S(\omega)} = \frac{\exp\{i\omega r/c\}}{r} - \frac{\exp\{i\omega R/c\}}{R} = T. \tag{5.11}$$

The appendix shows that, for this case, the first order error in T, computed by allowing R to vary by 1m, is less that 1% at 100Hz. The error decreases with decreasing frequency. Thus the error in R is negligible, so a constant value of R can be used for the deghosting.

The deghosting operator is a convolutional phase factor, which does not affect the wavelet shaping scheme described in the rest of this chapter. The measured particle velocity $v(t)$ is

$$v(t) = g(t) * s(t) = g(t) * m(t) * f(t), \tag{5.12}$$

where $g(t)$ is the impulse response of the earth and $f(t)$ is the deghosting filter. The source measurement deghosting must be performed before trace mixing or stacking.

5.5 Theory and application of measured wavelet shaping

Here the theory for the design and application of a filter to suppress the shot–to–shot variation is developed and applied. This follows Ziolkowski (1991) which uses measured source signatures for deconvolution of surface seismic data.

The generalised measurement geometry is shown in Figure 5.2. For a single receiver walkaway VSP the geophone data are particle velocities $\boldsymbol{v}(t, \boldsymbol{x}_r)$ recorded as a function of time t and receiver position $\boldsymbol{x}_r$. The source signature is a function of time and shot position, $s(t, \boldsymbol{x}_s)$. The impulse response of the earth is a function of time as well as geometry: $\boldsymbol{g}(t, \boldsymbol{x}_s, \boldsymbol{x}_r)$. In the frequency domain the particle velocity measurement, source function and impulse response are related as:

$$\boldsymbol{V}(\omega, \boldsymbol{x}_r) = \boldsymbol{G}(\omega, \boldsymbol{x}_s, \boldsymbol{x}_r) \times S(\omega, \boldsymbol{x}_s) + N(\omega, \boldsymbol{x}_r), \tag{5.13}$$

where the capitals denote the change of domain and $N(\omega, \boldsymbol{x}_r)$ is the noise recorded at the geophone.

There is a single source pressure measurement $m(t)$ for a single shot made at a hydrophone a distance r from the source and R from its virtual image. A filter $F(\omega, \boldsymbol{x}_s)$ is required such that $S(\omega, \boldsymbol{x}_s)$ is shaped to a desired function $D(\omega)$, which is *not* shot–dependent. $D(\omega)$ is the Fourier transform of the desired wavelet $d(t)$. After filtering, all the shots have the same source signature $d(t)$. The filter is defined as

$$F(\omega, \boldsymbol{x}_s) = \frac{D(\omega) S^*(\omega, \boldsymbol{x}_s)}{|S(\omega, \boldsymbol{x}_S)|^2 + \epsilon} \quad , \tag{5.14}$$

where $D(\omega)$ is chosen such that the desired source wavelet $d(t)$ is shorter than $s(t)$. The desired wavelet has approximately the same bandwidth as the original source wavelet so that the modulus of $F(\omega, \boldsymbol{x}_s)$ is approximately one. The quantity ϵ is a small constant for stabilisation of the operator in the presence of noise. Finally the impulse response of the earth is:

$$\boldsymbol{G}(\omega, \boldsymbol{x}_s, \boldsymbol{x}_r) \cdot D(\omega) = \boldsymbol{V}(\omega, \boldsymbol{x}_r) \cdot F(\omega, \boldsymbol{x}_s) - F(\omega, \boldsymbol{x}_s) \cdot N(\omega, \boldsymbol{x}_s). \tag{5.15}$$

As the filter magnitude is approximately unity the signal–to–noise is almost unchanged. This filter is applied to the geophone data. The shot–to–shot variability is removed from the VSP data.

For this application example the source depth is 4m and the hydrophone is fixed 1m above the source, as shown in Figure 5.2. The hydrophone is so close to the source that the recorded source signature is dominated by the direct arrival and the sea bottom reflections can be ignored. Figure 5.5 shows a typical source wavelet before and after wavelet shaping has been carried out. All the sources are shaped to this final wavelet.

The calculated filter $F(\omega, \boldsymbol{x}_s)$ is transformed to the time domain, $F(\omega, \boldsymbol{x}_s) \mapsto f(t, \boldsymbol{x}_s)$. To ensure that $f(t, \boldsymbol{x}_s)$ is causal the desired wavelet $d(t)$ is delayed in time. In this case the delay is 128ms. This lagged filter is shown is Figure 5.6. All the filters are lagged by the same amount. The filters are applied to the source and geophone data as convolutions in time, so

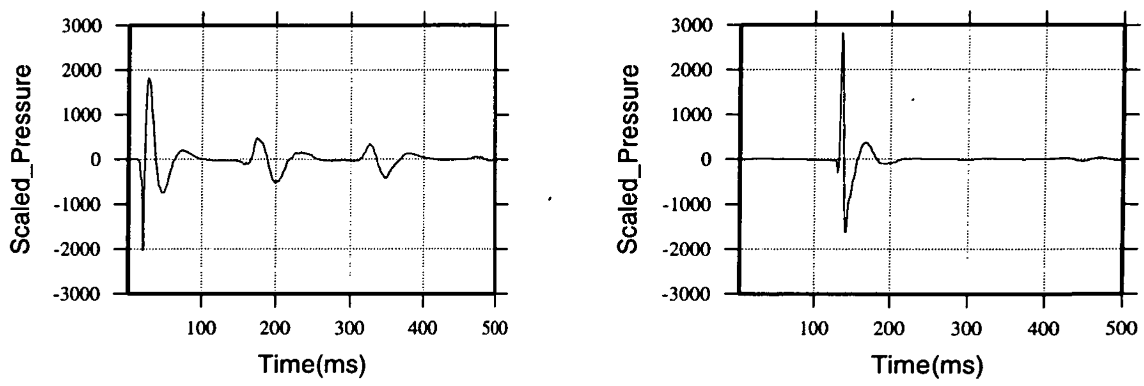

Figure 5.5: Source signatures A) before and B) after wavelet shaping

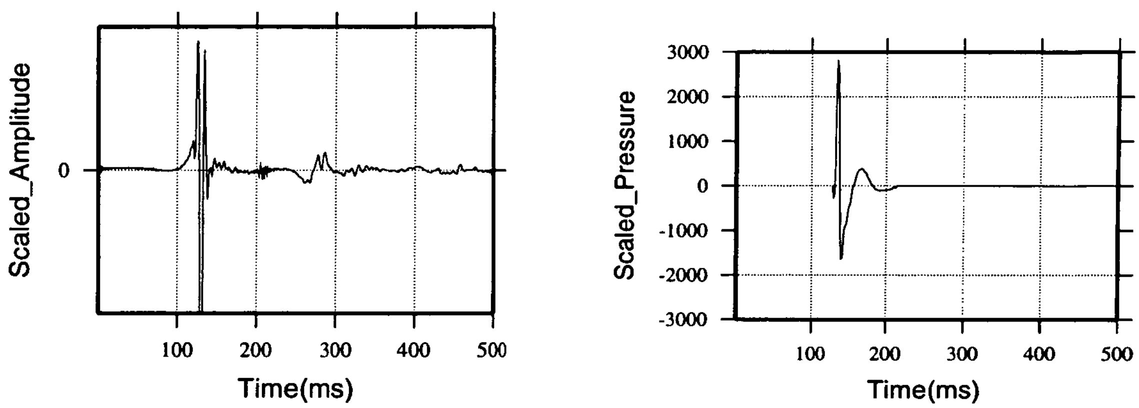

Figure 5.6: A) Time domain wavelet shaping filter and B) desired wavelet

the final data are also delayed by 128ms. The desired wavelet is shown in Figure 5.6. The actual output wavelet is slightly different from the desired output wavelet. In practice the filter is designed so that it is relatively smooth and so does not perfectly reproduce the desired wavelet. The difference can mainly been seen in the later portion of the wavelet and is small. The polarity of the desired wavelet is reversed compared to the input wavelet.

Figures 5.7 and 5.8 show the vertical component of the geophone data before and after processing. The shots are 30m apart and the geophone is at a depth of 3km. (Shot 77 was a mis–fire)

The same filters are applied to the radial and transverse components of the geophone data. The continuity of events is clearly improved by this process. This scheme can be applied to other VSP geometries with no modification.

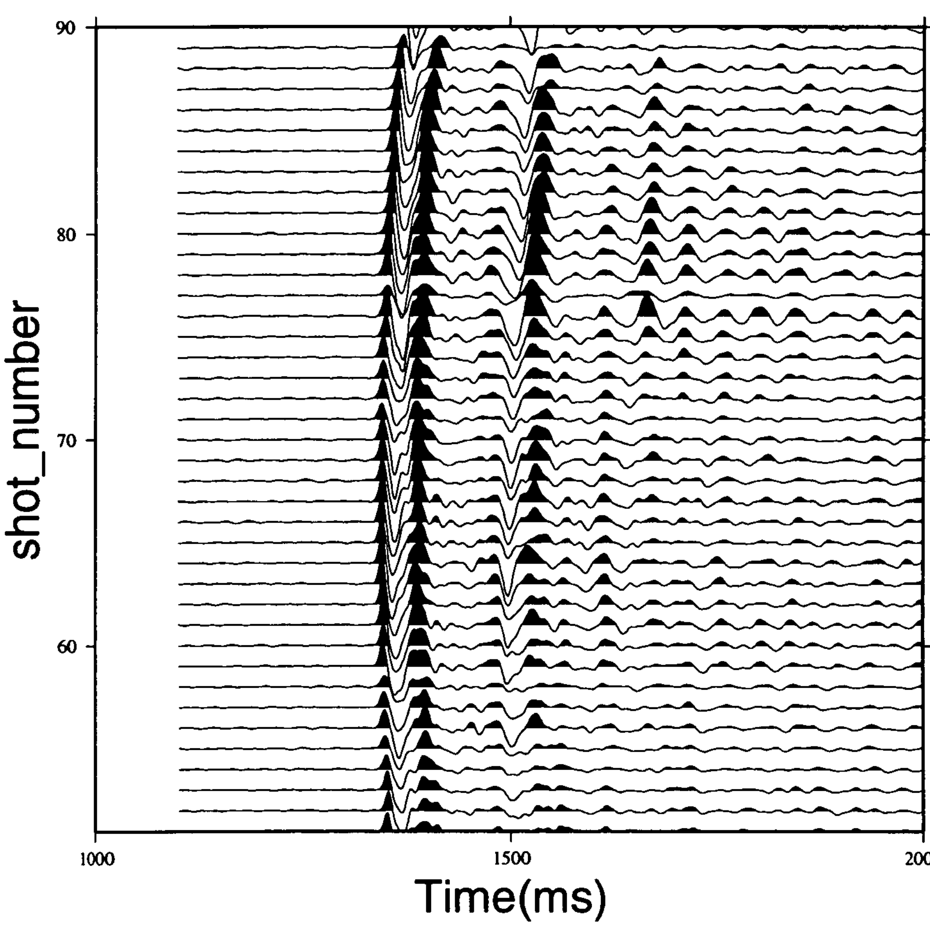

Figure 5.7: Vertical geophone data before wavelet shaping

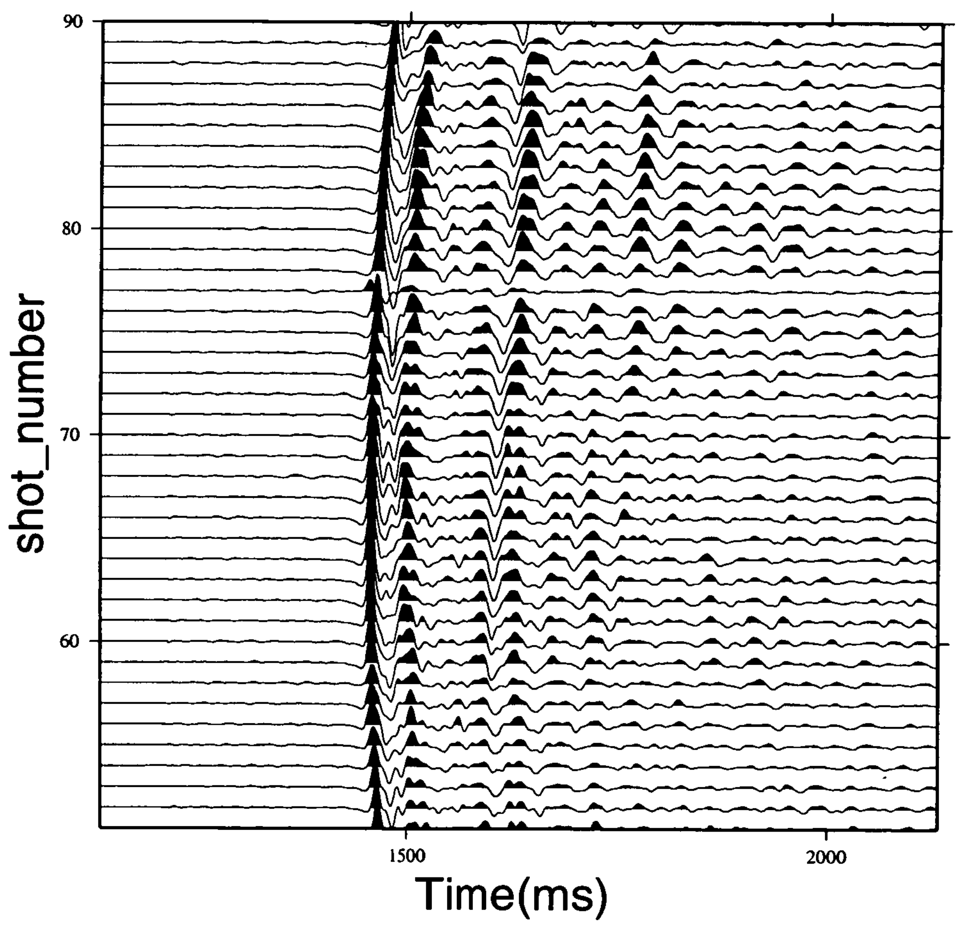

Figure 5.8: Vertical geophone data after wavelet shaping

Discussion and conclusions

If such a scheme is added to the VSP processing sequence there are practical issues to be considered. The geophone and hydrophone data should ideally be recorded through the same electronic filters. If this is not possible, the responses of the two sets of filters must be known. The two quantities R and r must also be known. That is, the position of the hydrophone relative to the source and the source depth must be known. Estimation of these quantities introduces errors.

It is well known from measurements that there is significant shot–to–shot variation in the source signature. Current VSP processing schemes usually ignore this, thus introducing errors. I propose that the source signature should be measured properly such that the shot–to–shot variations are eliminated using this scheme. Then conventional VSP processing can be applied without these sources of error.

RECOVERING THE REFLECTIVITY: THEORY

Chapter 6

6.1 Introduction

In this chapter the equations for recovering the reflectivity beneath the receiver in the (ω, k_x, k_y) domain are derived. The derivation relies on the expression of the entire wavefield at the receiver for a single plane wave component. The reflectivities are recovered by division and the practicalities of carrying out the division are discussed. The recovered reflectivities are converted into wavefields for transformation back to the time–space domain.

6.2 The wavefield at the receiver

Consider a three–component walkaway VSP experiment over a horizontally plane–layered earth isotropic. The receiver is at $(0, 0, z_r)$ and the ith source is at (x_i, y_i, z_s), where z_s is fixed. The source is isotropic, and only SV-P waves are propagating. The upper boundary condition is a (vertical) stress–free surface and the lower boundary condition is the radiation condition. The measured particle velocity data–volume as a function of time is $v_j(x_i, y_i, z, t) = \boldsymbol{v}$, where $j = 1, 2$ corresponding to the two orthogonal receivers in the 1 (radial) and 2 (vertical) directions (the dynamic frame). The transverse direction is not considered as there is no SH propagation or out–of–plane propagation. For a laterally–invariant earth this is equivalent to a single source at $(0, 0, z_s)$ and a horizontal plane of receivers at (x_i, y_i, z_r).

Transforming $\boldsymbol{v}$ to the (ω, k_x, k_y) domain yields

$$\hat{\boldsymbol{V}}(k_x, k_y, z_r, \omega) = \iiint_{-\infty}^{\infty} \boldsymbol{v}(x, y, z_r, t) \exp\{i(\omega t - k_x x - k_y y)\} \, \mathrm{d}t \; \mathrm{d}x \; \mathrm{d}y. \tag{6.1}$$

In this domain plane wave components are separated, as shown in Chapter 2.

The full wavefield, for a single plane wave component, at $z = z_r$, where $z_r > z_s$ and z_s and

$V(z_R)$	Particle velocity two–vector
m_D^R	2x2 matrix to convert down going P and S amplitudes to displacements
m_U^R	2x2 matrix to convert up going P and S amplitudes to displacements
R_D^{RL}	2x2 reflectivity matrix of whole region beneath the receiver
$[I - R_U^{RF} R_D^{RL}]^{-1}$	Reverberations across the receiver level
I	The 2x2 identity matrix
R_U^{RF}	Reflectivity of the region between $z = r$ and the $z = 0$ for upgoing waves
T_D^{RS}	Transmission matrix for down going waves between the source and receiver
$[I - R_U^{FS} R_D^{SL}]^{-1}$	'The multiples'
R_U^{FS}	Reflectivity of the whole region above the source
R_D^{SL}	Reflectivity of the whole region below the source
Σ_D^S	Down going source amplitude $[\psi_D, \phi_D]^T$ ϕ is P radiation and ψ is S
Σ_U^S	Up going source amplitude $[\psi_U, \phi_U]^T$

Table 6.1: Terms in equation (6.2)

z_r are in different layers, is (Kennett, 1983, equation 7.38);(Kennett, 1981, equation 4.36)

$$\begin{aligned} \hat{V}(z_r) =& (m_D^R + m_U^R R_D^{RL}) \\ & \times [I - R_U^{RF} R_D^{RL}]^{-1} T_D^{RS} \\ & \times [I - R_U^{FS} R_D^{SL}]^{-1} (\Sigma_D^S - R_U^{FS} \Sigma_U^S). \end{aligned} \tag{6.2}$$

This equation describes the entire particle velocity wavefield V at the receiver for a single plane wave component. The terms are described in table (6.1). This description of the wavefield is well known.

Figure 6.1 shows which regions of the elastic layer space each term in the wavefield equation represents. The source vectors are not shown in this diagram.

The reflectivity matrices R contain all intrabed multiples that are possible for the regions

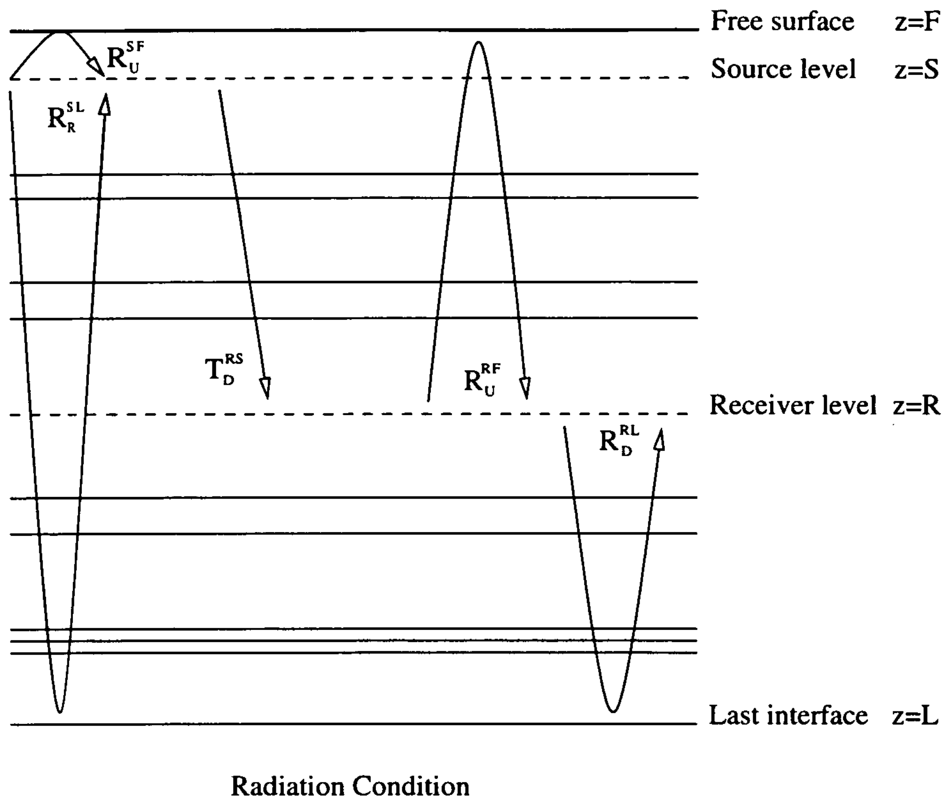

Figure 6.1: Terms in equation (6.2)

which they describe. These expressions are valid for single points in the frequency, horizontal–slowness domain for an azimuthally–isotropic earth.

Let $\beth$ be defined as:

$$\beth = [\boldsymbol{I} - \boldsymbol{R}_U^{RF}\boldsymbol{R}_D^{RL}]^{-1}\boldsymbol{T}_D^{RS} \times [\boldsymbol{I} - \boldsymbol{R}_U^{FS}\boldsymbol{R}_D^{SL}]^{-1}(\boldsymbol{\Sigma}_D^S - \boldsymbol{R}_U^{FS}\boldsymbol{\Sigma}_U^S). \tag{6.3}$$

This quantity $\beth$ (Hebrew letter Beth) is a two-vector of the form $[\beth^S, \beth^P]^T$; it contains all parts of the wavefield that contain any information about the region above the receiver. Thus, (6.2) may be written:

$$\boldsymbol{V}(z_r) = (\boldsymbol{m}_D^R + \boldsymbol{m}_U^R\boldsymbol{R}_D^{RL})\ \beth. \tag{6.4}$$

Writing the upgoing and downgoing wavefields in (6.2) separately yields,

$$\boldsymbol{V}_D(z_r) = \boldsymbol{m}_D^R\beth, \tag{6.5a}$$

and

$$\boldsymbol{V}_U(z_r) = \boldsymbol{m}_U^R \boldsymbol{R}_D^{RL} \sqsupset. \tag{6.5b}$$

Multiplying the left–hand side of each of these equations by the inverse of the respective transfer matrix yields:

$$\left[\boldsymbol{m}_D^R\right]^{-1} \boldsymbol{V}_D(z_r) = \sqsupset, \tag{6.6a}$$

and

$$\left[\boldsymbol{m}_U^R\right]^{-1} \boldsymbol{V}_U(z_r) = \boldsymbol{R}_D^{RL} \sqsupset. \tag{6.6b}$$

For brevity $\boldsymbol{R}_D^{RL}$ is now denoted simply $\boldsymbol{R}$, $\boldsymbol{m}_U^R$ is denoted $\boldsymbol{m}_U$ and $\boldsymbol{m}_d^R$ is denoted $\boldsymbol{m}_D$.. It should be noted that these three quantities are dependent on the receiver depth.

6.3 The transfer matrices, $\boldsymbol{m}_{U|D}$

The $\boldsymbol{m}_{U|D}$ terms are the rotations from the eigenvector frame to the dynamic frame, which are radial and vertical slowness dependent. The inverses of the transfer matrices, denoted $\boldsymbol{n}_{U|D}$, rotate the particle motion from the dynamic frame to the eigenvector frame. That is the inverse matrices decompose radial and vertical particle motions into compressional and shear particle motions. Here angles are measured relative to the horizontal. A wave travelling along the source array has an angle of propagation of 0^o, and a wave travelling perpendicular to the source array an angle of propagation of 90^o.

The radial slowness is related to the radial wavenumber by

$$p_r = \frac{k_r}{\omega}, \tag{6.7}$$

which is denoted p, k_r is real for all data points and here p is always positive. The P-wave and S-wave vertical slownesses are

$$q_\alpha = (\alpha^{-2} - p^2)^{1/2}, \tag{6.8}$$

and

$$q_\beta = (\beta^{-2} - p^2)^{1/2}, \tag{6.9}$$

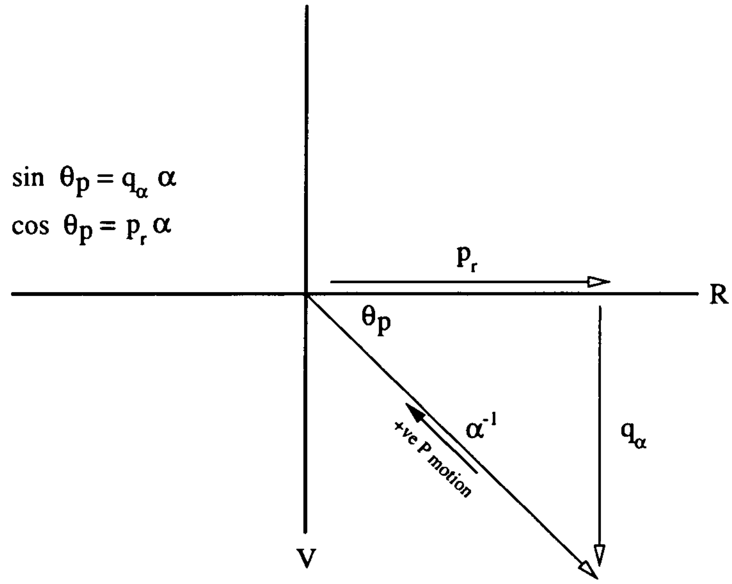

Figure 6.2: P-wave decomposition to dynamic frame

respectively. The radial slowness is real if both ω and k_r are real for all data points. The vertical slownesses are complex when p exceeds $1/\alpha$.

Figure 6.2 shows a downgoing P-wave and the sine and cosine of the propagation angle as a function of horizontal or vertical slowness; the source is at the origin. The vertical and horizontal particle velocities in the dynamic frame are:

$$v_{D,pv} = -P_D \cdot \sin\theta_p, \tag{6.10a}$$

$$v_{D,pr} = -P_D \cdot \cos\theta_p, \tag{6.10b}$$

where P_D is the complex amplitude of the downgoing compressional wave in the eigenvector frame and θ_p is the angle to the horizontal. Positive P–wave motion is defined as being in the source direction, hence the quantities in equations (6.10) are negative. Substituting in the sine and cosine definitions yields

$$v_{D,pv} = -P_D \cdot q_a \cdot \alpha, \tag{6.11a}$$

$$v_{D,pr} = -P_D \cdot p_r \cdot \alpha. \tag{6.11b}$$

For upgoing waves the sign of the vertical particle motion only is reversed,

$$v_{U,pv} = P_U \cdot q_a \cdot \alpha, \tag{6.12a}$$

$$v_{U,pr} = -P_U \cdot p_r x \cdot \alpha. \tag{6.12b}$$

and the horizontal particle motion is unchanged; P_U is the complex amplitude of the upgoing

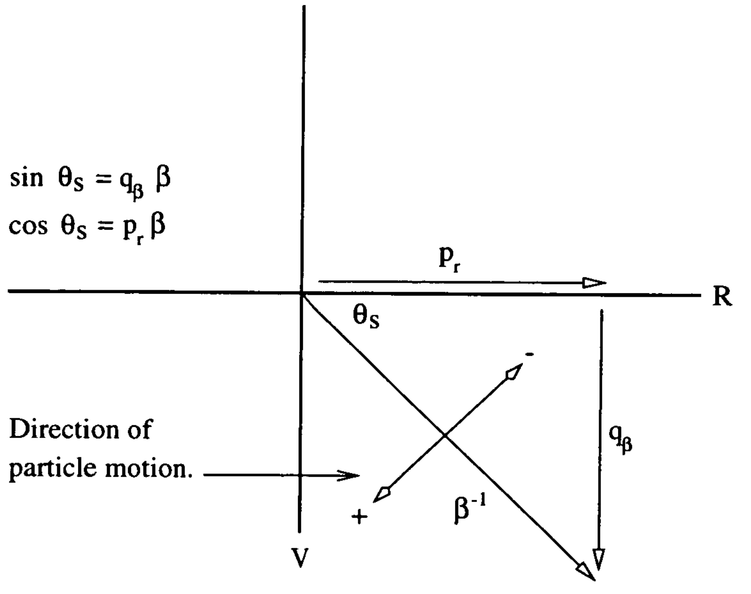

Figure 6.3: SV-wave decomposition to dynamic frame

wave. The sign change occurs as the vertical slowness are of equal magnitude but opposite sign for the material symmetry considered here.

Figure 6.3 shows the corresponding definitions for SV-wave propagation; note the definition of positive SV particle motion the vertical and radial components now have different sign. Now the vertical and horizontal motions in the dynamic frame are

$$v_{D,sv} = S_D \cdot \cos\theta_s, \tag{6.13a}$$

$$v_{D,sr} = -S_D \cdot \sin\theta_s, \tag{6.13b}$$

where S_D and S_U are the complex amplitudes of downgoing and upgoing shear waves in the eigenvector frame respectively and θ_s is the angle to the horizontal. The particle motion is now orthogonal to the direction of propagation Substituting in the sine and cosine definitions yields

$$v_{D,sv} = S_D \cdot p_r \cdot \beta, \tag{6.14a}$$

$$v_{D,sr} = -S_D \cdot q_\beta \cdot \beta. \tag{6.14b}$$

Again for upgoing waves the sign of the vertical slowness only is reversed,

$$v_{U,sv} = S_U \cdot p_r \cdot \beta, \tag{6.15a}$$

$$v_{U,sr} = S_U \cdot q_\beta \cdot \beta. \tag{6.15b}$$

The transfer matrices are made up of the rotations from the eigenvector to dynamic frame for each possible wave type. The structure of the downgoing transfer matrix, in terms of converting wave type to component, is:

$$\boldsymbol{m}_D = \begin{pmatrix} S \to R & P \to R \\ S \to V & P \to V \end{pmatrix}, \tag{6.16}$$

that is, element (1,1) rotates from S to R and so on. Substituting in the decomposition expressions presented above yields:

$$\boldsymbol{m}_D = \begin{pmatrix} -q_\beta \beta & -p_r \alpha \\ p_r \beta & -q_\alpha \alpha \end{pmatrix}, \tag{6.17}$$

for downgoing waves and

$$\boldsymbol{m}_U = \begin{pmatrix} q_\beta \beta & -p_r \alpha \\ p_r \beta & q_\alpha \alpha \end{pmatrix}, \tag{6.18}$$

for upgoing waves.

The data are rotated to the dynamic frame as an initial processing step. They must be rotated to the eigenvector frame. This is done by application of the inverse transfer matrices. The inverses of the transfer matrices are:

$$\boldsymbol{n}_D = \begin{pmatrix} -q_\alpha/B & p/B \\ -p/A & -q_\beta/A \end{pmatrix} = \left[\boldsymbol{m}_U^R\right]^{-1}, \tag{6.19}$$

and

$$\boldsymbol{n}_U = \begin{pmatrix} q_\alpha/B & p/B \\ -p/A & q_\beta/A \end{pmatrix} = \left[\boldsymbol{m}_U^R\right]^{-1}. \tag{6.20}$$

Where

$$A = \beta\left(p^2 + q_\alpha q_\beta\right), \tag{6.21}$$

and

$$B = \alpha\left(p^2 + q_\alpha q_\beta\right). \tag{6.22}$$

Applying these inverse transfer matrices to equation (6.6) yields:

$$U_P = (-p \cdot u_{U,r} + q_\beta \cdot u_{U,v})/B, \tag{6.23a}$$

$$D_P = (-p \cdot u_{D,r} - q_\beta \cdot u_{D,v})/B, \tag{6.23b}$$

$$U_S = (+q_\alpha \cdot u_{U,r} + p \cdot u_{U,v})/A, \tag{6.23c}$$

$$D_S = (-q_\alpha \cdot u_{D,r} + p \cdot u_{D,v})/A. \tag{6.23d}$$

That is, the upgoing and downgoing vertical and radial wavefields have been split into compressional and shear wavefields by rotation from the dynamic frame to the eigenvector frame.

6.4 Recovery of the reflectivity

The ultimate aim of this thesis is to recover the reflectivity of the region beneath the receiver. The upgoing and downgoing wavefields are related to the reflectivity thus:

$$\begin{bmatrix} U_S \\ U_P \end{bmatrix} = \begin{bmatrix} R_{SS} & R_{SP} \\ R_{PS} & R_{PP} \end{bmatrix} \begin{bmatrix} D_S \\ D_P \end{bmatrix}, \tag{6.24}$$

for a single point in (ω, k_x, k_y). This system is under–determined, with two equations and four unknowns. The equations are written explicitly as:

$$U_S = R_{SS} D_S + R_{SP} D_P, \tag{6.25a}$$

$$U_P = R_{PS} D_S + R_{PP} D_P. \tag{6.25b}$$

Using a different source that changes the partition between $P-$ and $S-$ energy in the upgoing and downgoing wavefields yields another set of equations.

$$U'_S = R_{SS} D'_S + R_{SP} D'_P, \tag{6.26a}$$

$$U'_P = R_{PS} D'_S + R_{pp} D'_P. \tag{6.26b}$$

Combining (6.25) and (6.26) and solving for each of the reflectivities yields:

$$R_{PP} = \frac{U_P \cdot D'_S - U'_P \cdot D_S}{D_P \cdot D'_S - D'_P \cdot D_S}, \tag{6.27a}$$

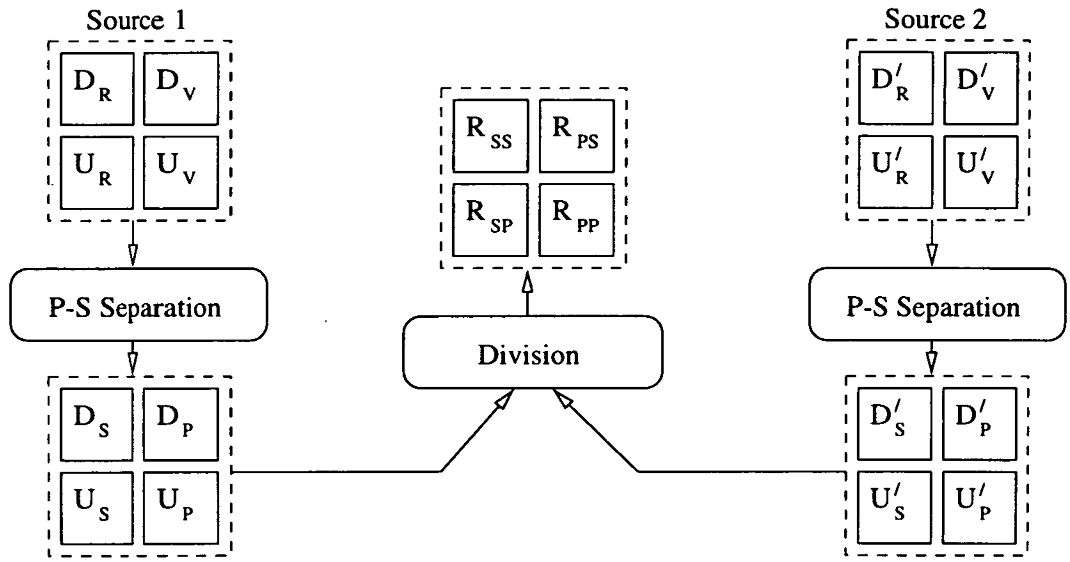

Figure 6.4: Flowchart for the P-S separation and division

$$R_{PS} = \frac{U_P \cdot D'_P - U'_P \cdot D_P}{D'_P \cdot D_S - D_P \cdot D'_S}, \tag{6.27b}$$

$$R_{SP} = \frac{U_S \cdot D'_S - U'_S \cdot D_S}{D_P \cdot D'_S - D'_P \cdot D_S}, \tag{6.27c}$$

$$R_{SS} = \frac{U_S \cdot D'_P - U'_S \cdot D_P}{D'_P \cdot D_S - D_P \cdot D'_S}, \tag{6.27d}$$

for each point in (ω, k_x, k_y). Figure 6.4 is a flow diagram of how the reflectivities are recovered. These reflectivities are broad–band responses. The signal–to–noise ratio varies with frequency. The reflectivities must be filtered in frequency such that they have a bandwidth similar to the original data. How the division is carried out is discussed in the following section.

In the R_{PP} and R_{SS} terms of (6.27) the A and B terms from the inverse transfer matrices cancel completely. In the R_{PS} and R_{SP} terms there are factors of $\frac{B}{A}$ and $\frac{A}{B}$ that do not cancel during the division. Noting

$$\frac{A}{B} = \frac{\beta\,(p^2 + q_\alpha q_\beta)}{\alpha\,(p^2 + q_\alpha q_\beta)} = \frac{\beta}{\alpha}, \tag{6.28}$$

which is constant for all wavenumbers and frequencies, it is never necessary to compute the A or B terms.

6.5 Wavefield division

To solve the recovery equations (6.27) requires division of complex numbers. The denominator is zero at some points in (ω, k_x, k_y). This section discusses how the division is carried out in practice.

Consider two complex numbers P and Q which may take any values. Let

$$R = \frac{P}{Q}. \tag{6.29}$$

Multiplying top and bottom by $Q^\star$, the complex conjugate of Q yields:

$$R = \frac{PQ^\star}{QQ^\star}, \tag{6.30}$$

where the denominator is now always real. The denominator $(QQ^\star)$ can still be zero. Adding a small constant ϵ to the denominator thus,

$$R = \frac{PQ^\star}{QQ^\star + \epsilon}, \tag{6.31}$$

prevents this occurring. This small constant is chosen such that is is some small percentage of the maximum value of $QQ^\star$, typically of the order of 1%. In practice ϵ must be computed before the wavefields are divided. The frequency containing the most energy is the first frequency transformed to the ω, k_x, k_y domain. The quantity $QQ^\star$ is computed for each k_x, k_y point in this domain and ϵ is 0.1% of the maximum $QQ^\star$. This value of ϵ is then used for all data. Incorrect computation leads to errors. If ϵ is too small the result can be dominated by noise, if ϵ is too large then the division can be dominated by ϵ and this yields only a scaled version of the numerator.

Figures 6.5 and 6.6 show the magnitude of two functions $P(x)$ and $Q(x)$ respectively. These functions have similar properties to the functions being divided in the synthetic example of Chapter 8. The value of the stabilisation constant ϵ is 1% of the maximum value of $QQ^\star$. The result from the division $R(x)$ is shown in figure 6.7 The error in the division $E(x)$ can be computed by computing $P(x)$ from the recovered $R(x)$ thus:

$$Q(x)R(x) = P(x), \tag{6.32}$$

and subtracting the computed $P(x)$ from the original:

$$E(x) = Q(x)R(x) - P(x). \tag{6.33}$$

This error is shown in figure 6.8. Figures 6.5, 6.6 and 6.8 are plotted on the same scale, The error is approximately two orders of magnitude less than the numerator or denominator.

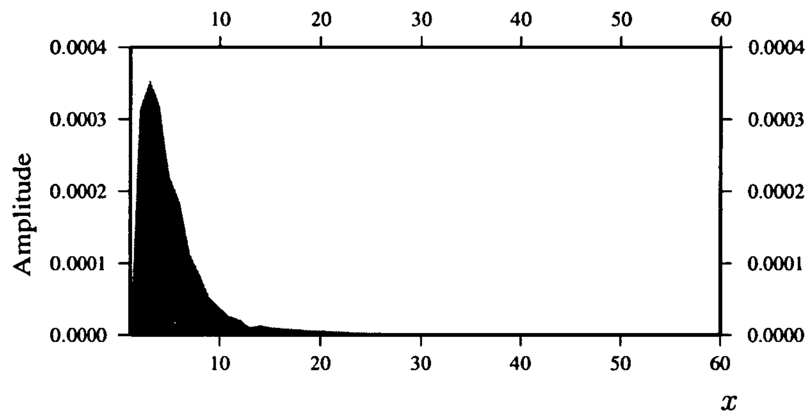

Figure 6.5: Absolute magnitude of $P(x)$

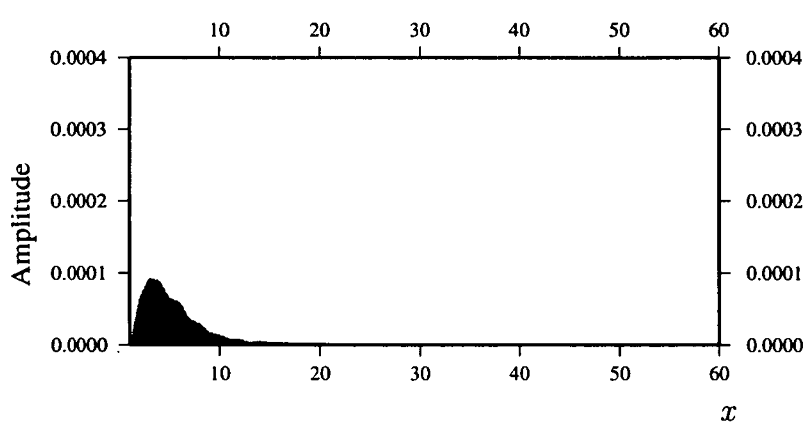

Figure 6.6: Absolute magnitude of $Q(x)$

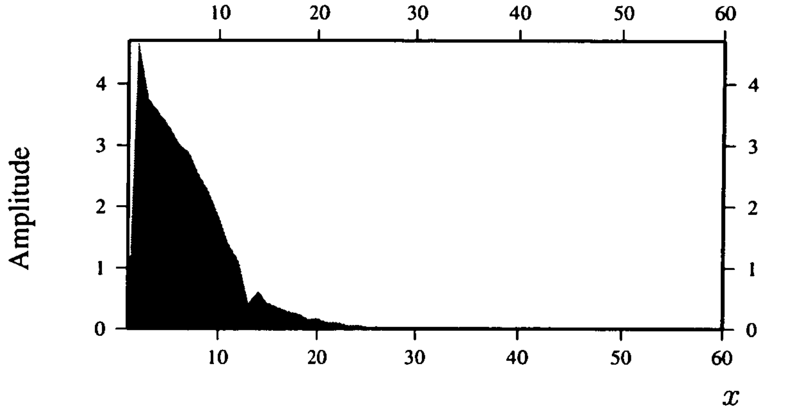

Figure 6.7: Absolute magnitude of $R(x)$, as computed by division

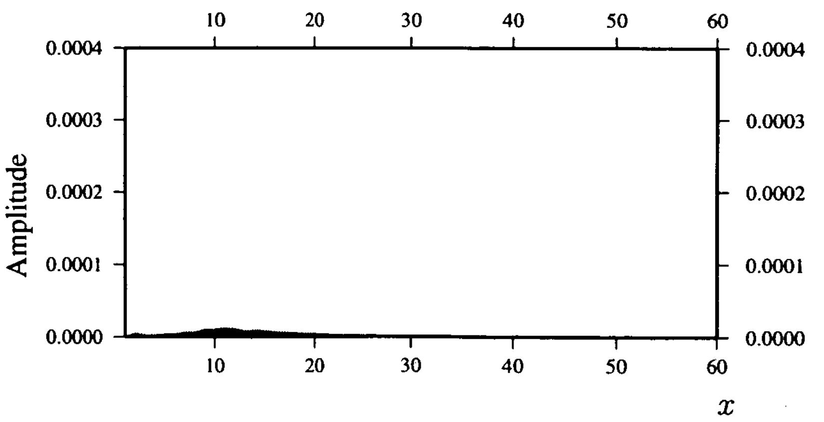

Figure 6.8: Absolute magnitude of $Q(x)R(x) - P(x)$

6.6 The second source

Here the properties that the second source must have are discussed.

Looking again at the term $\beth$, which is:

$$\beth = [\boldsymbol{I} - \boldsymbol{R}_U^{RF}\boldsymbol{R}_D^{RL}]^{-1}\boldsymbol{T}_D^{RS} \times [\boldsymbol{I} - \boldsymbol{R}_U^{SF}\boldsymbol{R}_D^{SL}]^{-1}(\boldsymbol{\Sigma}_D^S - \boldsymbol{R}_U^{SF}\boldsymbol{\Sigma}_U^S). \tag{6.34}$$

The second set of equations must have a different partition of energy between shear and compressional modes. Just changing the source level and not changing the source vector does not achieve this. The term

$$[\boldsymbol{I} - \boldsymbol{R}_U^{RF}\boldsymbol{R}_D^{RL}]^{-1}\boldsymbol{T}_D^{RS} \times [\boldsymbol{I} - \boldsymbol{R}_U^{SF}\boldsymbol{R}_D^{SL}]^{-1} \tag{6.35}$$

does change by changing the source level but does not change the partition of energy between compressional and shear modes. The seismograms with the source at a different level may look radically different but in the (ω, k_x, k_y) domain the second set of equations is just a linear combination of the first. Changing the partition of energy in the source vector,

$$(\boldsymbol{\Sigma}_D^S - \boldsymbol{R}_U^{SF}\boldsymbol{\Sigma}_U^S), \tag{6.36}$$

is the only way of obtaining a second set of equations which is not a linear combination of the first. For marine VSP the source is an acoustic source in the water. Any other source in the water does not have a different partition of energy so the second source must be a sea bed source. For the synthetic data presented here a sea bed source is modelled using a vertical force just beneath the sea bed. The sea bed source can be of any type as long as it is in contact with the solid.

6.7 Reflectivity display

The four recovered reflectivities describe the reflective properties for the region beneath the receiver for each of the possible combinations of wave–mode; R_{PS} describes the P–wave response of the earth to a downgoing S–wave. These reflectivities are not themselves wavefields. This section describes how the reflectivities are converted into wavefields.

The reflectivity response is expressed in a meaningful manner in the time–space domain by (1) recovering the reflectivity response, (2) generating wavefields in the frequency–wavenumber domain from this response and (3) transforming the wavefields to the time–space domain.

Given V_P and V_S the compressional wave and shear wave vertical wavenumbers, $k_{z,P}$ and

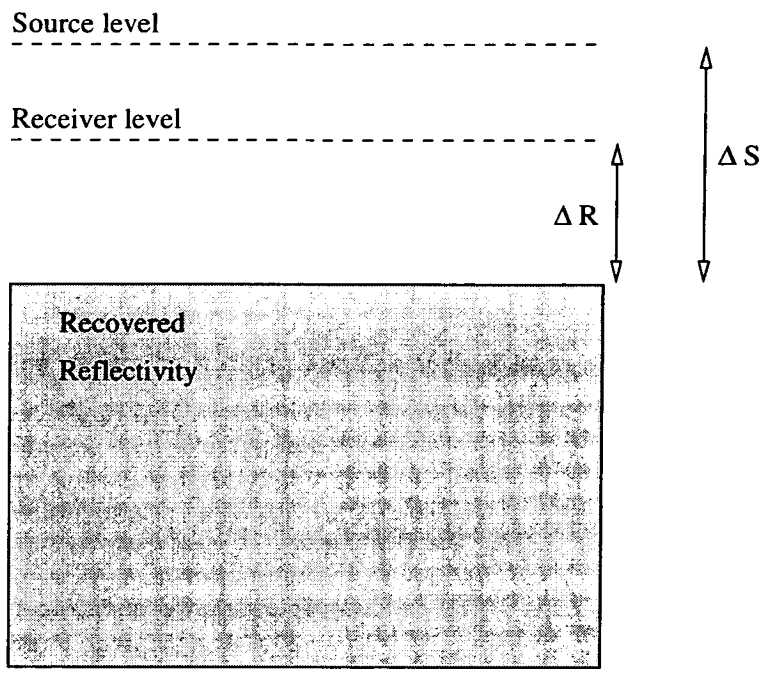

Figure 6.9: Geometry for computing wavefields from the recovered reflectivities

$k_{z,S}$ respectively, can be computed. Four wavefields are calculated. These are: W_{PP}, W_{PS}, W_{SP} and W_{SS}, corresponding to their respective reflectivities. They are:

(1) downgoing P, upgoing P

$$W_{PP} = \exp\{ik_{z,P}\Delta R\} \cdot R_{PP} \cdot \frac{i}{2k_z, P} \cdot \exp\{ik_{z,P}\Delta S\} \cdot S(\omega), \tag{6.37a}$$

(2) downgoing S, upgoing P

$$W_{PS} = \exp\{ik_{z,P}\Delta R\} \cdot R_{PS} \cdot \frac{i}{2k_z, S} \cdot \exp\{ik_{z,s}\Delta S\} \cdot S(\omega), \tag{6.37b}$$

(3) downgoing P, upgoing S

$$W_{SP} = \exp\{ik_{z,S}\Delta R\} \cdot R_{SP} \cdot \frac{i}{2k_z, P} \cdot \exp\{ik_{z,P}\Delta S\} \cdot S(\omega), \tag{6.37c}$$

(4) downgoing S, upgoing S

$$W_{SS} = \exp\{ik_{z,S}\Delta R\} \cdot R_{SS} \cdot \frac{i}{2k_z, S} \cdot \exp\{ik_{z,S}\Delta S\} \cdot S(\omega). \tag{6.37d}$$

Figure 6.9 shows the geometry. Each reflectivity is multiplied by an incident field. The incident field for a shear–wave is:

$$\frac{i}{2k_z, S} \exp\{ik_{z,S}\Delta S\} \cdot S(\omega). \tag{6.38}$$

The source term $S(\omega)$ has the same bandwidth as the original source. The vertical distance from the source to the reflecting zone is ΔS. The wavefield is a response to a spherically symmetric source decomposed into plane waves, thus the reflectivity is multiplied by a factor of $\frac{i}{2k_z}$ (equation (2.46)). The plane wave components are then propagated to the receiver level by $\exp\{ik_{z,P|S}\Delta R\}$, where ΔR is the vertical distance from the reflecting region to the receiver level. The vertical wavenumbers $k_{z,P}$ and $k_{z,S}$ can be zero, thus the spherical wavefield correction terms have a pole at $k_z = 0$. To prevent division by zero, complex frequency is used; this concept is detailed in the following chapter. These wavefields have the same bandwidth as the original wavefields.

6.8 Processing summary

The mechanics of the transform from time–space to frequency–wavenumber domain are detailed in the next chapter. The following pseudo-code shows the processing as it is done in the (ω, k_x, k_y) domain.

```
calculate the stabilisation constant for the division.

 .
foreach frequency
    foreach point in k_x,k_y
        compute radial wavenumber and radial slowness
        compute P and S material vertical wavenumbers
                                        and slownesses
        .
        P - S separation
        .
        compute reflectivities by division
        .
        compute P and S model vertical wavenumbers
        convert reflectivities to wavefields
    done
done
```

6.9 Discussion and conclusions

The equations for recovering the reflectivity beneath the receiver have been presented. It is impossible to recover the reflectivity using data from only a single source. A second source must be used, and that source must change the partition of energy between compressional and shear propagating waves for each wavenumber. For marine walkaway VSP if one source is an acoustic explosion the other must be a sea-bed source. Such sea–bed sources are currently being developed.

The recovery scheme depends on knowing the compressional and shear velocities of the medium local to the receiver. These velocities are measured when the well is logged. The wavefields are decomposed into compressional and shear parts. The recovery scheme depends on combining these wavefields and dividing one combination of wavefields by another. A method for making this division stable has been presented.

THE (x, y, t) TO (k_x, k_y, ω) TRANSFORM

Chapter 7

7.1 Introduction

The equations for the three–dimensional Fourier transform of the wavefield have been presented. Here I show how these are implemented in practice and what symmetries should be observed at each stage of the transform. These symmetries are shown as they are a useful check as to whether the transform and processing schemes are valid. Examples from the standard modelled wavefield are shown at each stage. A complete discussion of the Fourier transform is found in Chapter 2 of Bracewell (1986). The Hankel transform is not used as this involves asymptotic forms of Bessel functions and nonlinear spatial interpolation. Using Fourier transforms also allows for easy adaptation of the transform for three–dimensional geometries. Although this scheme appears computationally expensive, it is highly suitable for implementations on parallel computers. The synthetic data examples presented are plotted as they are stored to show clearly how the transform is carried out in practice. The earth is assumed to be laterally invariant. Thus a horizontal array of sources and a single receiver is equivalent to single source and a horizontal array of receivers.

7.2 Aliasing

The data are recorded with a finite spatial sampling interval and a finite time sampling interval. The number of spatial samples is much less than the number of time samples thus aliasing is most likely due to under sampling in space. Consider a shear wave travelling with velocity V_s in the receiver layer, the smallest unaliased wavelength λ_A is twice the spatial sampling interval $2\delta x$. The wave velocity is related to the wavelength and frequency by:

$$V_s = \lambda_A \cdot f_A, \tag{7.1}$$

where f_A is the largest unaliased frequency. Assuming V_s = 1950m/s then f_A, for a 25m spatial sample rate, is:

$$f_A = \frac{V_s}{2\delta x} = \frac{1950\text{ms}^{-1}}{2 \cdot 25\text{m}} = 39\text{Hz}, \tag{7.2}$$

an angular frequency ω of $245s^{-1}$. To prevent spatial aliasing, a Gaussian filter is convolved with the data in time to suppress frequencies above f_A. This convolution increases the length of the data in the time direction. A single trace before and after anti-alias filtering is shown in figure 7.1. A 25m spatial sample spacing is realistic for marine walkaway VSP, finer sampling

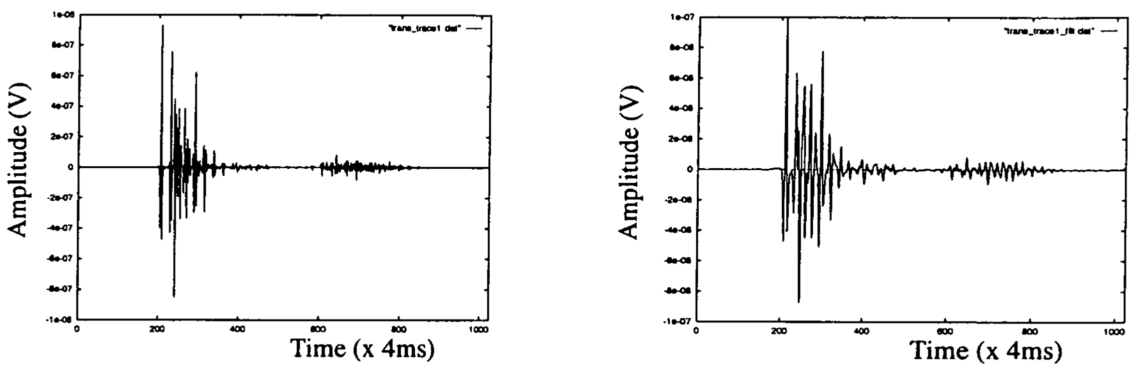

Figure 7.1: A) Original trace 1 B) Band–pass filtered trace 1

would allow for higher frequencies to be used. There is a useful amount of information propagating above the largest unaliased frequency. Under sampling in space forces useful data to be thrown away.

7.3 Transforming from time-space to frequency–space

Here the equations of Fourier transform from time to frequency are shown. This involves using complex values for the frequency. The infinite, continuous time t to frequency ω transform is

$$A(x, \omega) = \int_{-\infty}^{\infty} a(x, t) \exp\{i\omega t\}\, dt. \tag{7.3}$$

The periodic, discrete Fourier transform may be written as:

$$A(x, \omega) = \Delta t \sum_{j=0}^{N-1} a(x, j\Delta t) \exp\{i\omega j \Delta t\}, \quad \text{where, } \Delta t = \frac{T}{N}, \tag{7.4}$$

where $\omega = \frac{2\pi m}{T}$; N is the number of samples per trace and T is the trace length. This periodic form is cyclically symmetric in N. The wavefield is causal in time. Causality is assured by padding the data with zeros to twice its original length (after anti–alias filtering) in time. There is a DC bias in the data, which must be removed before transformation. The trace average is subtracted from each sample in a trace, on a trace–by–trace basis. This DC bias is the zeroth frequency in the transform domain, and should be zero as there can be no energy propagating at zero frequency.

During processing in the (w, k_y, k_x) domain it is necessary to divide by quantities which tend to zero as w tends to zero. The data are shifted away from the real w axis by a small constant α. This then prevents such division by zero. The new frequency ω' is complex and is defined:

$$\omega' = \omega + i\alpha. \tag{7.5}$$

Consider a function $f(t)$. The Fourier transform from t to ω is

$$F(\omega) = \int_{-\infty}^{\infty} f(t) \exp\{i\omega t\}\ dt, \tag{7.6}$$

substituting ω' for ω yields:

$$F(\omega') = \int_{-\infty}^{\infty} f(t) \exp\{i(\omega + i\alpha)t\}\ dt, \tag{7.7}$$

which is

$$F(\omega') = \int_{-\infty}^{\infty} f(t) \exp\{-\alpha t\} \exp\{i\omega t\}\ dt. \tag{7.8}$$

Thus shifting the data along the imaginary axis in the frequency domain by a constant α is equivalent to applying an exponentially decaying ramp to the data in the time domain thus:

$$f'(t) = f(t) \exp\{-\alpha t\}, \tag{7.9}$$

where $f'(t)$ is the data after the application of the ramp. The ramp decay parameter α is chosen such that $\exp\{-\alpha t\}$ is 0.1 halfway through the trace. After the inverse transform the data are recovered by:

$$f(t) = f'(t) \exp\{+\alpha t\}. \tag{7.10}$$

The ramp is applied to all traces immediately before time to frequency transform. The discrete Fourier transform is computed as normal. Whenever the frequency w is computed it is now complex with fixed imaginary part α.

Figure 7.2 shows a cartoon of the discrete Fourier transform (DFT) of a real causal function, such as a time trace. The variable τ is discrete time, the original pulse length is $t/2$ and it has been padded with zeros to $\tau = t$. As the transform is over a finite interval, the function must be periodic in t. After the DFT the real part is symmetric about $\nu = 0$ where ν is a discrete frequency variable. The frequencies are in the range $\nu = 0$ to $\nu = 2f_N$, where f_N is the Nyquist frequency. Again the transformed data are periodic in $2f_N$ noting that positive frequencies above the Nyquist are equivalent to negative frequencies. The data must also tend

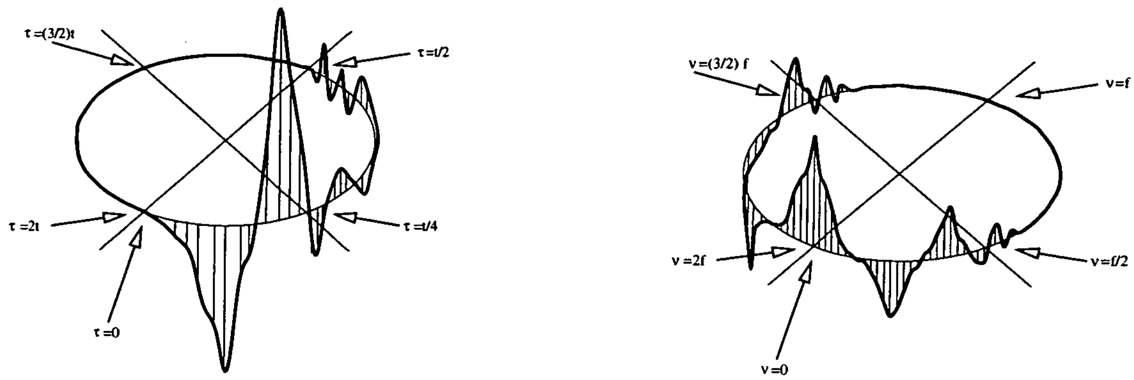

Figure 7.2: Cartoon showing a)A real time trace b)The real part of the DFT of a) after (Bracewell, 1986),p363

to zero as t tends to infinity, otherwise there will be a step containing infinite frequencies at the end of the data, introducing edge effects in the transform. The wavefield naturally decays with time, as can be seen clearly in figure 7.1.

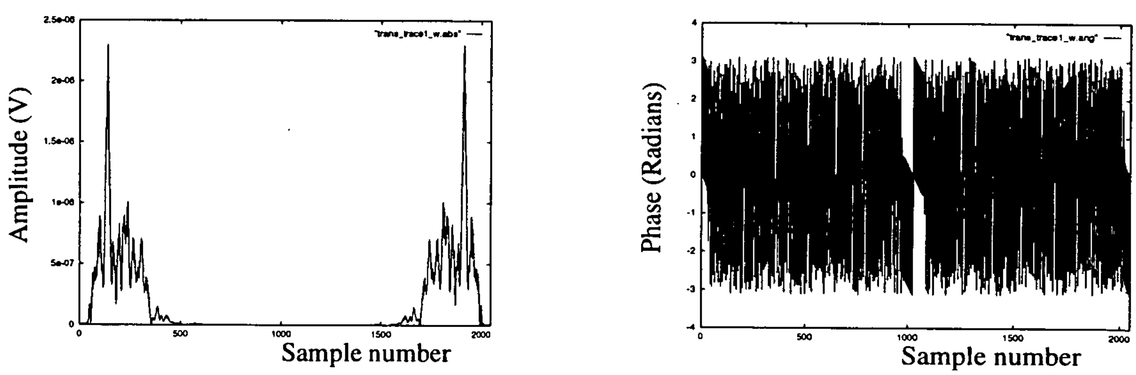

Figure 7.3: A) Amplitude trace 1 B) Phase trace 1 (spectra are wrapped about twice the Nyquist frequency)

Figure 7.3 shows the amplitude and phase spectra of a single transformed trace as it is output from the DFT. Note the negative frequencies are in the latter half of the data. The phase spectrum is odd, the amplitude spectrum is even. This occurs as the data has the property of *conjugate symmetry* in the (x, y, ω) domain. Consider the Fourier transform of $A(x, -\omega)$:

$$A(x, -\omega) = \int_{-\infty}^{\infty} a(x, t) \exp\{-i\omega t\} \, dt. \tag{7.11}$$

Taking the complex conjugate of the Fourier transform of $A(x, \omega)$ is:

$$A^\star(x, -\omega) = \int_{-\infty}^{\infty} a^\star(x, t) \exp\{i\omega t\}\, \mathrm{d}t. \tag{7.12}$$

As $a(x, t)$ is purely real $a^\star = a$ so

$$A^\star(x, -\omega) = A(x, \omega). \tag{7.13}$$

That is, in the transform domain the value of the negative frequencies of a function is the complex conjugate of the equivalent positive frequency. This property is shown by functions which are purely real in the original domain.

7.4 The space to wavenumber transform

The data are now processed on a frequency–by–frequency basis. The data–slice in the (x, y)–plane has the symmetry condition that the data are cylindrically symmetric about the origin in the plane, and ω is fixed for each slice.

The distance of each $x - y$ point on a grid from the origin may be calculated and a value for this point is interpolated from the $y = 0$ data using cubic spline interpolation. The interpolated data have the following properties.

$$A(-x, -y, \omega) = A(+x, +y, \omega), \tag{7.14a}$$
$$A(-x, +y, \omega) = A(+x, +y, \omega), \tag{7.14b}$$
$$A(+x, -y, \omega) = A(+x, +y, \omega). \tag{7.14c}$$

For fixed frequencies ω the wavefield is cylindrically symmetric about the origin for both real and imaginary parts. So for a fixed x **or** y **and** ω A is even for both real and imaginary parts. Figure 7.4 shows a data slice for fixed ω. The origin in the (x, y)–plane is the lower left corner of the data, $(1, 1)$ in the grid coordinates. The data are wrapped about twice the maximum x and y. The cylindrical symmetry in amplitude and phase is clearly evident.

Consider $A(x, y, \omega)$; two orthogonal transforms are applied in x and y.

$$\tilde{A}_x(k_x, y, \omega) = \int_{-\infty}^{\infty} A(x, y, \omega) \exp\{-ik_x x\}\ \mathrm{d}x, \tag{7.15}$$

followed by

$$\hat{A}_{xy}(k_x, k_y, \omega) = \int_{-\infty}^{\infty} \tilde{A}_x(k_x, y, \omega) \exp\{-ik_y y\}\ \mathrm{d}y. \tag{7.16}$$

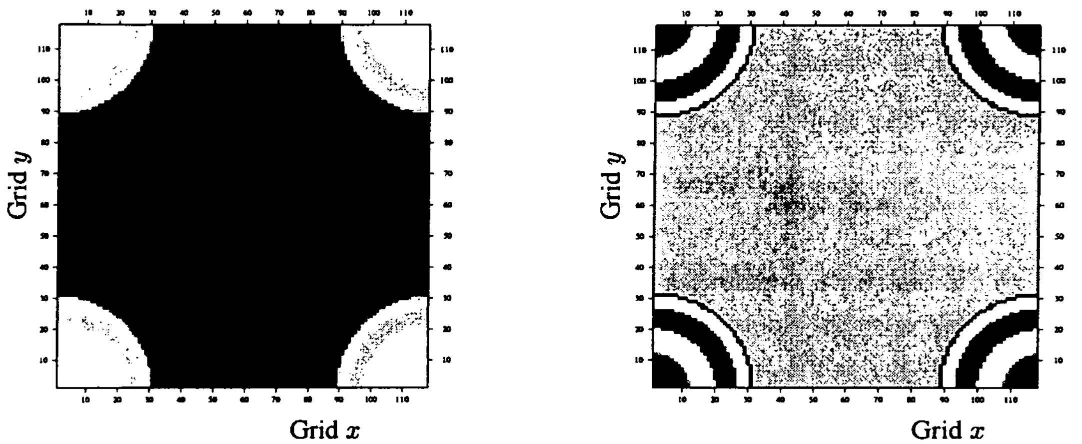

Figure 7.4: A) Amplitude spectra in (x, y)-plane B) Phase spectra in (x, y)-plane, for a fixed frequency

The discrete from of the spatial transform is

$$\tilde{A}_x(k_x, \omega) = \Delta x \sum_{j=0}^{N-1} A(j\Delta x, \omega) \exp\{ik_x j\Delta x\}, \quad \text{where} \quad \Delta x = \frac{X}{M}, \tag{7.17}$$

where $k_x = \frac{2\pi m}{M}$; X is the trace length in space and M is the number of geophones. As $A(x, y, \omega)$ is even for fixed ω then $\hat{A}(k_x, k_y, \omega)$ is also even for fixed ω. That is conjugate symmetry is not observed in the (x, y) or (k_x, k_y)–planes (at constant ω). Figure 7.5 shows the two–dimensional transform of the data slice shown in figure 7.4. Again, the transformed data are cylindrically symmetric about the origin and the data are wrapped around twice the Nyquist wavenumbers.

The wavefield should also decay to zero as x tends to infinity. If this is not the case then edge effects appear in the transformed domain. Applying a filter to taper the data affects the amplitude and phase of the wavefield in the wavenumber domain. The wavenumbers must be preserved as the true wavenumbers are required for the division in (ω, k_x, k_y). Thus edge effects are introduced into the results.

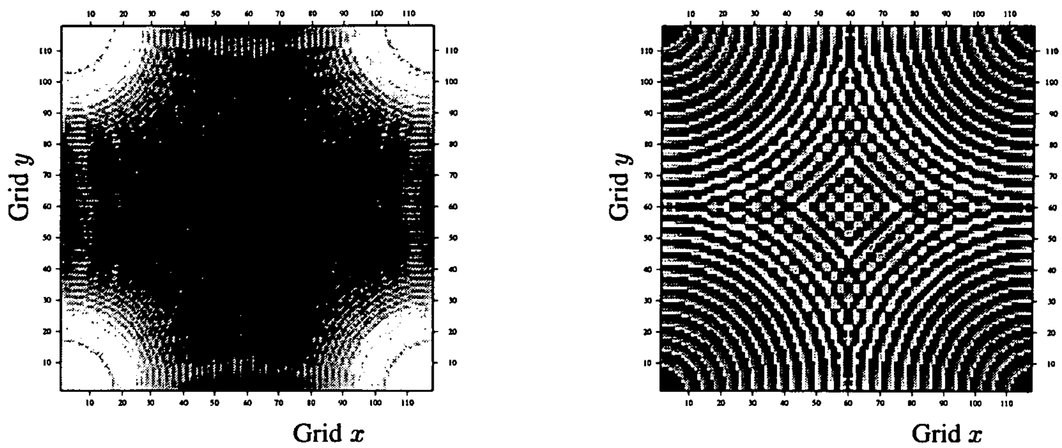

Figure 7.5: A) Amplitude spectra in (k_x, k_y)-plane B) Phase spectra in (k_x, k_y)-plane, for a fixed frequency

7.5 The (ω, k_x, k_y) domain

Combining the three transforms the three–dimensional transform is:

$$\hat{A}(k_x, k_y, \omega) = \iiint_{-\infty}^{\infty} a(x, y, t) \exp\{i(\omega t - k_x x - k_y y)\} \; dt \; dx \; dy. \tag{7.18}$$

The transformed volume is cylindrically symmetric about $\omega = 0$. The radial wavenumber k_r is the square–rot of the sum of the squares of the orthogonal horizontal wavenumbers. That is

$$k_r = (k_x^2 + k_y^2)^{\frac{1}{2}}. \tag{7.19}$$

As the data are symmetric there is no difference between positive and negative frequencies. Figure 7.6 shows the amplitude spectra for two wavefields. The vertical axis is angular frequency and the horizontal axis radial wavenumber[1]. The P–wavefield has more energy propagating at low horizontal wavenumber than the S–wavefield. That is, the P–waves are propagating closer to vertical the the S–waves, as one might expect. During processing the amplitudes of all wavefields are set to zero for $k_r = 0$ and $\omega = 0$. They should also be zero at the Nyquist frequency.

[1]These data come from $k_y = 0$ thus, $k_r = k_x$.

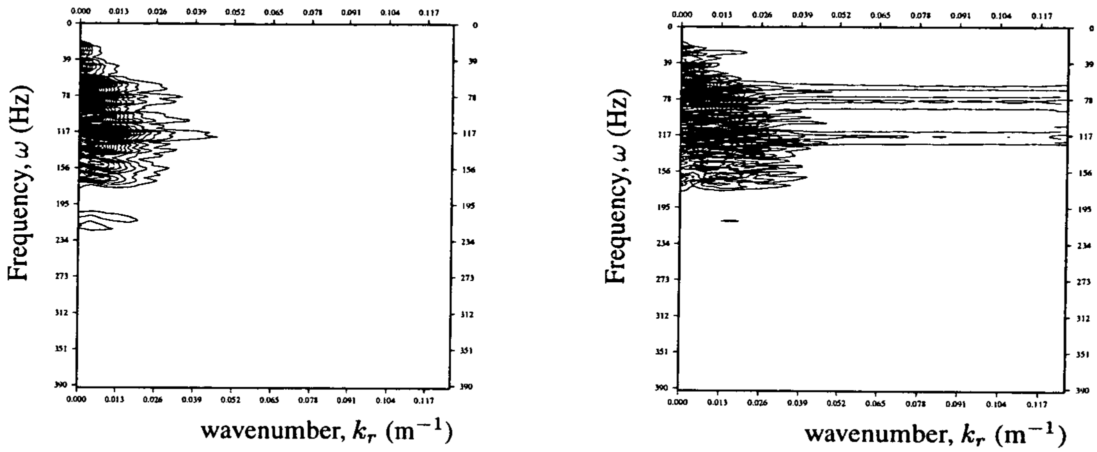

Figure 7.6: A) Upgoing $P-$ amplitude spectra in (k_x, k_y)-plane, B) Upgoing $S-$ amplitude spectra in (k_x, k_y)-plane

7.6 The inverse transform

The radial-wavenumber–space transform is simply the inverse of the forward transform thus:

$$A(x, y, \omega) = \frac{1}{4\pi^2} \iint_{-\infty}^{\infty} \hat{A}(k_x, k_y, \omega) \exp\{i(k_x x + k_y y)\} \; \mathrm{d}k_x \; \mathrm{d}k_y. \tag{7.20}$$

This is carried out using the inverses of the forward transforms. For speed one does not have to compute the negative frequency part of the wavefield as this can be constructed from the positive parts using complex conjugate symmetry. The frequency to time transform is the inverse of the time to frequency transform.

7.7 Transform summary

The mechanics of the processing in the frequency–wavenumber domain were dealt with in the previous chapter. The following pseudo-code shows the transform as it is carried out in practice.

```
calculate the alias frequency.
compute anti-alias filter

foreach (time) trace
    apply anti alias filter
    remove DC
```

```
    pad to twice original length with zeros
    apply exponentially decaying ramp
    transform from time to frequency
done
.
foreach positive frequency
    pad data to twice original length in x
    interpolate data onto x-y grid
    wrap grid around maximum x and y
    transform from x to k_x
    transform from y to k_y
    .
    +++++++++++++++++++++++++
    Data are now in k_x,k_y,w
    +++++++++++++++++++++++++
    .
    inverse transform from k_x to x
    inverse transform from k_y to y
done
.
for each (frequency) trace
    compute negative frequencies using complex conjugate symmetry
    inverse transform from frequency to time
    apply exponentially increasing ramp
done
.
```

7.8 Conclusions

The transform from the space–time to wavenumber–frequency and its inverse have been presented. There are three pre–transform processing steps which must be carried out. These are:

- Remove DC bias
- Anti–alias filtering. (Aliased energy in (ω, k_x, k_y) will introduce errors in the processing if it is not removed.)
- Application of exponentially decaying ramp to make the frequency complex.

Only the positive frequencies are processed. Negative frequencies are computed from the positive frequencies using the property of complex conjugate symmetry.

RECOVERING THE REFLECTIVITY: APPLICATION TO SYNTHETICS

Chapter 8

On two occasions I have been asked [by members of Parliament], 'Pray, Mr. Babbage, if you put into the machine wrong figures, will the right answers come out?' I am not able rightly to apprehend the kind of confusion of ideas that could provoke such a question.

Charles Babbage

8.1 Introduction

In this chapter the theory of reflectivity recovery is applied to synthetic data. Two models are used, one with a single reflector beneath the receiver level and the second with many reflectors beneath the receiver level. Three types of sea–bed source are used, an explosion and two tractions. Seismograms are shown at each stage of the process. This work has been presented as Higgins *et al.* (1998).

8.2 The (synthetic) data

Table 8.1 shows the earth model used to generate the synthetic data. The shot spacing is 25m and there are 60 shots ranging in offset from 0m to 1500m. The single receiver is placed at 850m depth, just above the first buried interface. This model is shown in Figure 8.1 and Table 8.1. The synthetic seismograms are generated using ANISEIS (Taylor, 1992), a full–waveform reflectivity modelling package. The upgoing and downgoing wavefields are modelled separately for each source, so no upgoing–wavefield downgoing–wavefield separation is required. Three sources are used: two orthogonal tractions corresponding to a vertical force and a horizontal force parallel to the source (and therefore receiver) array and an acoustic explosion. The horizontal force referred to here is one which aligned in the radial direction for each shot point.

Combinations of these sources simulate dual source experiments, with the source at the sea–

Layer	V_p (m/s)	V_s (m/s)	ρ (g/cm^3)	Thickness (m)
1	1500	0	1	100
2	1900	1300	2.1	500
3	2300	1600	2.4	500
4	2800	1900	2.6	∞

Table 8.1: Simple earth model

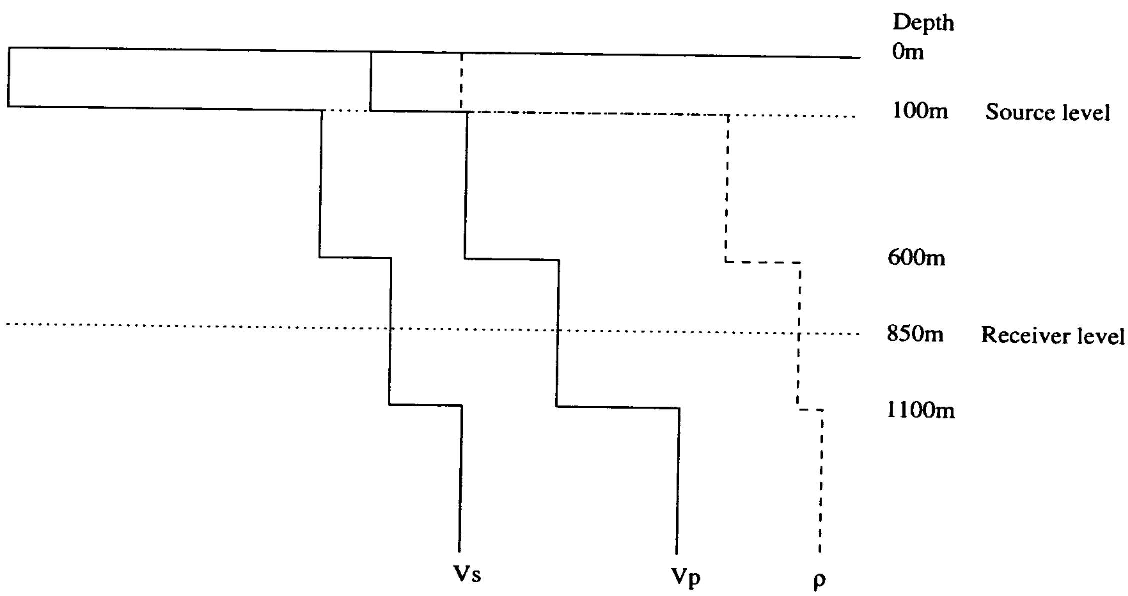

Figure 8.1: Simple earth model

bed. There are three possible dual–source experiments: explosion and vertical-force, explosion and horizontal-force and horizontal-force and vertical-force. The acoustic data are shown in figure 8.2, the vertical force data in 8.3, and the horizontal force data in figure 8.4. Each set of upgoing or downgoing wavefields is plotted on the same scale. The upgoing wavefields are plotted at an order of magnitude greater scale than the corresponding downgoing wavefields. The vertical and radial geophone components are shown. There is no out of plane propagation and so no energy in the transverse direction.

Note that the near–offset traces of the vertical–force and acoustic source are very similar for both the upgoing and downgoing wavefields. Note that the P–waves and S–waves overlap in time in parts of the upgoing wavefields.

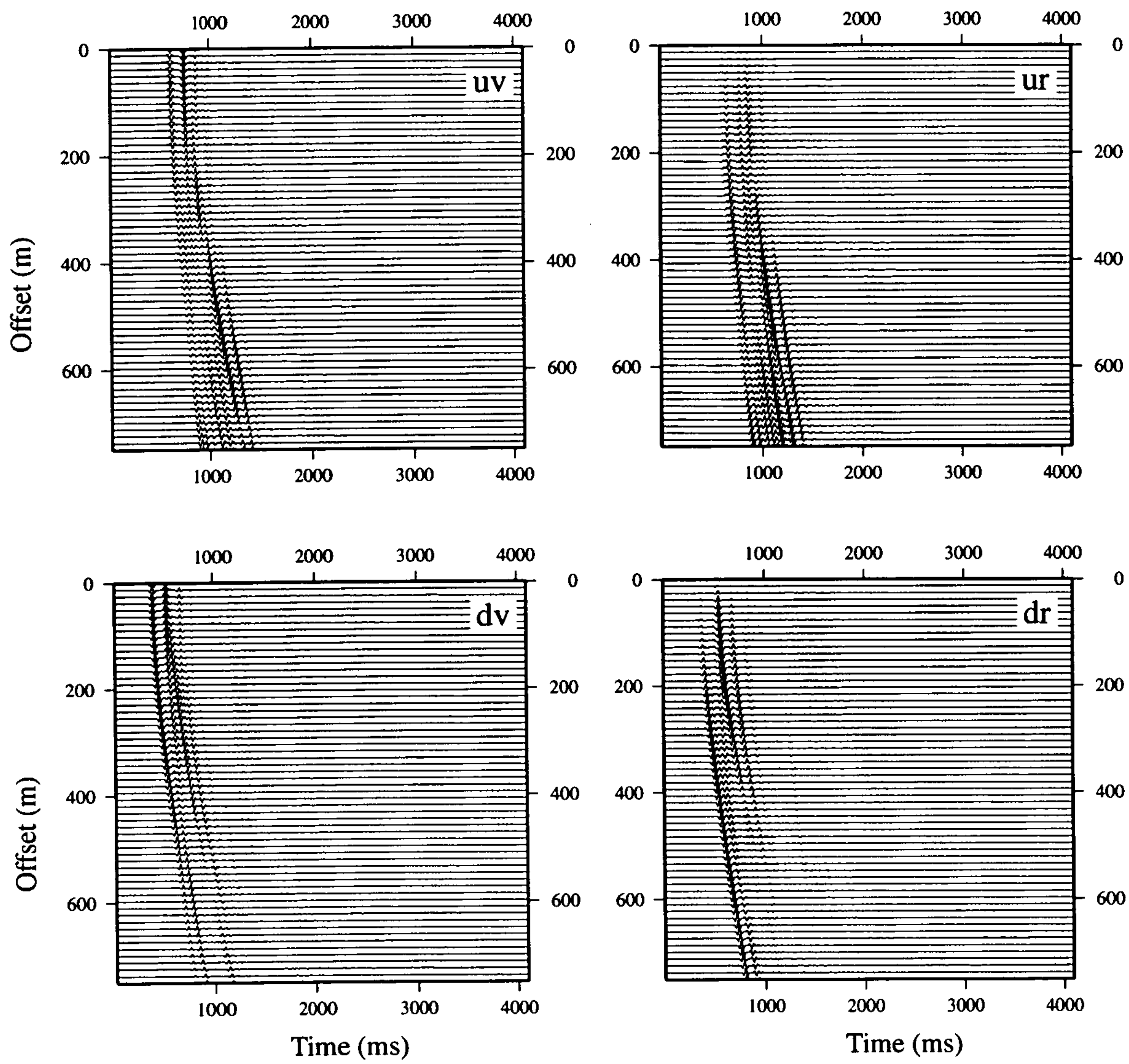

Figure 8.2: Acoustic source data, vertical and radial components

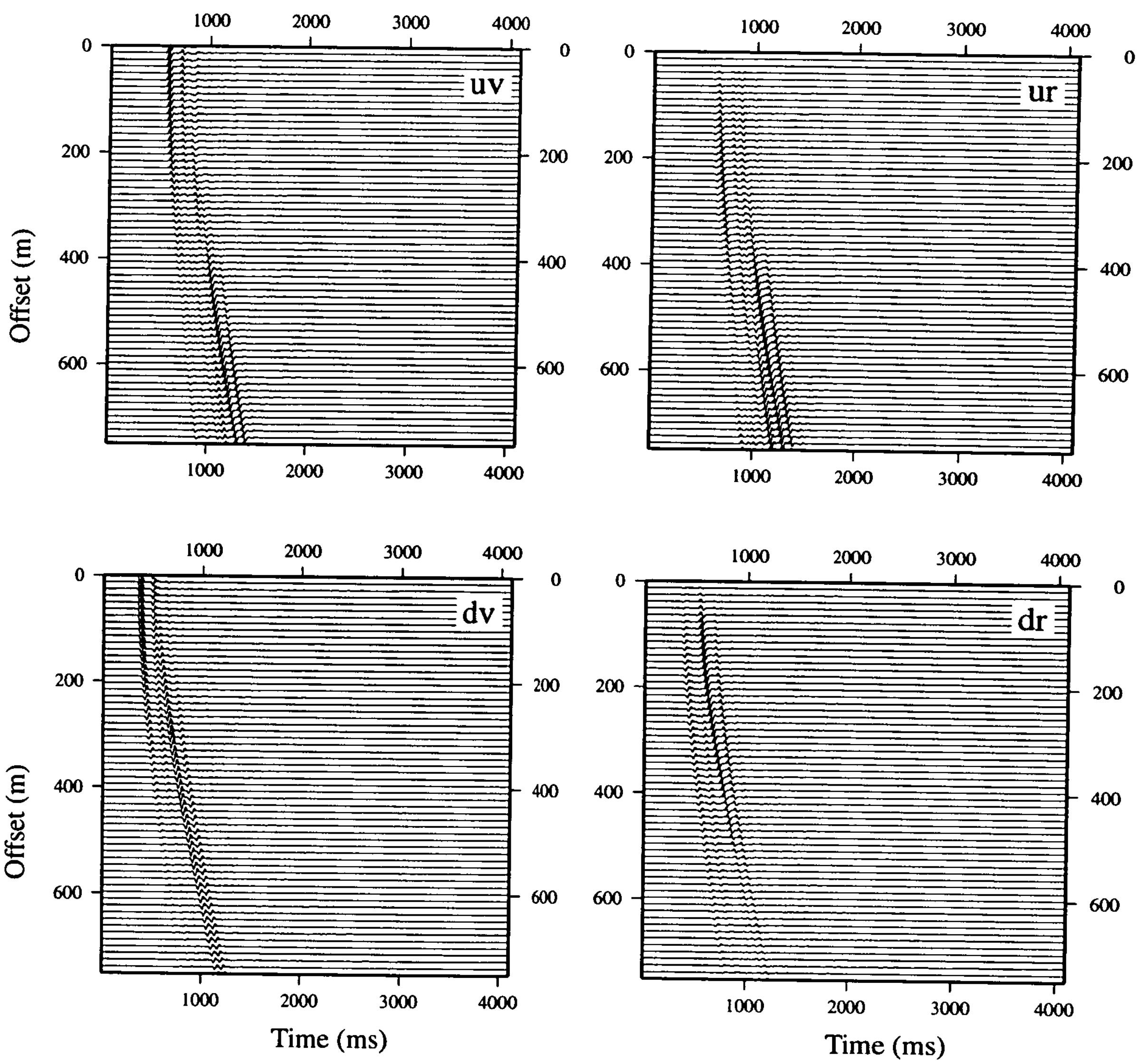

Figure 8.3: Vertical force source data,vertical and radial components

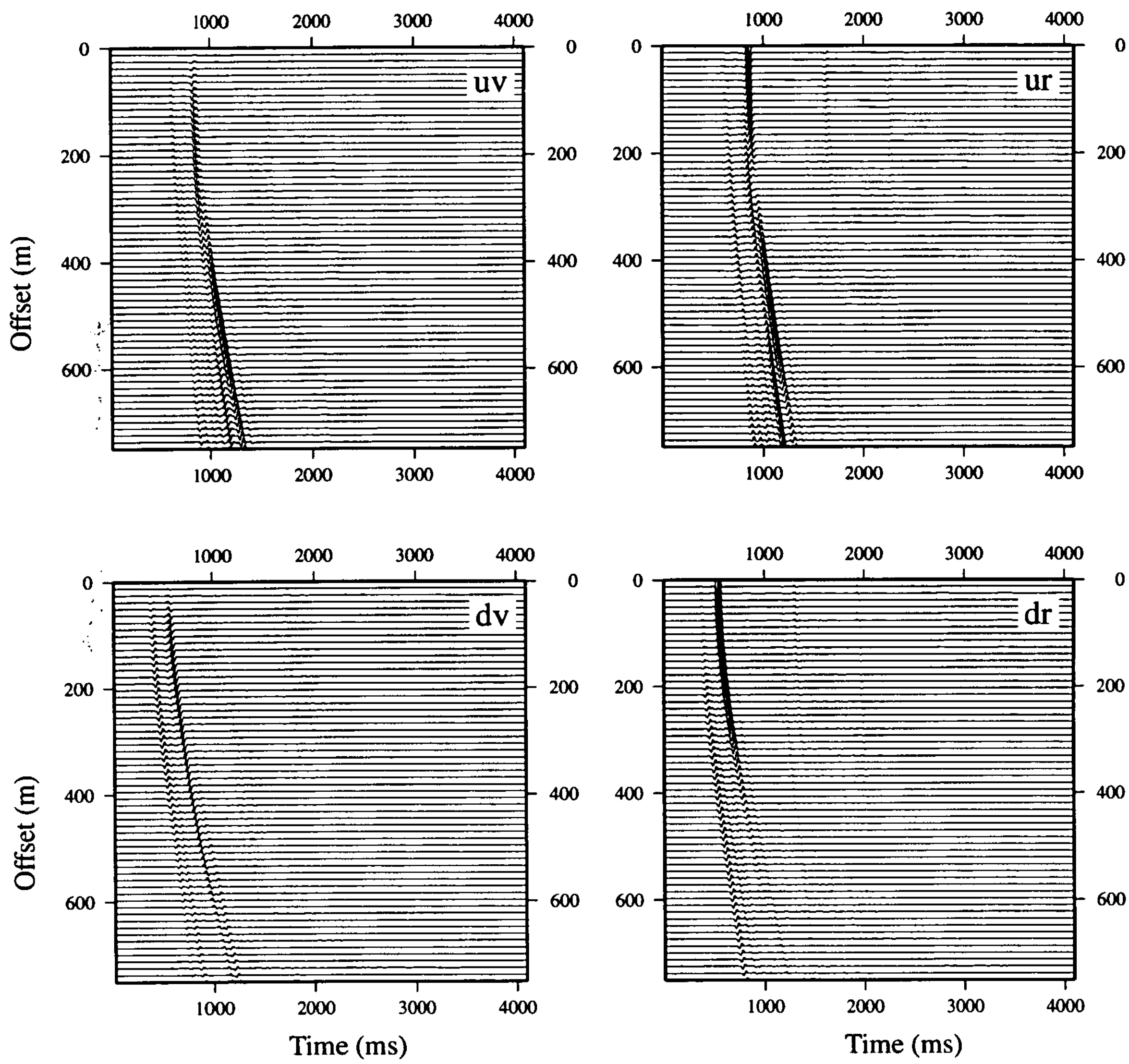

Figure 8.4: Horizontal force source data,vertical and radial components

8.3 P and S separation

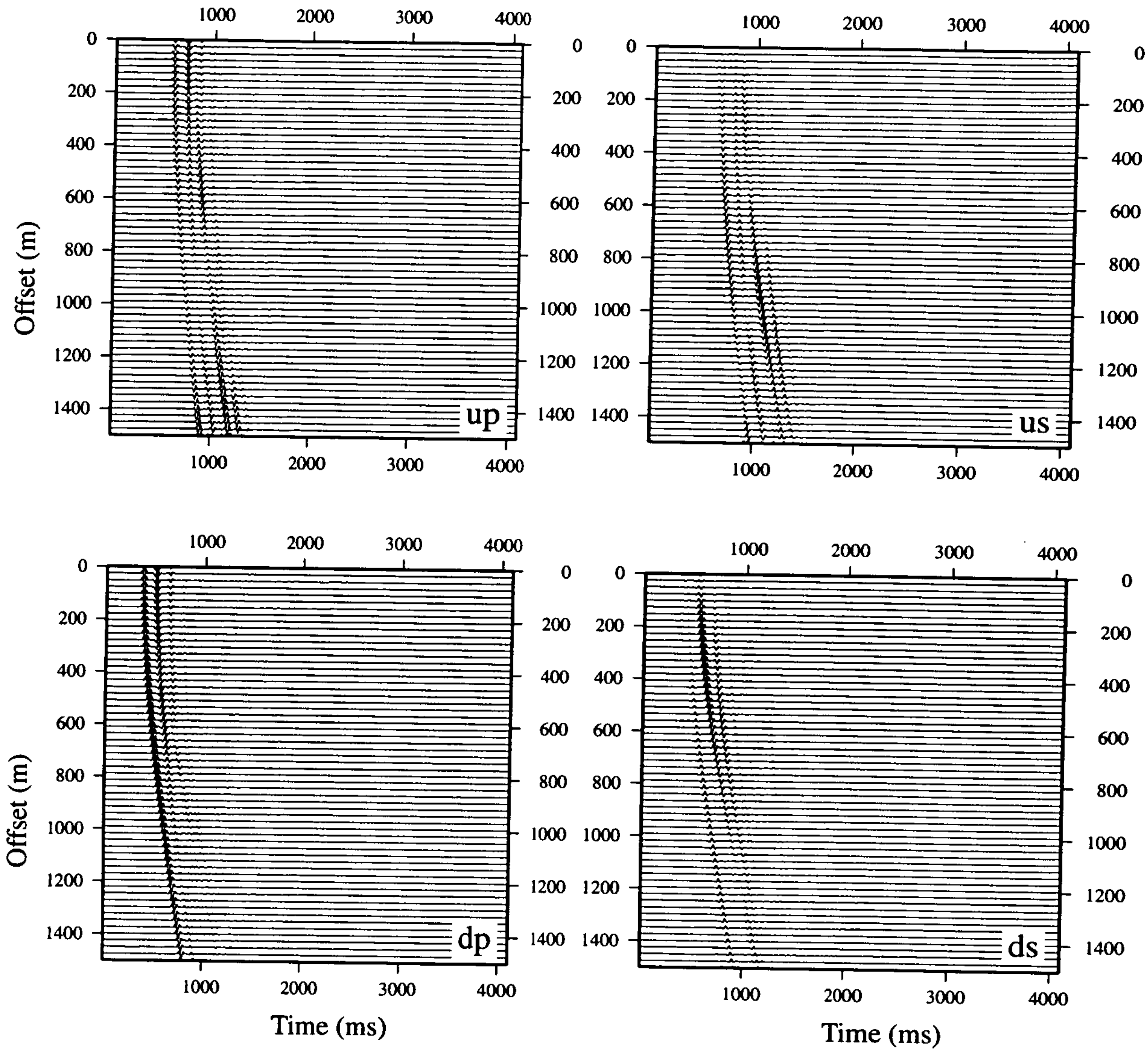

Figure 8.5: Acoustic source data, $P-$ and $S-$ components

The post P–S separation wavefields are shown in figures 8.5, 8.6 and 8.7. The upgoing wavefield is plotted at an order of magnitude greater scale.

The P-S separation is dependent on the estimate of the P and S velocities at the receiver. Dankbaar (1987) notes that for a standard marine VSP velocity variations along the borehole of up to 25% yield acceptable results for his (similar) separation scheme. For this case there is no variation of velocity at each receiver position as the earth is assumed to be laterally invariant. Accurate velocities are available from the borehole logs and any near–offset or zero–offset experiments so velocity estimation should pose little problem.

The separation works well, even when the P–waves and S–waves overlap in time. Again the

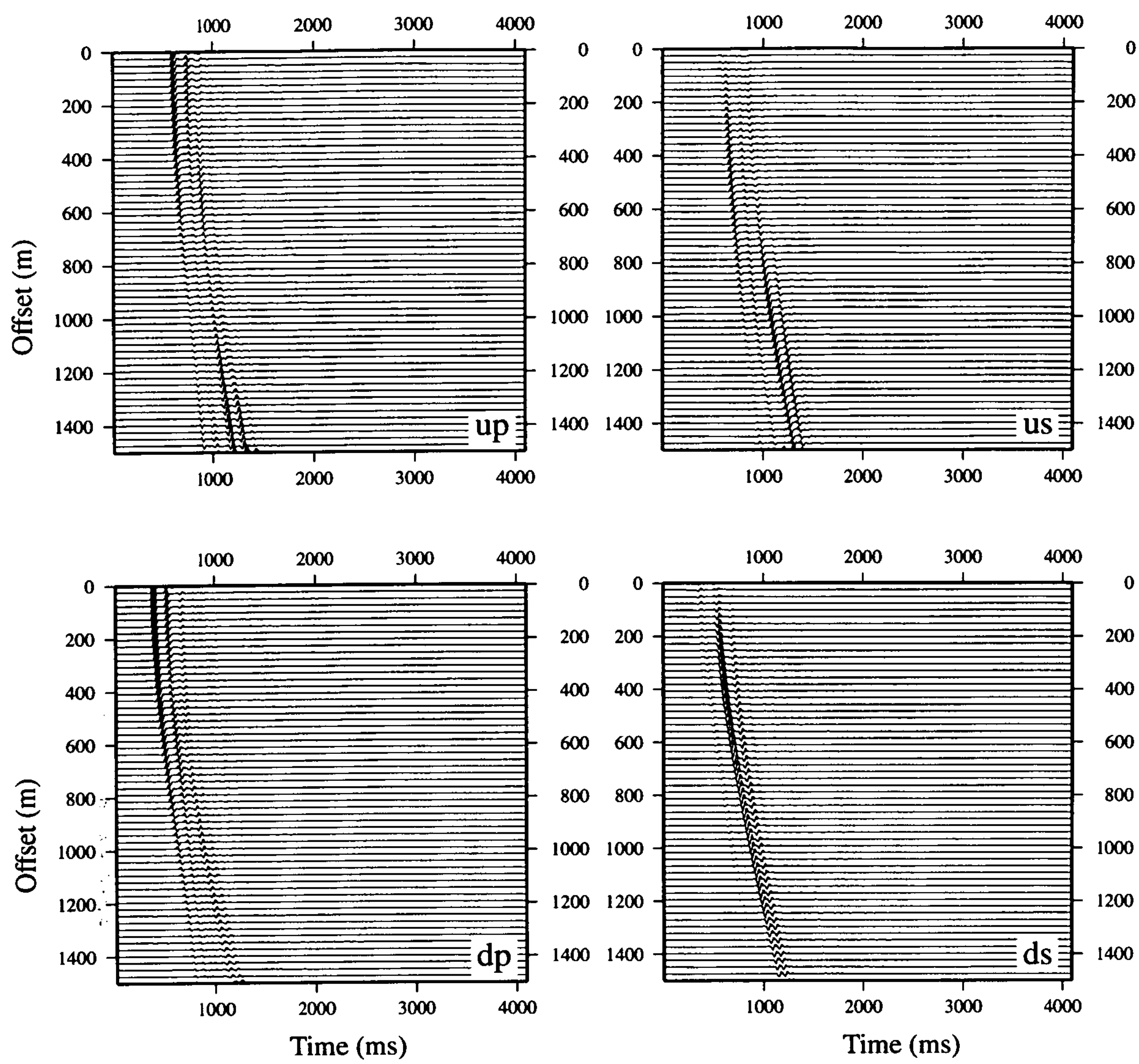

Figure 8.6: Vertical force source data, $P-$ and $S-$ components

near offset-traces for the acoustic and vertical force source are very similar. All evanescent waves are preserved. This is not a true $P-$ $S-$ separation scheme as the $(p^2 - q_\alpha q_\beta)$ term from the denominator in equations (6.23) have not been included as they divide out in the computation of the reflectivities. Dankbaar (1987) shows that acceptable results are obtained if this factor is ignored and suggests that it should be for the computation of the S-wavefield otherwise the separation becomes unstable when q_α becomes complex, that is, when the $P-$ waves become evanescent.

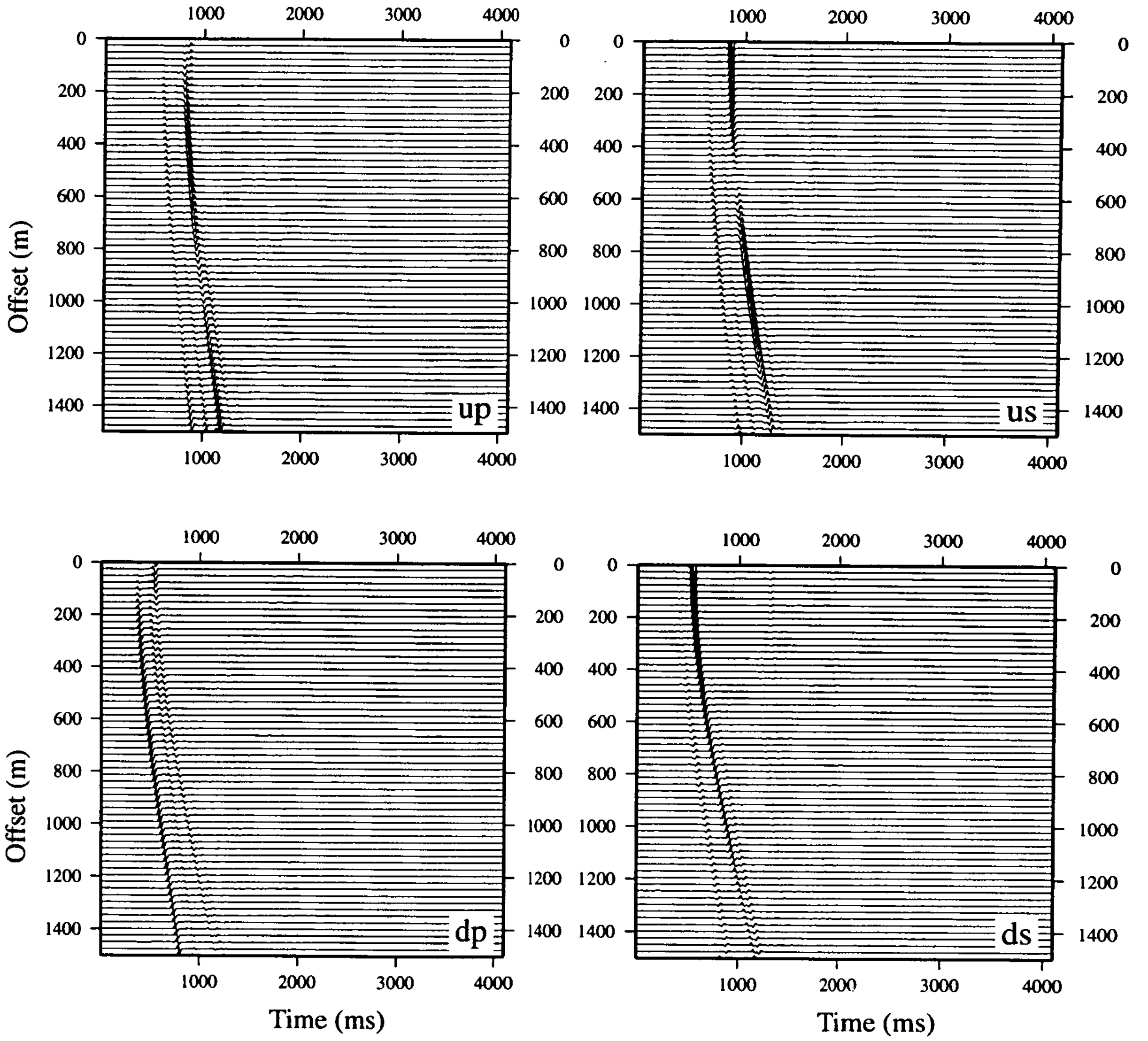

Figure 8.7: Horizontal force source data, $P-$ and $S-$ components

8.4 Recovering the reflectivity

The reflectivity is converted to a wavefield as described in Chapter 6, this wavefield originates from a monopole point source (equations (6.37)). Here the source and receiver level is 500m above the reflecting zone. The medium between the source and receiver levels and the reflecting zone has the same velocities as the receiver level in the original experiment. The results are shown in Figures 8.8, 8.9 and 8.10. The three experiments show very similar results.

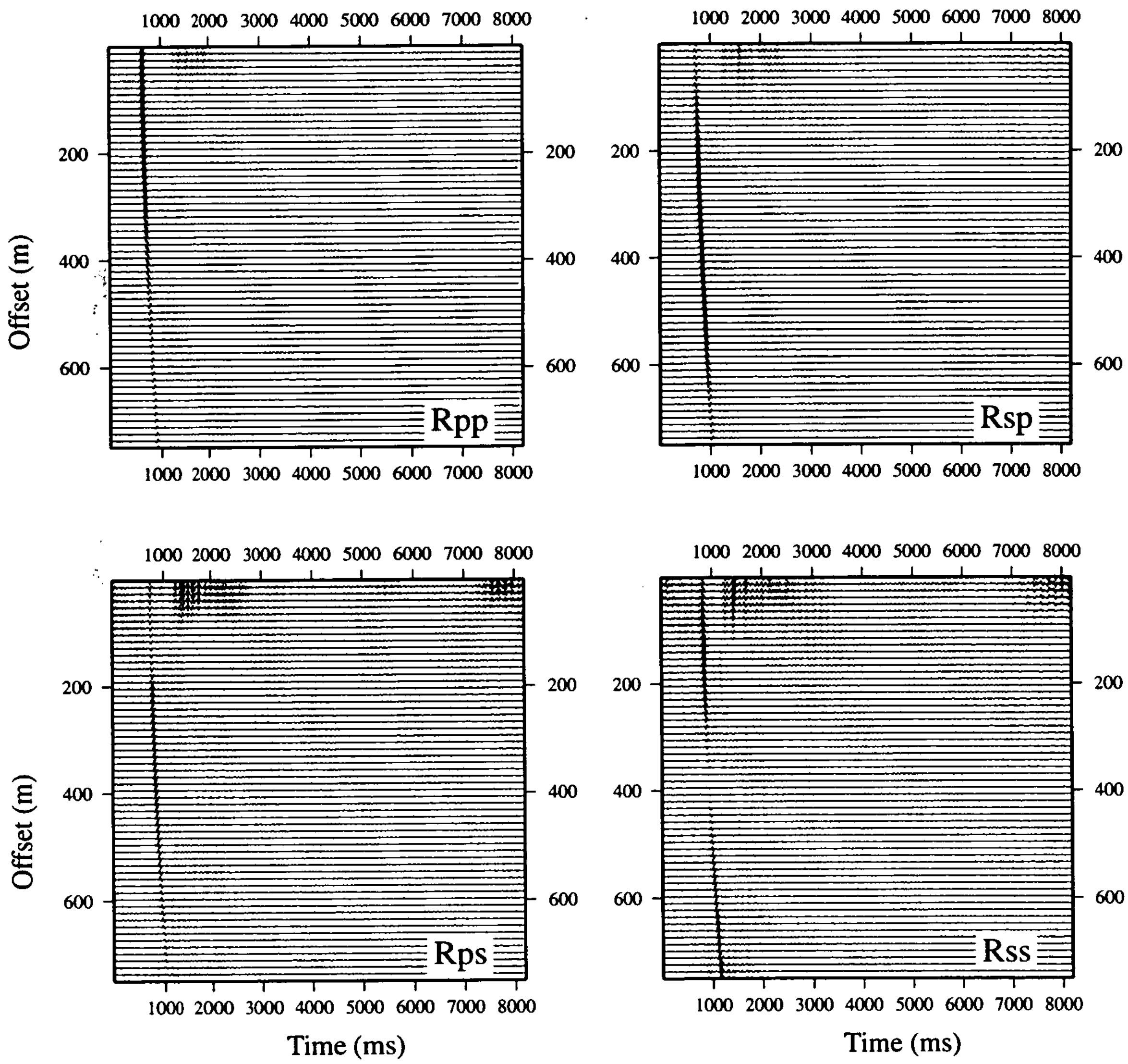

Figure 8.8: Reflectivity wavefields, explosion and vertical–force dual source

At the source a horizontal force and explosion are indistinguishable from one another for horizontally propagating waves. Here the partition of energy between P–waves and S–waves is the same for each source type. However, the value at each point in the (computed) (ω, k_x, k_y) domain, is an average energy over an area, the area being dependent on the sample interval.

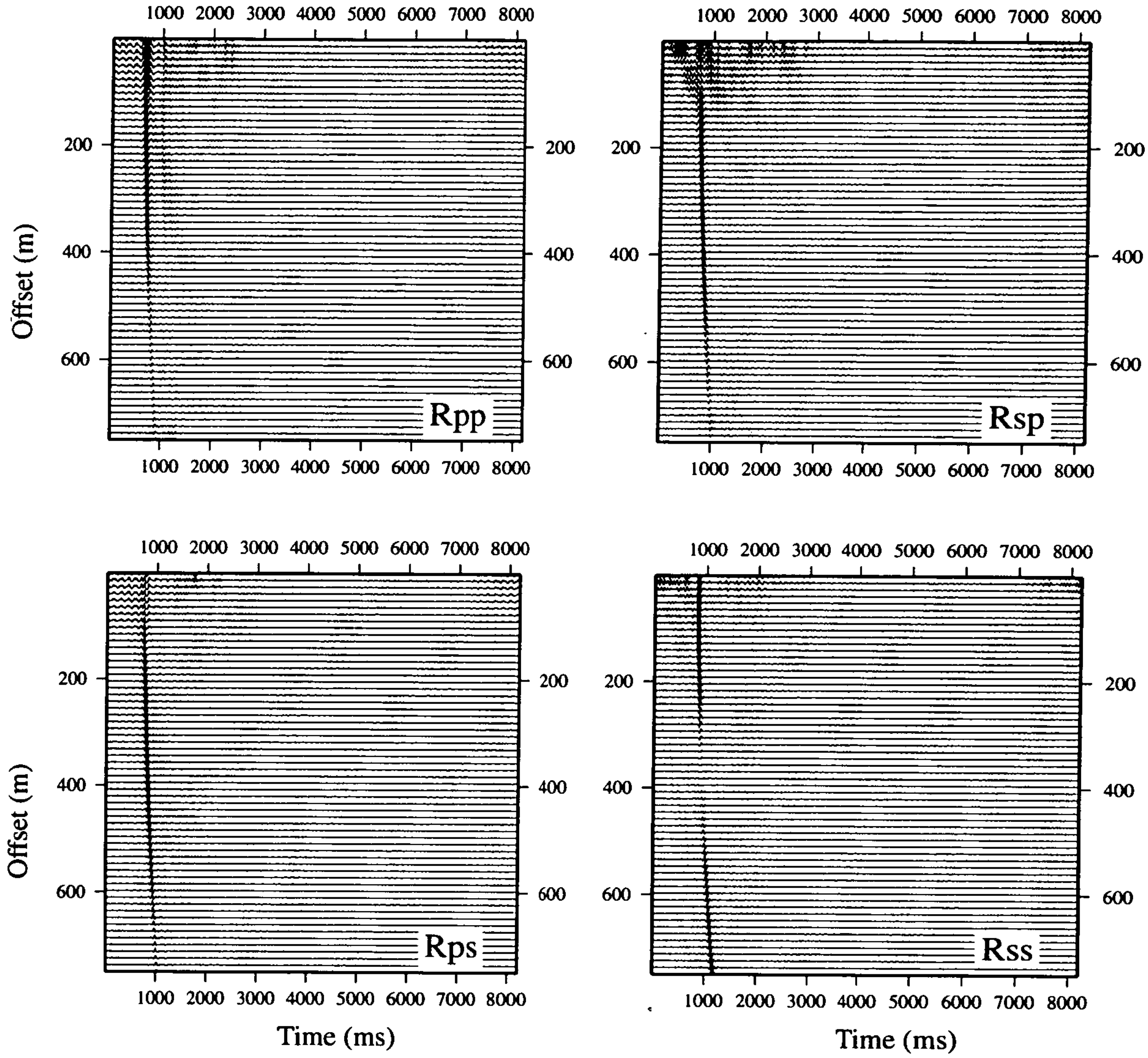

Figure 8.9: Reflectivity wavefields, explosion and horizontal–force dual source

Thus the partition of energy between P–waves and S–waves is made different for all computed slowness by changing the isotropic source to an horizontal force. The same is also true of an explosion and a vertical-force source at zero (horizontal) wavenumber.

In matrix form equations (6.25,6.26) are:

$$\begin{bmatrix} U_S & U'_S \\ U_P & U'_P \end{bmatrix} = \begin{bmatrix} R_{SS} & R_{SP} \\ R_{PS} & R_{PP} \end{bmatrix} \begin{bmatrix} D_S & D'_S \\ D_P & D'_P \end{bmatrix} . \tag{8.1}$$

Denoting the matrix of upgoing wavefields $\boldsymbol{U}$, the matrix of downgoing wavefields $\boldsymbol{D}$ and the

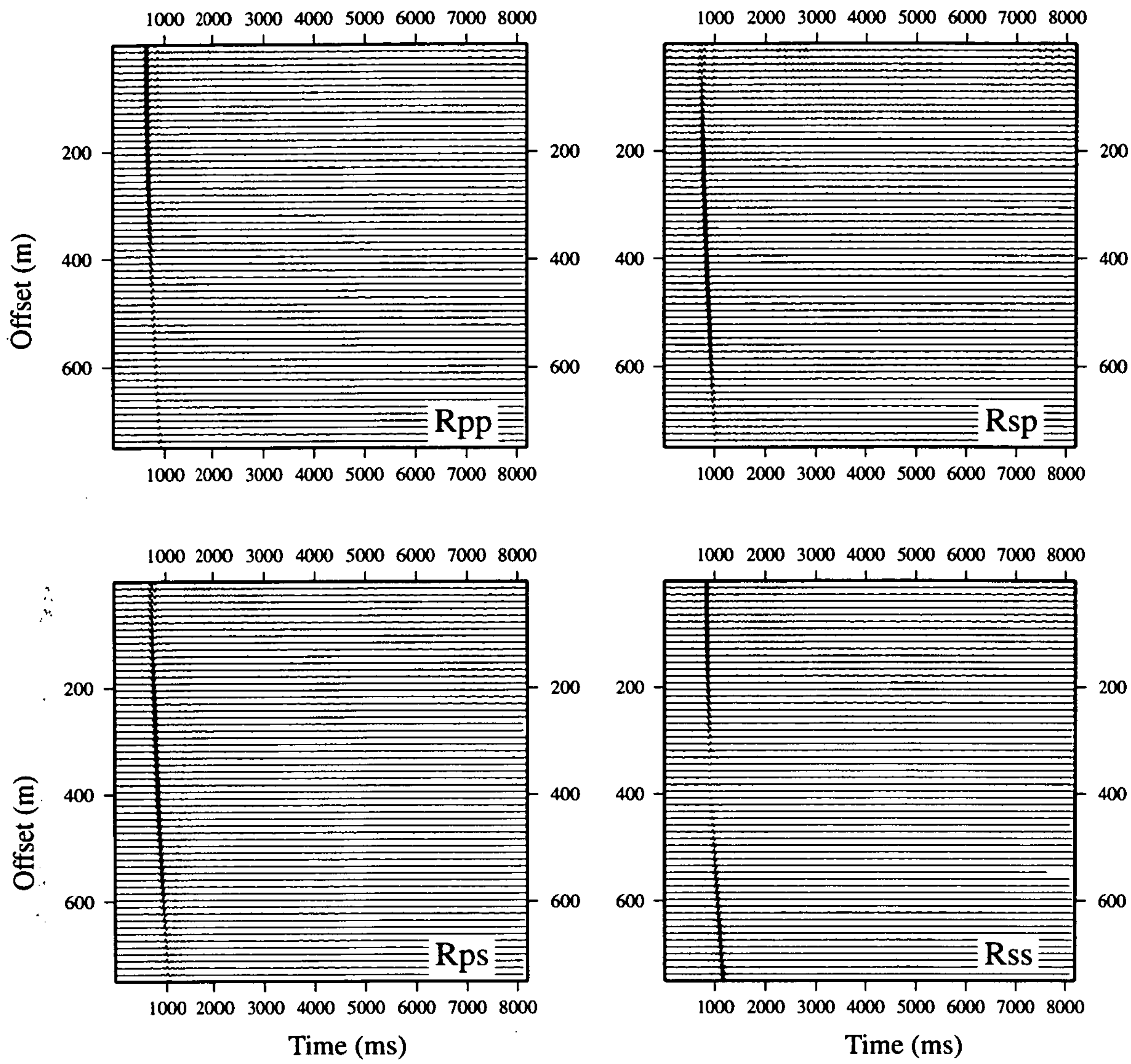

Figure 8.10: Reflectivity wavefields, vertical–force and horizontal–force dual source

matrix of reflectivities $\boldsymbol{R}$ this above equation is

$$\boldsymbol{U} = \boldsymbol{R}\boldsymbol{D}. \tag{8.2}$$

Multiplying both sides by the inverse of $\boldsymbol{D}$ yields:

$$\boldsymbol{U}\boldsymbol{D} = \boldsymbol{R}\boldsymbol{D}\boldsymbol{D}^{-1} = \boldsymbol{R}\boldsymbol{I}, \tag{8.3}$$

which is the matrix form of the recovery equations (6.27). However the inverse of $\boldsymbol{D}$ cannot be constructed when $\boldsymbol{D}$ is singular. That is, when the determinant of $\boldsymbol{D}$ is zero. This occurs when the downgoing wavefields of the first source are a linear combination of the downgoing wavefields for the second source at a point in (ω, k_x, k_y). When the determinant of $\boldsymbol{D}$ is very small then errors in $\boldsymbol{D}$ have a large effect on the computation of $\boldsymbol{R}$. Essentially the inversion is unstable at points in (ω, k_x, k_y) where the eigenvalues of $\boldsymbol{D}$ are small. The effect of this is clearly seen in Figure 8.8. There is much noise in the zero offset traces, especially in the R_{PP} and R_{SP} sections, which correspond to downgoing P–waves, which dominate the near–offset for the acoustic and vertical force source types.

The noise on the near–offset traces corresponding to downgoing S–waves for the acoustic–source/horizontal–source (Figure 8.9) is surprising. Here one would expect that this combination of sources would give optimum results, similar to the vertical–force/horizontal–force source results.

The best results are shown in Figure 8.10, the vertical–force/horizontal–force combination. There is little noise at zero offset and the reflection event is clearly resolved. There are no multiples of events related to the near–surface in the section. There is a small coherent event just after the main arrival in the section corresponding to downgoing P–waves (the R_{PP} and R_{SP} sections). This is probably related to coherent noise in the synthetic data as a result of reflectivity modelling in the (ω, k_r) domain. This scheme does not address such coherent noise.

8.5 Upgoing wavefield reconstruction

The recovered wavefields look correct. Here the recovered reflectivities are used to generate upgoing wavefields using the original downgoing wavefields. If the reflectivities are correct there should be no difference between the original upgoing wavefields and the reconstructed upgoing wavefields. These reconstructed wavefields and the difference between the reconstruction and the original upgoing wavefields are shown in Figures 8.11, 8.12 and 8.13.

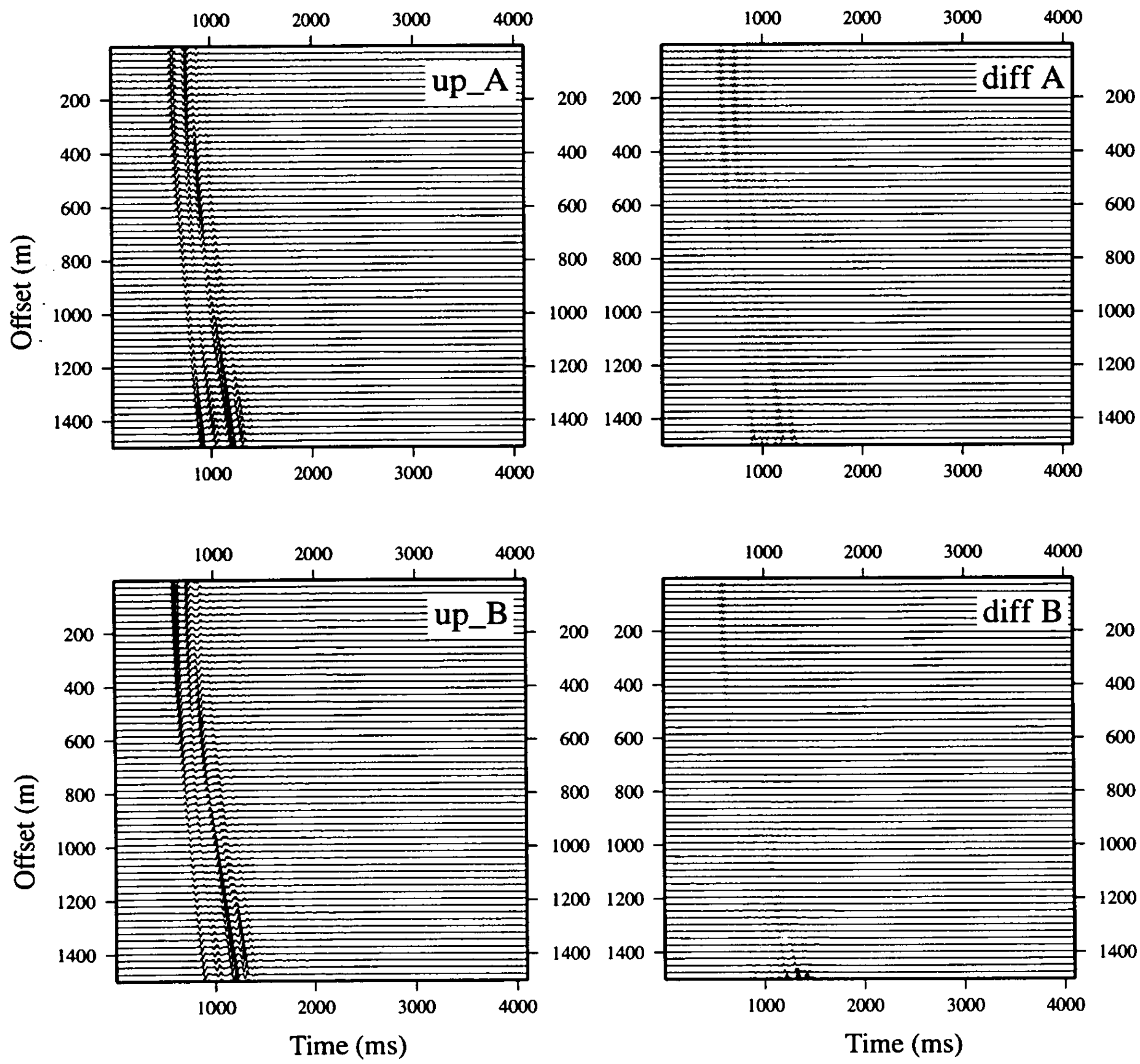

Figure 8.11: Acoustic source data reconstruction and difference

Figure 8.11 is reconstructed from the reflectivity computed using the acoustic/vertical–force dual source and Figures 8.12 and 8.13 are reconstructed from the vertical-force/horizontal–force dual source. The differences are small, less than 1%, for all the reconstructed wavefields.

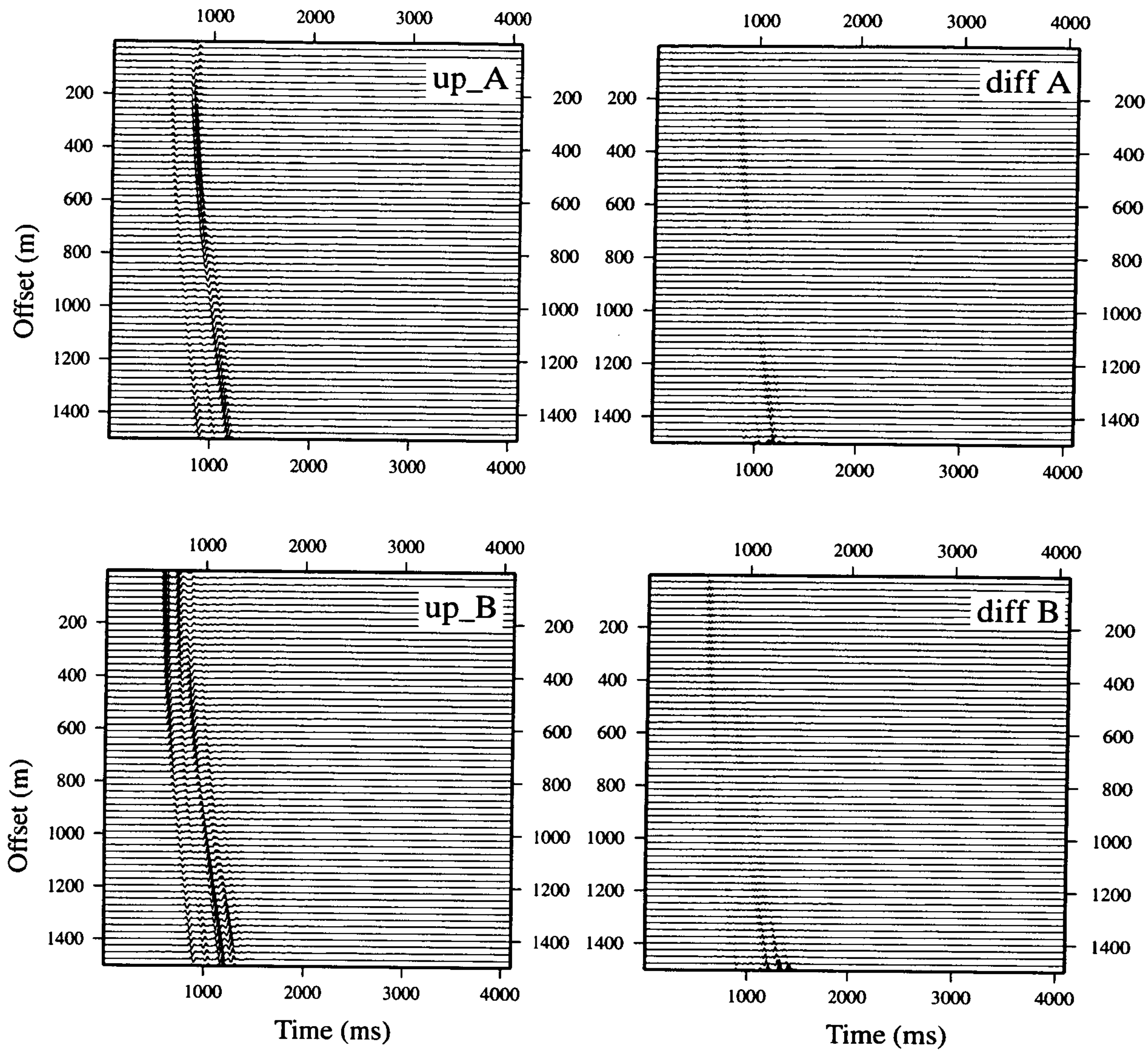

Figure 8.12: Vertical force source data, reconstruction and difference

The most difference is seen on the furthest offset traces. This is where there is an edge in the data and the error is introduced during the transform stages of processing.

8.6 Discussion and initial conclusions

The simple model example works well. The P–waves and S–waves overlap in time but are separated well for all three source types. The reflectivities for each of the three experiments can be used to reconstruct the upgoing wavefields. The difference between the reconstructed wavefields and the original upgoing wavefields is small. The single interface is resolved very clearly.

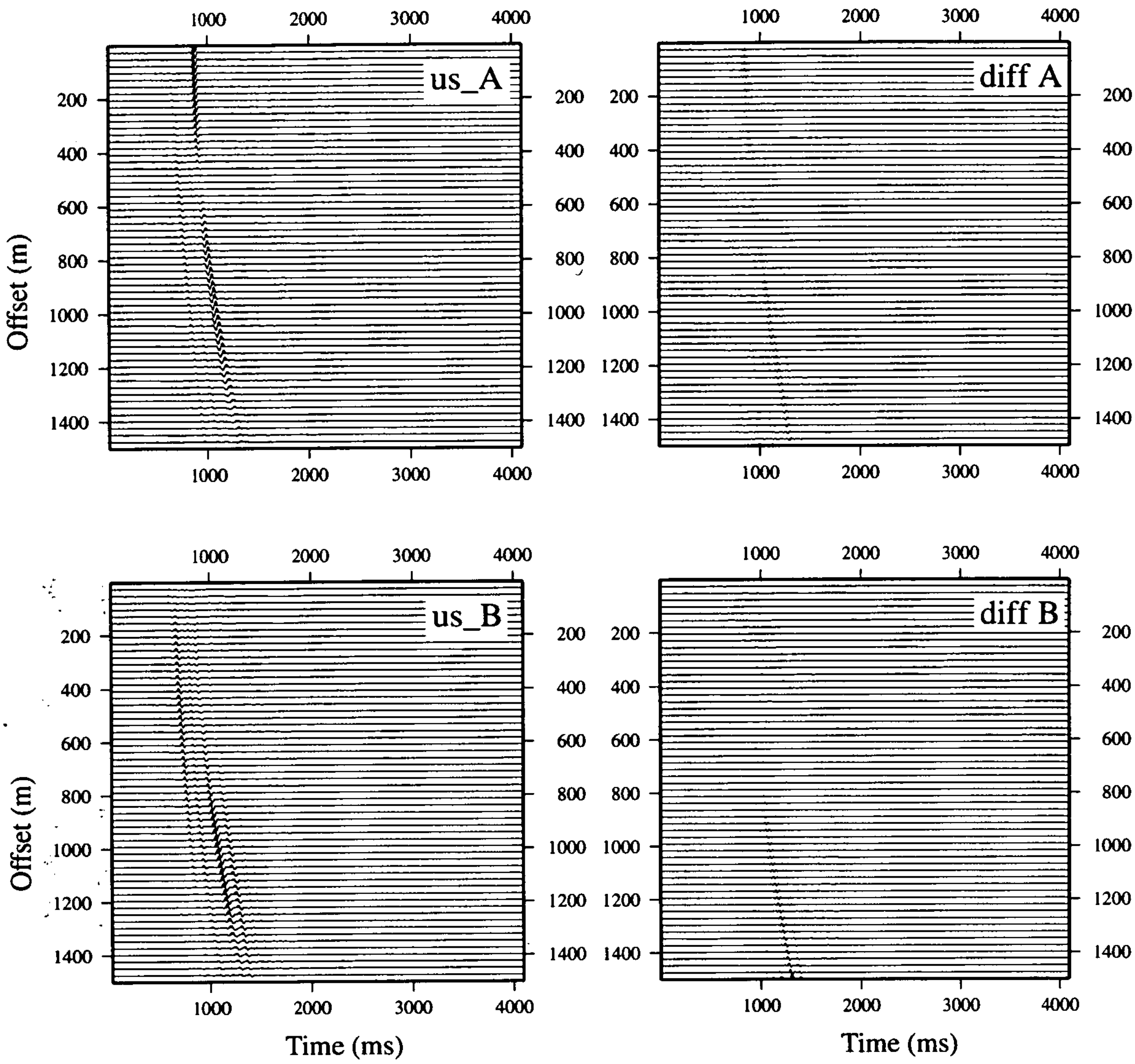

Figure 8.13: Horizontal force source data, reconstruction and difference

The best results are obtained using a vertical–force/horizontal–force dual source. This is the only combination for which the partition of energy between $P-$ and $S-$ is different for *all* wavenumbers. The other source combinations work well for non–near offsets.

8.7 Complex (synthetic) data example

Here a more complex earth model is used. The source and receiver geometry is the same as for the simple example. Only the vertical-force/horizontal force combination is used. The

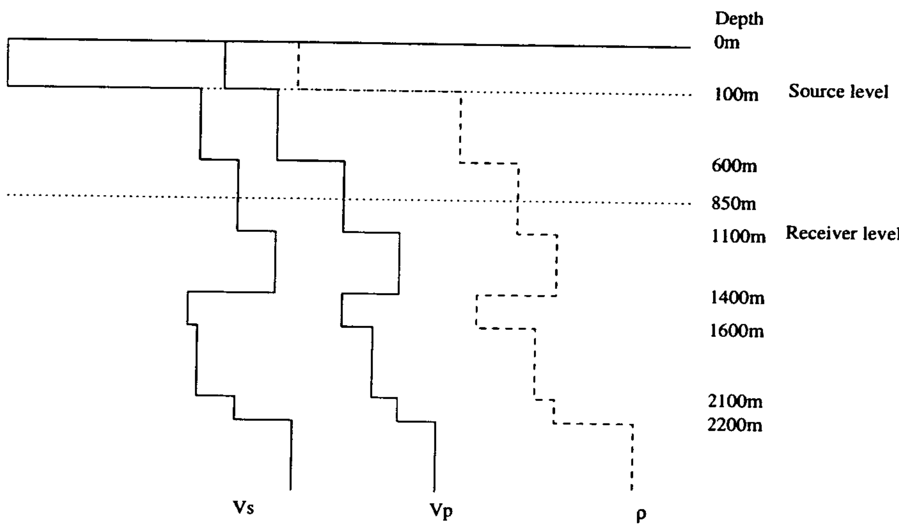

Figure 8.14: Complex earth model

Layer	V_p (m/s)	V_s (m/s)	ρ (g/cm^3)	Thickness (m)
1	1500	0	1	100
2	1900	130	2.1	500
3	2300	1600	2.4	500
4	2800	1900	2.6	300
5	2300	1200	2.2	200
6	2500	1250	2.3	500
7	2800	1400	2.4	100
8	3000	2000	2.9	∞

Table 8.2: Complex earth model

model is shown in Table 8.2 and Figure 8.14.

The sources are placed on the sea-bed. The receiver depth is again 850m and the shot spacing 25m. There are 60 shots ranging in offset from 0m to 1500m.

The synthetic seismograms are shown in Figures 8.15 (vertical force) and 8.16 (horizontal force). The seismograms are much more complex than the previous example and again the $P-$ and $S-$ wavefields overlap in time.

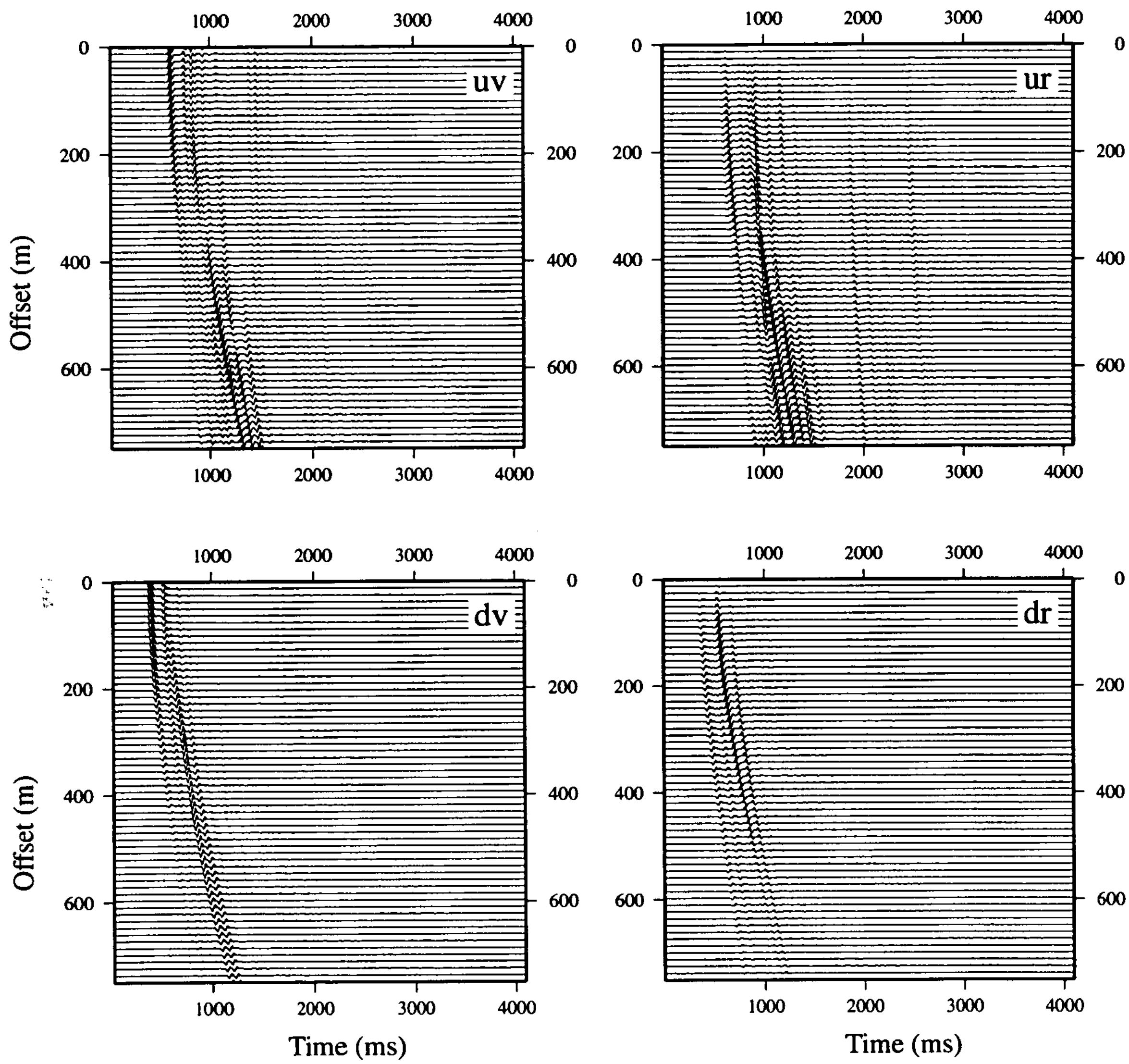

Figure 8.15: Vertical force source data. Complex model

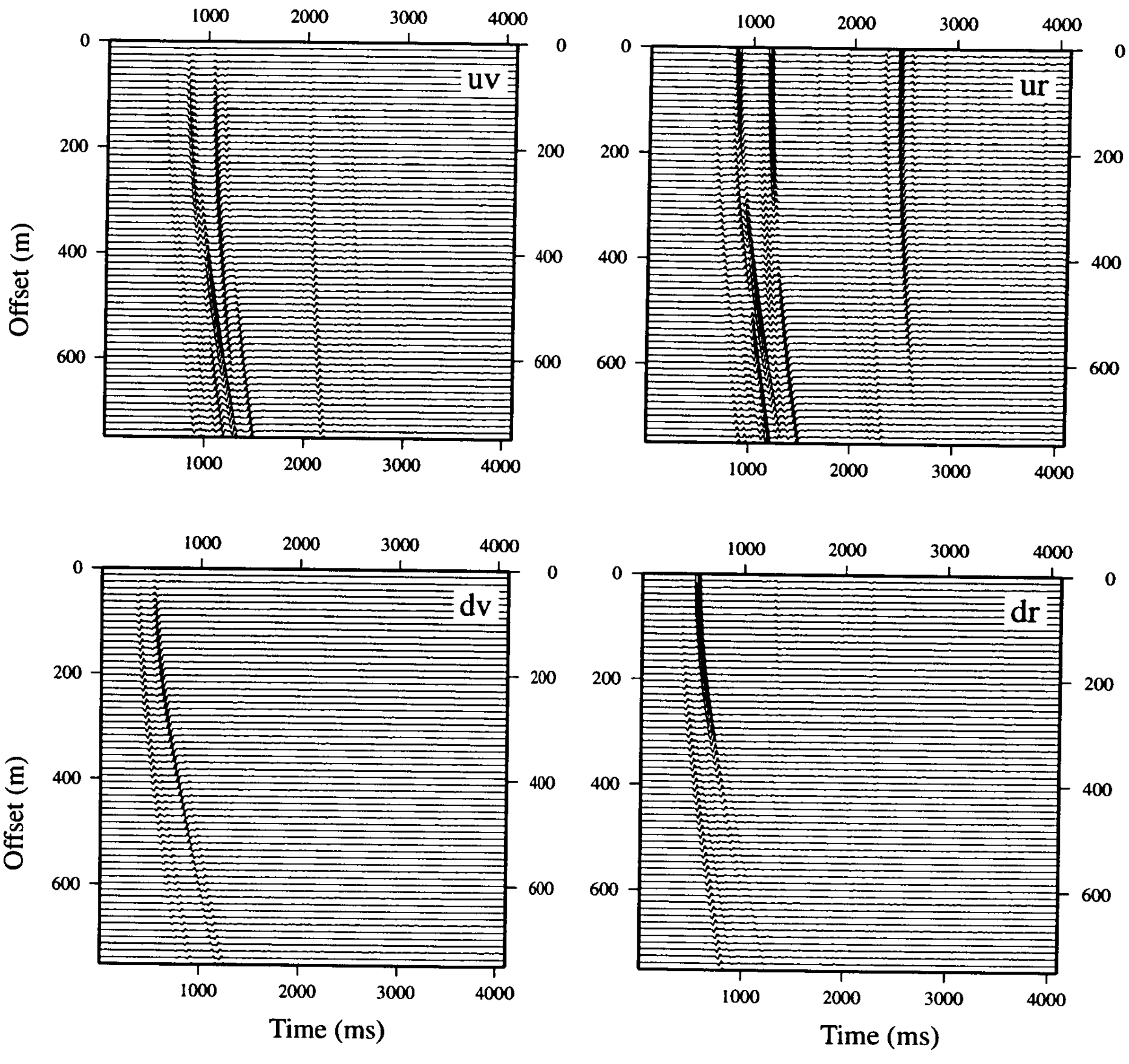

Figure 8.16: Horizontal force source data, Complex model

The $P-S-$separation works well. The wavefields being clearly separated for both sources

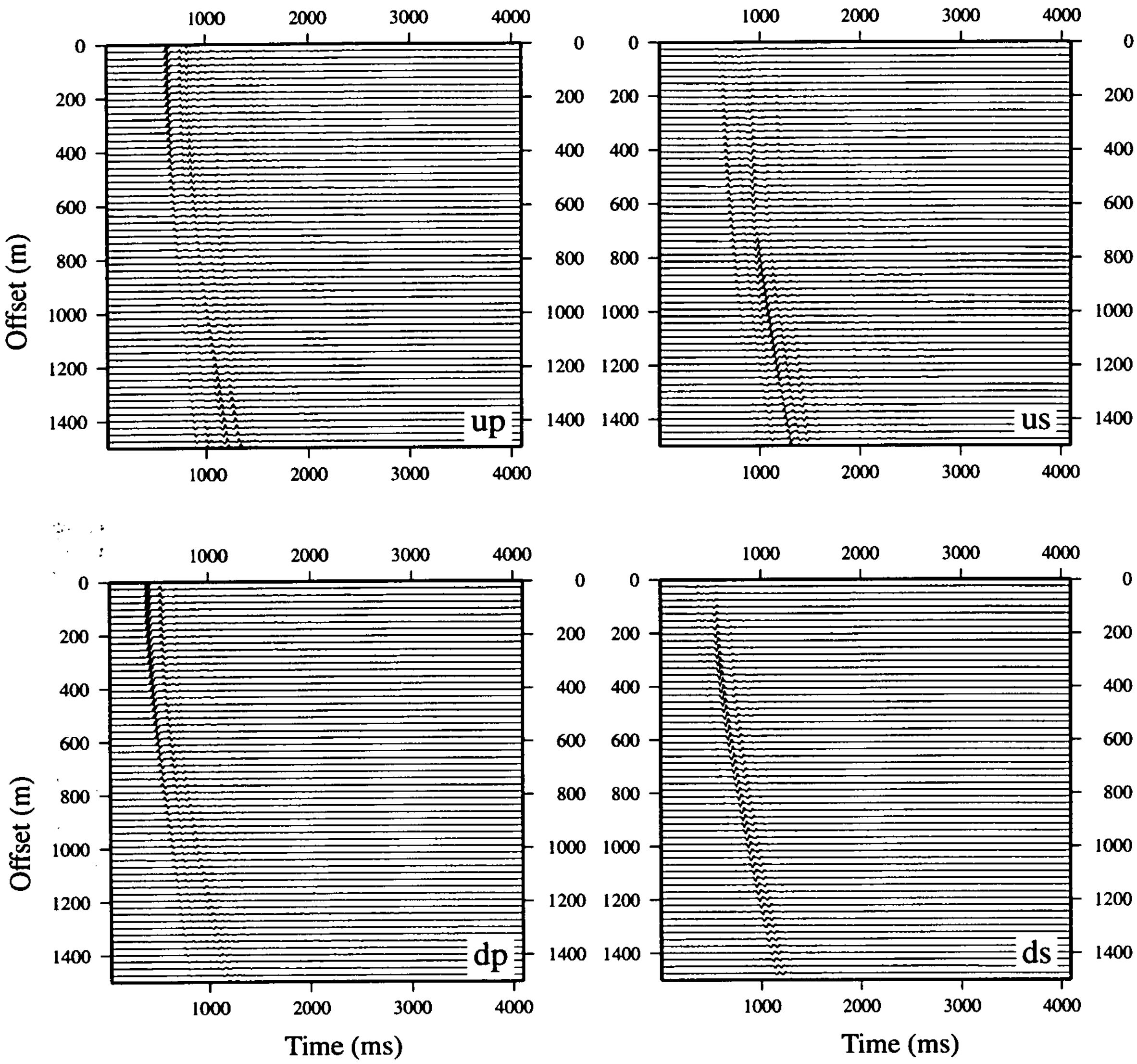

Figure 8.17: Vertical force source, mode separated data. Complex model

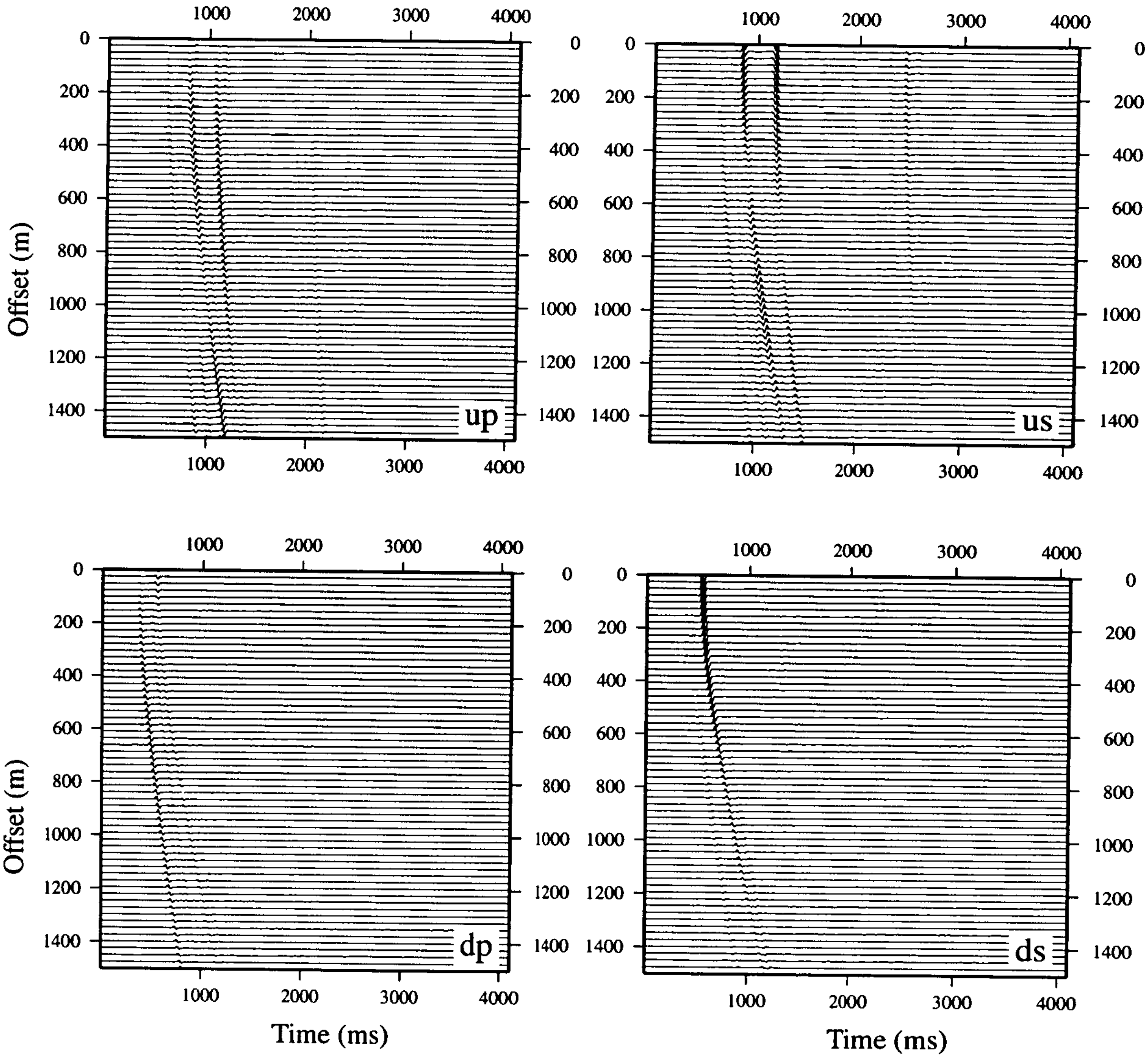

Figure 8.18: Horizontal force source, mode separated data, Complex model

The final reflectivity is plotted such that each component is plotted in the same scale. Notice that the amplitude and arrival times of the R_{PS} and R_{SP} sections are very similar, as one might expect.

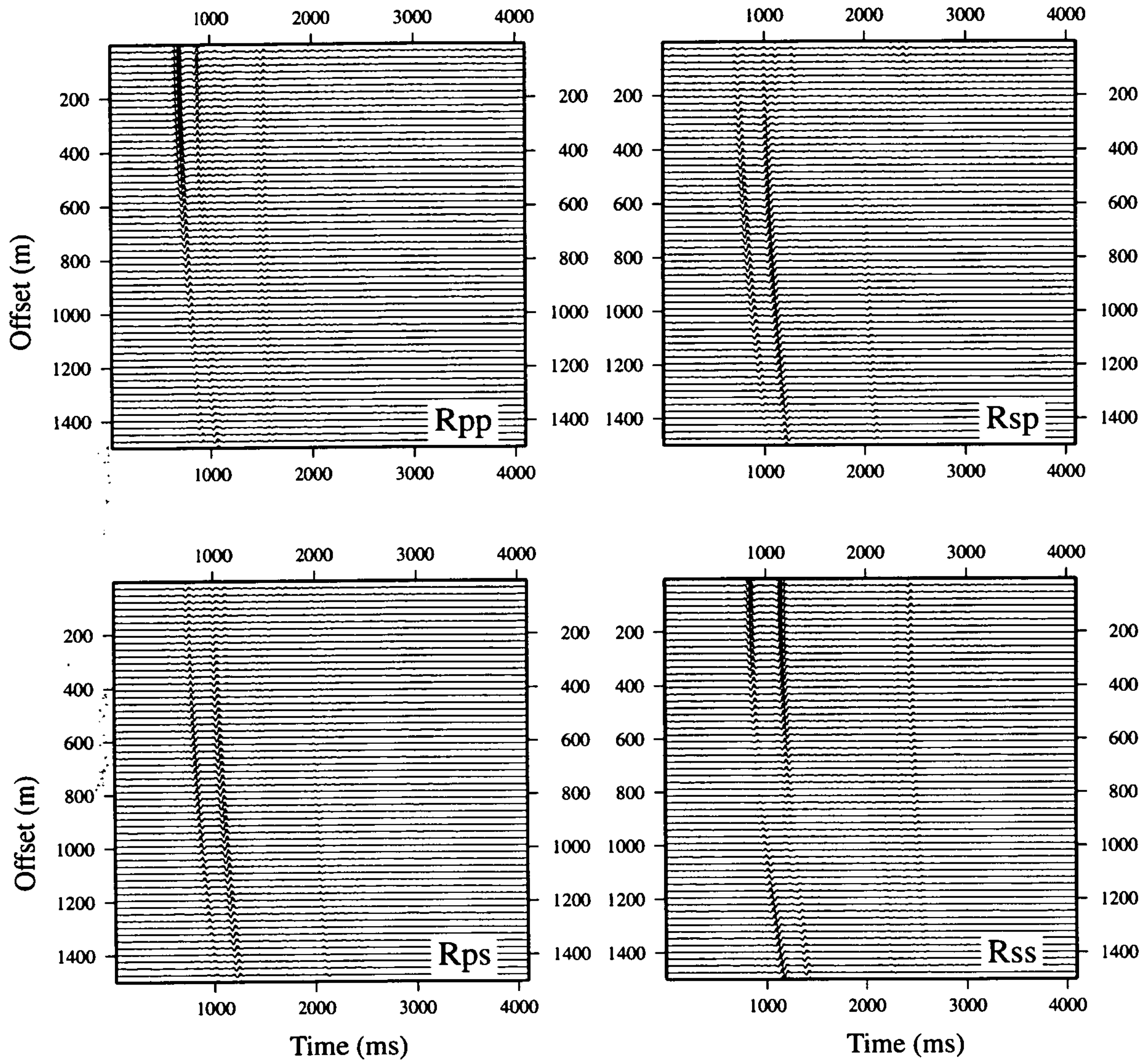

Figure 8.19: Recovered reflectivity. Complex model

8.8 Conclusions

The scheme works well. The recovered reflectivities can be used to reconstruct the upgoing wavefields and the difference between the reconstructed wavefields and the original upgoing wavefields is small. The best results are obtained using a vertical–force/horizontal–force combination. However reasonable results are obtained using an acoustic source as one of the sources.

CONCLUSIONS

Chapter 9

In this chapter the conclusions are discussed and summarised. Suggestions and speculations for future work are made.

9.1 Conclusions

Two main themes have been explored in this thesis; wavelet shaping to remove the effect of shot–to–shot variations in borehole seismic data, and recovering the reflectivity beneath the receiver for walkaway VSP by wavefield division in the frequency–wavenumber domain. These themes are not separate as the first is a pre–requisite for the second. The transform to the frequency–wavenumber domain cannot be computed correctly if there is source signature variation in the data to be transformed. The wavefield division and therefore reflectivity recovery cannot be achieved if the transform cannot be computed.

In Chapter 4 I showed how the pressure measurement made at a hydrophone near the source is related to the particle displacement recorded at a downhole geophone. This is based on the analysis of Lamb (1923) and Ziolkowski (1998). The source (pressure) wavelet recorded at the hydrophone is the same as the particle velocity measured at the geophone. Thus any wavelet processing can be carried out using a linear convolutional model. Chapter 5 demonstrates how wavelet shaping is carried out in practice. As has been stated, there are references to work by Zeitvogel, which I am unable to find. The wavelet shaping scheme is dependent on knowing r the source—hydrophone distance and R the virtual–source—hydrophone distance. For the examples presented in this thesis r is constant. R however, varies with wave height. The appendix to Chapter 5 demonstrates that variations in R of about 1m have a negligible effect on the source wavelet shaping scheme. How sea-bed–source wavelets are recorded, related to the downhole particle velocity and shaped to remove the effect of shot–to–shot variations has not been discussed.

Using the formulation of Kennett (1983) in Chapter 6 I show how the reflectivity of the region beneath the receiver can be recovered. Two sources must be used which have differing partitions of energy between P–waves and S–waves for all points in (ω, k_x, k_y). This cannot be done using only a single source as any upgoing wavefield is a linear combination of two down going wavefields. The recovery scheme relies on dividing two wavefield combinations. The stabilisation of this division and an example of the application is also presented. A by–product of the recovery scheme is that the wavefield is separated into $P-$ and $S-$ components.

The data are processed in the (ω, k_x, k_y) domain. Chapter 7 describes the transformation of the data to this domain. The earth is assumed to be laterally invariant. The transform uses complex frequencies to prevent poles at zero (vertical) wavenumber in the transform domain causing division by zero when the wavefields are scaled prior to inverse transform to (t, x). The data are pre–processed prior to transform to prevent processing artifacts.

In the previous chapter (Chapter 8) I show application of the recovery scheme to synthetic data. The reflectivities are recovered well. As a test, the upgoing wavefields are reconstructed using the recovered reflectivities. The difference between the reconstructed and original wavefields is small, except at far offset where edge effects in the transform caused errors to be introduced. The best results are obtained using a vertical–force/horizontal–force combination, for which the partition between $P-$ and $S-$ energy is different for *all* points in (ω, k_x, k_y). Reasonable results are obtained if an acoustic source is used as one of the sources. Thus experiments that are designed with this technique in mind should use a vertical–force/horizontal–force combination, however it is possible that acoustic source data may already exist in which case a horizontal–force source should be used for the repeat experiment as this will allow the near–offset reflectivity to be recovered.

In conclusion, a dual source VSP in which the source wavelet is constant shot–to–shot, can be inverted for the (tensor) reflection response of the region beneath the receiver, for a plane horizontally layered earth. The velocities V_P and V_S must be known at the receiver. The wavelets for the two sources should be shaped so that they have the same bandwidth; this is done using the scheme of Chapter 6.

9.2 Suggestions for further work and speculation

This work must be tested on real data. As yet no data exist which are suitable. The real earth is three–dimensional, testing on real–data will show how well this scheme, developed for a one–dimensional earth, will work for a three–dimensional earth.

A key problem which will require resolution is that of the stability of the sea–bed source. No information is available about the sea–bed sources currently being developed other than a basic outline of their operation. As with the land vibrator sources, source shot–to–shot variability will depend on the near–surface conditions. How this source is measured and how the measurement relates to the downhole wavefield needs to be addressed. How the source will be measured and how this measurement relates to the downhole wavefield is as yet not known.

An obvious extension of this work is to nine–component experiments: three–orthogonal sources and three orthogonal receivers. This would possibly allow for the recovery of the *full* tensor response of an anisotropic earth. The equations for the full wavefield at the receiver are presented in Fryer and Frazer (1984). The wavefield separation would require an anisotropic velocity model of the receiver medium. The wavefield will no longer be symmetrical about the origin for non–azimuthally symmetric earth models so the velocity model must be azimuth dependent. Extending the transform to three–dimensional recording geometries is simple; the real x, y data are used instead of interpolating the single line data to x and y.

If the reflectivity of the region beneath the receiver changes with time it may be possible to carry out repeat experiments to monitor this change, although, as is the case with all time–lapse studies, one must be very careful to make sure that the response is of geological origin rather than an artifact of the processing.

REFERENCES

Ahmed, H., 1989. Application of mode converted shear waves to rock property estimation from vertical seismic profiling data. *Geophysics*, **54**(4):pages 478–485.

Ahmed, H., Dillion, P., Johnstad, S., and **Johnston, C.**, 1986. Northern Viking graben multilevel three-component walkaway VSPs. *First Break*, **10**(4):pages 9–27.

Aki, K. and **Richards, P.**, 1980. Quantitative Seismology, volume 1. Freeman.

Båth, M., 1968. Mathematical Aspects of Seismology. Elsevier.

Beydoun, W., 1984. Seismic tool–formation coupling in boreholes, Chapter 2, pages 80–86. In Toksöz and Stewart (1984).

Bracewell, R. N., 1986. The Fourier Transform and its Applications. McGraw–Hill.

Brekhovskikh, L. D., 1960. Waves in Layered Media. Academic Press, New York.

Cheng, C. H. and **Toksöz, M. N.**, 1984. Generation, propagation and analysis of tube wave in a borehole, Chapter 5, pages 276–287. In Toksöz and Stewart (1984).

Dankbaar, J. M. M., 1987. Vertical seismic profiling – Separation of P- and S-waves. *Geophysical Prospecting*, **35**:pages 803–814.

Dillon, P. B. and **Collyer, V. A.**, 1985. On timing the VSP first arrival. *Geophysical Prospecting*, **33**:pages 1174–1194.

DiSiena, J. P., Byun, B. S., Fix, J. E., and **Gaiser, J. E.**, 1984a. F-K analysis and tube wave filtering, Chapter 5, pages 288–301. In Toksöz and Stewart (1984).

DiSiena, J. P., Gaiser, J., and **Corrigan, D.**, 1984b. Horizontal components and shear wave data of three–component VSP data, Chapter 4, pages 177–188. In Toksöz and Stewart (1984).

Dix, C. H., 1936. Interpretation of well shot data. *Geophysics*, **4**:pages 24–32.

Dougherty, M., **Vincent, R.**, **Swift, S.**, and **Stephen, R.**, 1995. Anisotropic scattering in old Alantic crust. *Journal of Geophysical Research*, **100**(B7):pages 10095–10106.

Esmersoy, C., 1984. Polarization analysis, rotation and velocity estimation in three–component VSP, Chapter 2, pages 236–256. In Toksöz and Stewart (1984).

Esmersoy, C., 1990. Inversion of P and SV waves from multicomponent offset vertical seismic profiles. *Geophysics*, **55**(1):pages 39–50.

Ewing, W. M., **Jardetzky, W. S.**, and **Press, F.**, 1957. Elastic Waves in Layered Media. McGraw–Hill.

Fessenden, R. A., 1917. Method and apparatus for locating ore bodies. *U.S. Patent No. 1240328.*

Fryer, G. J. and **Frazer, L. N.**, 1984. Seismic waves in stratified anisotropic media. *Geophysical Journal of the Royal Astronomical Society*, **78**:pages 691–710.

Gal'perin, E. I., 1974. Vertical Seismic Profiling, volume 12 of *Special Publications*. Society of Exploration Geophysics. English translation of Галвперин (1971).

Галвперин, Е. И., 1971. Вертикапное Сеисмическое Профилрование. Москва. In Russian.

Hardage, B. A., 1983. Vertical Seismic Profiling, Part A principles. Number 14 in Handbook of Seismic Exploration. Elsevier.

Higgins, M. and **MacBeth, C.**, 1995. Determination of subsurface anisotropy using near–offset VSP. In *Technical Abstracts*. Joint Association for Geophysics, United Kingdom Geophysical Assembly.

Higgins, M., **MacBeth, C.**, and **Zilokowski, A.**, 1998. Overburden correction for marine walkaway VSP. In *Technical Abstracts*. European Association of Geoscientists and Engineers.

Higgins, M., **Ziolkowski, A.**, and **MacBeth, C.**, 1997. Source signature processing in marine VSP. In *Technical Abstracts*. European Association of Geoscientists and Engineers.

Hokstad, K., **Landrø, M.**, and **Mittet, R.**, 1996. Estimation of effective source signatures from marine VSP data. *Geophysical Prospecting*, **44**:pages 179–196.

Kennet, P., **Ireson, R.**, and **Conn, P.**, 1980. Vertical seismic profiles: their use in exploration geophysics. *Geophysical Prospecting*, **28**:pages 676–699.

Kennett, B., 1979. The supression of surface multiples on seismic records. *Geophysical Prospecting*, **27**:pages 584–600.

Kennett, B. L. N., 1981. Elastic Wave Propagation in Stratified Media, volume 21 of *Advances in Applied Mechanics*, Chapter 2, pages 80–167. Academic Press Inc, 111 Fith Avenue, New York.

Kennett, B. L. N., 1983. Seismic Waves in Stratified Media. Cambridge University Press.

Kommedal, J. and **Tjøstheim, B.**, 1989. A study of different methods of wavefield separation for application to VSP data. *Geophysical Prospecting*, **37**:pages 117–142.

Lamb, H., 1923. The early stages of a submarine explosion. *Philosophical Magazine*, **47**(257).

Lee, M. W., 1984. Processing of vertical seismic profile data. *Advances in Geophysical Data Processing*, **1**:pages 129–160.

MacBeth, C., 1995. How can anisotropy be used for reservoir characterisation? *First Break*, **13**(1):pages 31–37.

MacBeth, C., **Boyd, M.**, **Rizer, W.**, and **Queen, J.**, 1998. Eastimation of resevoir fracturing from marine VSP using local shear-wave conversion. *Geophysical Prospecting*, **46**:pages 29–50.

MacBeth, C. and **Liu, E.**, 1994a. Efficient conversion to shear waves at near-normal incidence in marine VSP's. In *Technical Abstracts*. European Association of Geoscientists and Engineers.

MacBeth, C. and **Liu, E.**, 1994b. The problem of water–column multiples for processing converted S waves in marine VSP data. *Geophysical Journal International*, **119**:pages 999–1004.

Menke, W. and **Abbott, D.**, 1990. Geophysical Inverse Theory. Columbia University Press, New York.

Parkes, G. and **Hatton, L.**, 1986. The Marine Seismic Source. D. Reidel Publishing.

Rayleigh, L., 1917. On the pressure developed in a liquid during the collapse of a shperical cavity. *Philosophical Magazine*, **24**:pages 94–98.

Schruth, P. K., **Bush, I.**, and **Digranes, P.**, 1992. Observations of shear-wave splitting from VSPs in the northern North Sea. In *Technical abstracts*. European Association of Geoscientists and Engineers.

Schutz, B., 1980. Geometrical Methods of Mathematical Physics. Cambridge University Press.

Seeman, B. and **Horowicz, L.**, 1983. Vertical seismic profiling: separation of up and down going acoustic waves in stratified media. *Geophysics*, **48**:pages 555–568.

SEG, editor, 1989. Research Workshop on Recording and Processing Vector Wavefield Data. Society of Exploration Geophysics.

Smidt, J. M., 1989. VSP processing with full downgoing–wavefield deconvolution applied to the total wavefield. *First Break*, **7**(6):pages 247–257.

Sneddon, Z., 1998. Tube–Wave Filtering for Uniwell Data. Master's thesis, University of Edinburgh.

Sommerfeld, A., 1909. Über die Ausbeitung der Wellen in der drahtlosen Telegraphie. *Ann. Physick*, **28**:pages 665–736.

Spencer, T., **Davis, F. E.**, **Chuan, W.-R.**, and **Zeitvogel, M.**, 1984. VSP measurement of seismic attenuation. *Geophysics*, **49**(5):pages 667.

Tariel, P. and **Michon, D.**, 1984. On vertical seismic profile processing. *Geophysical Prospecting*, **32**:pages 755–789.

Taylor, D. B., 1992. Anisies version 4.5 Reference Manual.

Toksöz, M. and **Stewart, R.**, 1984. Vertical Seismic Profiling: Part B Advanced concepts. Handbook of Geophysical Exploration. Elsevier.

Vershuur, D. J., **Berkhout, A. J.**, and **Wapenaar, C. P. A.**, 1992. Adaptive surface-related multiple elimination. *Geophysics*, **57**(9):pages 1166–1177.

Weyl, H., 1919. Ausbreitung electromagnetisher Wellwn über einen ebenen Leiter. *Ann. Physick*, **60**:pages 481–500.

Wiggins, J. W., 1988. Attenuation of complex water–bottom multiples by wave–equation–based prediction and subtraction. *Geophysics*, **53**(12):pages 1527–1539.

Wild, P., **MacBeth, C.**, **Crampin, S.**, **Li, X.-Y.**, and **Yardley, G.**, 1993. Processing and interpreting vector wavefield data. *Canadian Journal of Exploration Geophysics*.

Ziolkowski, A., 1970. A method for calculating the output pressure waveform from an airgun. *Geophysical Journal of the Royal Astronomical Society*, **21**:pages 137–161.

Ziolkowski, A., 1982. An airgun model which includes heat transfer and bubble interactions. In *Technical Abstacts*, pages 187–189. Society of Exploration Geophysics.

Ziolkowski, A., 1991. Why don't we measure seismic signatures? *Geophysics*, **56**(2):pages 190–201.

Ziolkowski, A., 1998. Theory for the measurement of air gun bubble oscillations. *Geophysics*. In press.

Ziolkowski, A. and **Johnston, R. G. K.**, 1997. Marine seismic sources: QC of wavefield computation from near–field measurements. *Geophysical Prospecting*, **445**:pages 611–639.

Ziolkowski, A., Parkes, G., Hatton, L., and **Haughland, T.**, 1982. The signature of an air gun array: Computation from near-field measurements including interactions. *Geophysics*, **47**(10):pages 1413–1421.

SENSITIVITY OF SOURCE MEASUREMENT DEGHOSTING

Appendix A

Here an analysis of the sensitivity of the deghosting scheme to variations in R is presented. The hydrophone is assumed to be fixed relative to the source, as is the case for the data presented. Equation (5.5) is written :

$$\frac{M(\omega)}{S(\omega)} = \left[\frac{\exp\{i\omega r/c\}}{r} - \frac{\exp\{i\omega R/c\}}{R}\right] = T. \tag{A.1}$$

which is written

$$\frac{1}{S} = \frac{1}{M}\left[\frac{\exp\{i\omega r/c\}}{r} - \frac{\exp\{i\omega R/c\}}{R}\right] = \frac{1}{M}\frac{T}{1}. \tag{A.2}$$

Consider what happens when the transfer function T is perturbed by δr and δR. To first order, the Taylor expansion of T about (r_0, R_0) is

$$T(r_0 + \delta r, R_0 + \delta R) = T(r_0, R_0) + \frac{\partial T(r_0, R_0)}{\partial r}\delta r + \frac{\partial T(r_0, R_0)}{\partial R}\delta R. \tag{A.3}$$

The first derivatives of T are:

$$\frac{\partial T}{\partial r} = \frac{e^{i\omega r/c}}{r}\left(\frac{i\omega}{c} - \frac{1}{r}\right), \tag{A.4}$$

with respect to r and

$$\frac{\partial T}{\partial R} = -\frac{e^{i\omega rR/c}}{R}\left(\frac{i\omega}{c} - \frac{1}{R}\right), \tag{A.5}$$

with respect to R. Substituting (A.4) and (A.5) into (A.3) the inverse of the source function is:

$$\frac{1}{S} = \frac{T}{M}\left[1 + \frac{\frac{e^{i\omega r/c}}{r}\left[\frac{i\omega}{c} - \frac{1}{r}\right]}{\frac{e^{i\omega r/c}}{r} - \frac{e^{i\omega R/c}}{R}}\delta r - \frac{\frac{e^{i\omega R/c}}{R}\left[\frac{i\omega}{c} - \frac{1}{R}\right]}{\frac{e^{i\omega r/c}}{r} - \frac{e^{i\omega R/c}}{R}}\delta R\right], \tag{A.6}$$

which is

$$\frac{1}{S} = \frac{T}{M}\left[1 + \frac{\frac{i\omega}{c} - \frac{1}{r}}{1 - \frac{re^{i\omega(R-r)/c}}{R}}\delta r - \frac{\frac{i\omega}{c} - \frac{1}{R}}{\frac{Re^{i\omega(r-R)/c}}{r} - 1}\delta R\right]. \tag{A.7}$$

The squared modulus of each of the perturbing terms is:

$$\left|\frac{\frac{i\omega}{c} - \frac{1}{r}}{1 - \frac{re^{i\omega(R-r)/c}}{R}}\delta r\right|^2 = \frac{\left[\frac{\omega^2}{c^2} + \frac{1}{r^2}\right]\delta r^2}{1 + \frac{r^2}{R^2} - \frac{r}{R}\underbrace{\left[e^{i\omega(R-r)/c} + e^{-i\omega(R-r)/c}\right]}_{=2\cos(\omega(R-r)/c)}}, \tag{A.8}$$

and

$$\left|\frac{\frac{i\omega}{c} - \frac{1}{R}}{\frac{Re^{i\omega(r-R)/c}}{r} - 1}\delta R\right|^2 = \frac{\left[\frac{\omega^2}{c^2} + \frac{1}{R^2}\right]\delta R^2}{1 + \frac{R^2}{r^2} - \frac{R}{r}\underbrace{\left[e^{i\omega(r-R)/c} + e^{-i\omega(r-R)/c}\right]}_{=2\cos(\omega(r-R)/c)}}. \tag{A.9}$$

For the geometry considered here R = 7m and r = 1m thus $R - r$ = 6m, $r - R$ = −6m, $R/r = 7$ and $r/R = 1/7$. The maxima and minima of the first term are:

$$\frac{(\omega^2/c^2 + 1)\delta r^2}{1 + 1/49 - (1/7)\cdot 2 \cdot \pm 1} = \frac{(\omega^2/c^2 + 1)\delta r^2}{(50 \mp 14)/49}, \tag{A.10}$$

and the second

$$\frac{(\omega^2/c^2 + 1/49)\delta R^2}{1 + 49 - 7\cdot 2\cdot \pm 1} = \frac{(\omega^2/c^2 + 1/49)\delta R^2}{50 \mp 14}. \tag{A.11}$$

The frequency ω is in the range 0 to 600s^{-1} a range for ω^2/c^2 of 0 to 2/5m^2. So the first and second terms are now

$$\frac{(\{0, 2/5\} + 1)\delta r^2}{(50 \mp 14)/49} = \frac{\{1, 1.43\}\delta r^{\,2}}{\{0.7, 1.3\}}, \tag{A.12}$$

and

$$\frac{(\{0, 2/5\} + 1/49)\delta R^2}{50 \mp 14} = \frac{\{0.02, 0.42\}\delta R^{\,2}}{\{36, 64\}}. \tag{A.13}$$

The minimum and maximum perturbations are $0.3 \times 10^{-3}\delta R$ and $11.6 \times 10^{-3}\delta R$ and $0.8\delta r$, $1.9\delta r$. The perturbing term δr depends on the movement of the hydrophone relative to the source. In this case the airgun and hydrophone are fixed to the source rig; δr is then zero. The perturbation δR dependent on the source depth and hydrophone depth. This varies as the water surface goes up and down. If the source sinks by 0.5m and r remains constant then

δR is 1m. The perturbation term then has a maximum size of $\approx$0.01 at 100Hz. The error decreases as frequency decreases.

$$S = \frac{M}{T} \left[1 + \{0.7, 2\}\delta r(= 0) + \{0.3 \times 10^{-3}, 11.6 \times 10^{-3}\}\delta R\right]^{-1}. \tag{A.14}$$

This calculation only includes errors due to moving the ghost and the gun relative to the sensor. This error is the maximum possible error. The error increases with frequency. Consider the cosine term in the denominator of each expression. The error is maximised when the denominator is minimal, which happens when the cosine term equals -1. That occurs at $n_o\pi$ where n_o is any *odd* integer. If $\omega(r - R)/c = n_o\pi$ then $\lambda(r - R) = n_o/2$. Which is when the source and ghost constructively interfere with each other. At other times the error is reduced due to the destructive interference between the source and ghost arrivals.